

Research Paper



Further reverberations of the 1983 impact with Saturn's C ring

Richard G. French ^{a,b}*, Philip D. Nicholson ^c, Matthew M. Hedman ^d, Heikki Salo ^e, Essam A. Marouf ^f, Colleen A. McGhee-French ^b, Nicole Rappaport ^g, Joshua Colwell ^h, Richard Jerousek ^h, Victor M. Afifbo ^d, Sophia Flury ⁱ, Jolene Fong ^b, Ryan Maguire ^j, Glen Steranka ^b, Matthew S. Tiscareno ^k

^a Space Science Institute, Boulder, CO 80301, USA

^b Department of Astronomy, Wellesley College, Wellesley, MA 02481, USA

^c Astronomy Department, Cornell University, Ithaca, NY 14853, USA

^d Department of Physics, University of Idaho, Moscow, ID 83844, USA

^e Astronomy and Space Physics, University of Oulu, FI-90014, Finland

^f Department of Electrical Engineering, San José State University, San José, CA 95192, USA

^g Jet Propulsion Laboratory, Pasadena, CA 91109, USA

^h Department of Physics, University of Central Florida, Orlando, FL 32816, USA

ⁱ Institute for Astronomy, University of Edinburgh, Royal Observatory, Edinburgh, UK

^j Department of Mathematics, MIT, Cambridge, MA 02139, USA

^k SETI Institute, Mountain View, CA 94043, USA

ARTICLE INFO

ABSTRACT

Keywords:

Occultations

Planets

Rings

A pattern of ~ 1 km wavelength ripples exhibiting a periodic beating pattern in Saturn's inner C ring (74,500–77,765 km) was detected in low-inclination *Cassini* Radio Science Subsystem (RSS) occultation observations made in 2010 (Marouf et al., 2011). Initially interpreted as analogous to the ~ 30 km wavelength vertical corrugations with $m = 1$ discovered in the C and D rings in near-equinox Cassini Imaging Science Subsystem (ISS) images by Hedman et al. (2007, 2011), the shorter wavelength of these features suggested that they had evolved from a pair of impacts several centuries ago. However, important inconsistencies with this model prevented a secure identification of their origin. A comprehensive search has revealed additional detections of this pattern in *Cassini* RSS, Visual and Infrared Mapping Spectrometer (VIMS) and Ultraviolet Imaging Spectrograph (UVIS) occultations observed between 2008 and 2017 that show a significant decrease in the wavelength of the ripples over time, suggesting a much more recent origin than centuries ago. We identify the conspicuous beat pattern visible in the ripple structure as the interference of $m = 0$ and $m = 2$ vertical modes of similar amplitudes but slightly different frequencies, evolving over time and winding up at a rate governed by the mean motion of ring particles, rather than by the much slower node rate that is applicable to the $m = 1$ corrugations. From empirical fits to the observed time-dependent wavelengths of the two modes and power spectral analysis of individual optical depth profiles, we demonstrate that the short-wavelength vertical corrugations originated from the same event that produced the longer-wavelength $m = 1$ periodic structure in the rings. We infer an impact date of UTC 1983 Sep 19.25 \pm 5.5 d, taking into account a plausibly small contribution of ring self-gravity to the windup rates of the corrugations. No convincing signatures of counterpart $m = 0$ or $m = 2$ radial modes, or of vertical modes with $m \geq 3$, are present in the occultation data, and no evidence of ripple structure is detectable beyond an orbital radius of 77,765 km. The measured amplitudes A_z^0 and A_z^2 of the newly-identified modes are anti-correlated with the ring optical depth. We detect a significant decrease in the amplitudes of both modes between 2008 and 2017. N-body numerical collisional simulations provide constraints on the vertical and radial ring viscosity that are compatible with the observed radial trend of mode amplitudes A_z^0 and A_z^2 and their variation with time. Assuming an effective particle size $R=1$ m, the inferred coefficient of restitution $e_n \sim 0.5$, with corresponding vertical and radial viscosities $v_z = 1.6 \text{ cm}^2 \text{ s}^{-1}$ and $v_r = 2.2 \text{ cm}^2 \text{ s}^{-1}$ at a radius of 75,500 km. The initial amplitudes of the $m = 0$ and $m = 2$ vertical modes are estimated to be ~ 4 to 7 times their observed values in 2017 in this region.

* Corresponding author at: Department of Astronomy, Wellesley College, Wellesley, MA 02481, USA.

E-mail address: rffrench@wellesley.edu (R.G. French).

1. Introduction

A mysterious pattern of ~ 1 km wavelength ripples exhibiting a periodic beating pattern was detected in Saturn's inner C ring (74,500–77,765 km) from low-inclination *Cassini* Radio Science Subsystem (RSS) occultation observations made in 2010 (Marouf et al., 2011). Reminiscent of the ~ 30 km wavelength vertical corrugations in the rings visible in near-equinox *Cassini* Imaging Science Subsystem (ISS) images that are believed to have resulted from an impact swarm in late 1983 (Hedman et al., 2007, 2011, 2015), the shorter-wavelength ripples were provisionally interpreted as much more tightly wound spirals that had evolved from a pair of impacts several centuries ago, but important inconsistencies with this model prevented a secure identification of their origin Marouf et al. (2011). A comprehensive search of multi-instrument occultation observations over the entire duration of the *Cassini* mission has revealed additional detections of this pattern in RSS, Visual and Infrared Mapping Spectrometer (VIMS) and Ultraviolet Imaging Spectrograph (UVIS) occultations between 2008 and 2017 that show a significant decrease in the wavelength of the ripples over time, suggesting a much more recent origin of the short-wavelength ripple structure.

In this paper, we demonstrate that the ripple structure was generated during the same 1983 impact that was responsible for the $m = 1$ corrugation pattern visible in near-equinox *Cassini* ISS images (Hedman et al., 2007, 2011, 2015). We begin with a survey of the observations in Section 2, and in Section 3 we develop a generalized model for the time evolution of vertical and radial normal modes excited by an idealized ring impact. In Section 4, we measure the windup rate of the waves, constrain the impact date, and identify the normal modes responsible for the beat pattern of the observed ~ 1 km wavelength ripples. In Section 5, we measure the variation of the amplitudes of the ripple patterns across the inner and middle C ring and show that they decreased significantly over the course of the *Cassini* mission. We estimate the possible effects of ring self-gravity on the windup rates of the ripple patterns. Then, in Section 6, we present the results of N-body kinematic collisional simulations of the perturbations for a range of assumed ring particle properties and compare the trends in the measured amplitudes of the waves over time with theoretical models of the time-dependent damping behavior. In Section 7, we discuss considerations for the impact formation mechanism responsible for the observed structure, and in the final section, we summarize our key results.

2. Observations

The ripple structure that is the focus of this study is most clearly evident in low optical depth regions of the inner C ring observed during occultations at low ring opening angles. To set the general scene, Fig. 1 shows the radial normal optical depth profile derived from the *Cassini* RSS_133I_X25 occultation over the ring plane radial range 74,500–78,300 km, from just exterior to the C ring inner edge at 74,490 km to the onset of the higher optical depth region of the middle C ring beyond 78,000 km.¹ In the upper panel, selected low optical depth regions are enclosed by dashed boxes labeled Rxx.x, where xx.x corresponds to the radius of the center of the region in thousands of km. The second and third rows show two such regions in more detail. Region R75.5 at left has a mean normal optical depth $\tau_n \sim 0.05$ and spans 370 km (75,300–75,670 km), exhibiting an overall ~ 30 km undulatory variation in optical depth with a prominent shorter-wavelength beat frequency pattern shown at higher resolution in the lower left panel. For future reference, we overplot the theoretical signature of a putative

$m = 1$ vertical mode of amplitude $A_z^1 = 100$ m and radial wavelength $\lambda_z^1 = 30.6$ km, the predicted value for the windup of an $m = 1$ vertical mode with an impact date $t_i = 1983.7$ (Hedman et al., 2007, 2011, 2015). (This is a notional sinusoidal signature, not the result of a fit. The wave amplitude and phase have been estimated by eye to give a plausible match.) Similarly, at right, we show region R77.7, with a mean normal optical depth $\tau_n \sim 0.04$ spanning 125 km (77,640–77,765 km), including two unresolved features near 77,660 and 77,760 km. A similar beat pattern is evident, and again we overplot a notional sinusoid with amplitude $A_z^1 = 100$ m and $\lambda_z^1 = 35.1$ km, corresponding to the predicted wavelength at this orbital radius for an $m = 1$ vertical mode for the same impact date t_i .

Fig. 2 shows the same RSS_133I_X25 profile for R76.6 (76,500–76,750 km), containing two features of unknown origin — B10 and B11, from the catalog of Baillié et al. (2011) — straddling a radial zone of $\tau_n \sim 0.04$ that contains similar short wavelength structure to that seen in regions R75.5 and R77.7, but with less clearly visible repeating beat frequency wavepackets, or longer wavelength periodic variations in optical depth. Here, we overplot the predicted signature of an $m = 1$ vertical wave with wavelength $\lambda_z^1 = 32.8$ km and amplitude $A_z^1 = 100$ m.

Fig. 3 shows the remaining labeled regions:

- Region R74.6 (74,500–74,700 km) has complex structure, including W74.51 (an outer Lindblad resonance (OLR) spiral density wave associated with an internal f -mode of Saturn with $m = 8$ and $l = 12$ French et al., 2021), and Baillié et al. (2011) feature B1, identified by French et al. (2019) as an outer vertical resonance (OVR) bending wave associated with Saturn f -mode with $m = 7$ and $l = 10$. The background optical depth $\tau_n \sim 0.05$, except for four narrow ~ 15 km-wide gaps centered near 74,550, 74,600, 74,625, and 74,660 km, three of which have unidentified wavelike structure adjacent to their relatively sharp inner edges. There is additional short wavelength ($\lambda \sim 1$ km) quasiperiodic structure reminiscent of that seen in R75.5, R76.6, and R77.7, but it is not readily distinguishable from possible unidentified density or bending waves with comparable wavelengths.
- Region R74.9 (74,700–75,100 km) has variable $\tau_n(\sim 0.05 - 0.12)$ and contains three strong waves (Baillié et al., 2011): B2 (the Mimas 4:1 inner Lindblad resonance (ILR) and OVRs B3 and B4, attributed to Saturn f -modes with $m = 4, l = 5$ and $m = 9, l = 14$, respectively (French et al., 2019)). Apart from these waves, no obvious ~ 1 km wavelength structure is evident in this region.
- Region R75.2 (75,100–75,300 km) has a rather uniform $\tau_n \sim 0.05$, and contains the W75.14 wave — a Saturn-driven OLR f -mode ($m = 10, l = 16$) — and an unidentified localized feature near 75,200 km. The characteristic $\lambda \sim 1$ km wavepacket pattern is evident at low amplitude throughout this region.
- Region R75.4 (75,100–75,670 km) (labeled in Fig. 1) spans regions R75.2 and R75.5. It is the longest interval of roughly uniform low optical depth $\tau_n(\sim 0.05)$ in the inner C ring and shows ~ 1 km wavelength structure throughout.
- Region R76.9 (76,750–77,000 km) has a variable normal optical depth $\tau_n \sim 0.05 - 0.10$, with an asymmetric localized peak near 76,910 km, superimposed throughout by low-amplitude oscillations with $\lambda \sim 1$ km.
- Region 77.3 (77,175–77,350 km) has the highest average optical depth ($\tau_n \sim 0.10$) of any of the labeled inner C ring regions, and little or no evidence of short-wavelength periodic structure.

We will revisit these regions in Section 5, when we estimate the radial variation in the amplitudes of the modes responsible for the short-wavelength C ring ripples, which are visible by eye only when $\langle \tau_n \rangle \lesssim 0.05$. No ripple structure was detected exterior to 77,765 km in any observations.

Table 1 lists the key characteristics of the RSS, UVIS, and VIMS occultations used in this study, including the calendar date of the event,

¹ The RSS_133I_X25 profile was observed during the *Cassini* rev 133 ingress occultation observed at X-band from DSN station DSS-25, with a ring opening angle of $B^* = 1.883^\circ$. The diffraction reconstruction was performed with a shortest resolvable wavelength of 300 m.

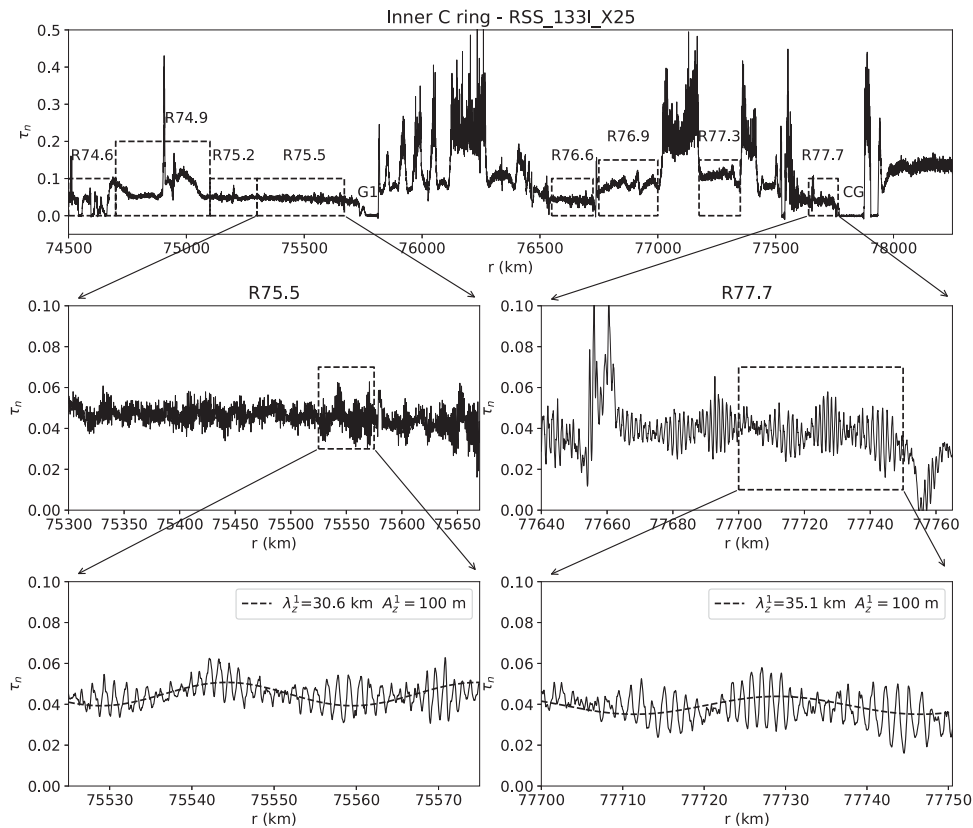


Fig. 1. The radial normal optical depth profile of the inner C ring, from the RSS_133I_X25 occultation of 2010 June 18 observed at low incidence angle ($B^* = 1.883^\circ$, $\tan B_{\text{eff}} = 0.1616$). The RSS data were diffraction-corrected with a processing resolution of 200 m. The upper panel shows the locations of selected ring regions labeled as Rxx.x, where xx.x is the approximate central radius in thousands of km. The second row shows two regions (R75.5 and R77.7) with particularly strong short wavelength ($\lambda \sim 1$ km) ripple structure exhibiting a beating pattern indicative of the presence of two waves of nearly equal wavelength. These two regions are immediately interior to the most prominent gaps in the inner C ring: G1 at 75,750 km and the Colombo gap (labeled CG) at 77,800 km. There are also longer wavelength undulations in the background optical depth that may be associated with the $m = 1$ vertical corrugations detected by [Hedman et al. \(2011, 2015\)](#) in Cassini ISS images obtained at low incidence angle. The third row zooms in to reveal the ripple structure in greater detail. In each lower panel, we include the notional signature of an $m = 1$ vertical corrugation of amplitude $A_z^1 = 100$ m with radial wavelength λ_z^1 corresponding to the local radial wavenumber predicted for an impact with the rings in 1983.7.

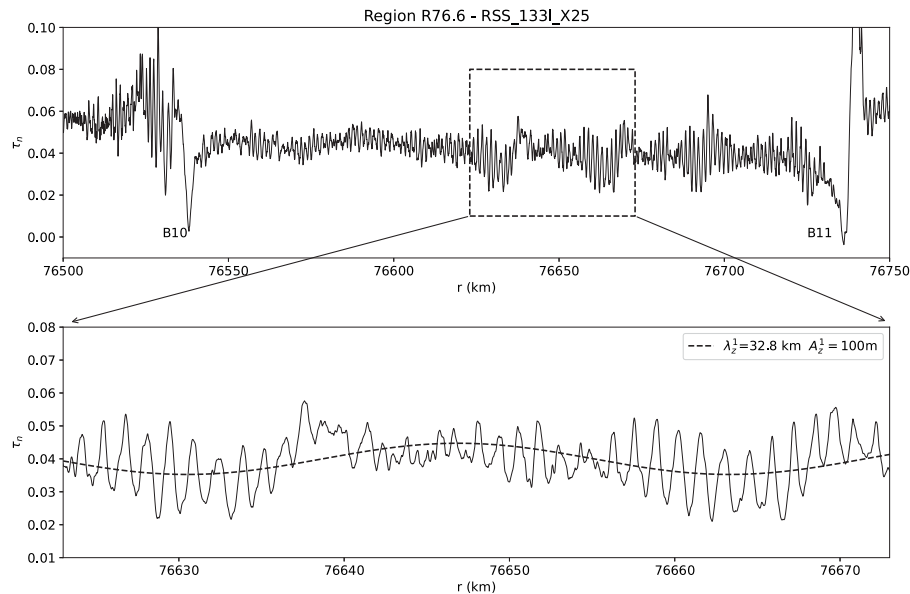


Fig. 2. The RSS_133I_X25 radial optical depth profile for R76.6 (76,500–76,750 km). The features labeled B10 and B11 are wavelike structures of unknown origin ([Baillié et al., 2011](#)). As in [Fig. 1](#), the region of uniform background optical depth $\tau_n \sim 0.04$ contains both short- and long-wavelength structure. The dashed line in the lower panel shows the theoretical signature of an $m = 1$ vertical wave with radial wavelength $\lambda_z^1 = 32.8$ km and vertical amplitude $A_z^1 = 100$ m, with the phase adjusted by eye to provide a plausible match to the data.

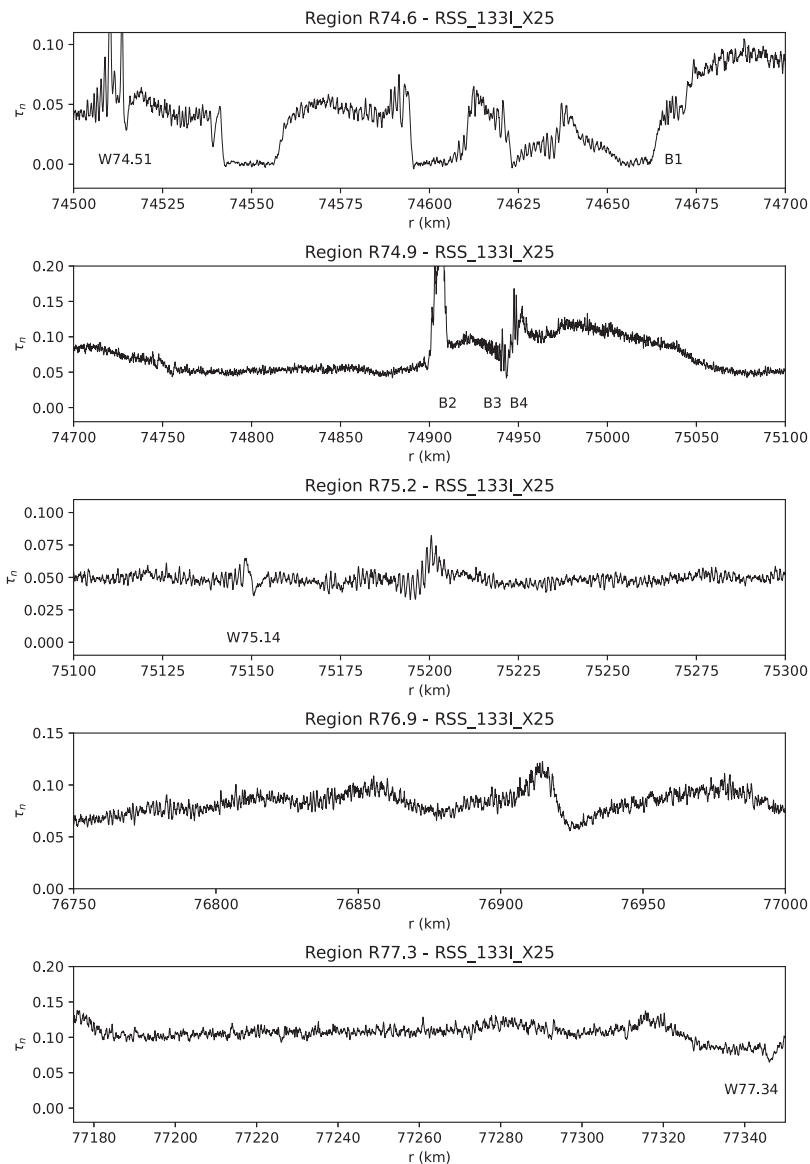


Fig. 3. RSS_133I_X25 radial optical depth profiles for five selected radial ranges in the inner C ring. See text for details.

the ring opening angle B^* (as seen from the DSN station on Earth for RSS events and from the star for stellar occultations), and for regions R75.5 and R77.7 the ring intercept time in decimal years, the inertial longitude in the ring plane θ , $\tan B_{\text{eff}}$, and ϕ , where the effective ring opening angle B_{eff} is defined by

$$\tan B_{\text{eff}} = \frac{\tan B^*}{\cos \phi} \quad (1)$$

and ϕ is the azimuthal angle in the ring plane between the line of sight from the distant end of the occultation ray and the local radial direction (Gresh et al., 1986). As we show in Section 3.6.1 below, the detectability of vertical corrugations in the ring is enhanced when $|\tan B_{\text{eff}}| \ll 1$ and muted when $|\tan B_{\text{eff}}| \gg 1$, which corresponds to a viewing geometry along the wave crests and troughs. Table 1 includes all occultation data sets with well-determined geometry that span the entire inner C ring and have sufficiently high radial resolution and SNR to reveal 1-km periodic structure in a power spectrum of the optical depth profile between 75,000 km and 78,000 km. In all, 35 occultations met these criteria. Except for the very low-inclination UVIS_IotOri_159E event, we excluded multiple-star occultations. The ripple structure was detectable in high-SNR observations with $|\tan B_{\text{eff}}|$ as large as 1.75, in isolated regions. The Cassini orbital tour spanned

a range of inclinations, resulting in an uneven time distribution of ripple detections. The earliest were RSS observations in 2008 and 2010; low-inclination stellar occultations observed at this time were either recorded at too low a cadence to resolve the ripple structure, had unfavorable $|\tan B_{\text{eff}}| > 1$, or did not have sufficient SNR to reveal the ripple structure. Subsequent UVIS occultations in 2012, and UVIS and VIMS occultations in 2017, had favorable geometry and SNR, resulting in ripple detections. In addition, Table 1 includes three very high SNR VIMS occultations of the star α Sco that have very high $|\tan B_{\text{eff}}|$. In Section 4.2.2, we take advantage of the geometry of these events to confirm that the modes responsible for the ripple structure involve vertical rather than radial disturbances. The RSS observations were diffraction-reconstructed with a minimum resolvable wavelength of 0.3 km, using the inversion method of Marouf et al. (1986). All observations were sub-sampled, interpolated, and rebinned to a common radius scale at an oversampled resolution of 0.025 km, registered to the absolute radius scale and ring plane geometry given by French et al. (2017).

Fig. 4 shows a gallery of representative low-inclination RSS, UVIS, and VIMS occultation profiles of region R75.5 (75,300–75,670 km), which is of special interest because it has a uniform background optical depth and exhibits significant ripple structure over a range of several

Table 1
Cassini C ring occultation observations.

Event ID ^a	UTC Date	B^* (°)	R75.5 ^b				R77.7 ^c			
			Year ^d	θ (°)	$\tan B_{\text{eff}}$	ϕ (°)	Year ^d	θ (°)	$\tan B_{\text{eff}}$	ϕ (°)
RSS_056E_X34	2008 JAN 15	-7.032	2008.0393117	318.27	0.4017	107.88	2008.0393144	324.71	0.2995	114.32
RSS_057E_X43	2008 JAN 27	-7.378	2008.0719540	318.41	0.4060	108.60	2008.0719568	324.70	0.3076	114.90
RSS_060E_X26	2008 MAR 02	-8.642	2008.1659378	323.97	0.3410	116.46	2008.1659399	327.94	0.3000	120.44
RSS_060E_X14	2008 MAR 02	-8.642	2008.1659378	323.97	0.3410	116.46	2008.1659399	327.94	0.3000	120.44
RSS_063E_X63	2008 APR 01	-9.598	2008.2497547	322.62	0.3723	117.01	2008.2497569	326.34	0.3309	120.73
RSS_064E_X43	2008 APR 11	-9.783	2008.2759833	324.04	0.3576	118.83	2008.2759853	327.50	0.3228	122.28
RSS_067E_X14	2008 MAY 09	-9.905	2008.3544675	324.52	0.3528	119.66	2008.3544696	327.87	0.3205	123.01
RSS_123L_K34	2009 DEC 25	4.829	2009.9832636	312.51	0.4235	78.49	2009.9832566	312.43	0.4206	78.41
RSS_123L_X34	2009 DEC 25	4.829	2009.9832636	312.51	0.4235	78.49	2009.9832566	312.43	0.4206	78.41
RSS_123L_X43	2009 DEC 25	4.829	2009.9832636	312.51	0.4235	78.49	2009.9832566	312.43	0.4206	78.41
RSS_125L_K34	2010 JAN 26	4.767	2010.0707021	306.94	0.2807	72.72	2010.0706954	306.86	0.2794	72.63
RSS_125L_X34	2010 JAN 26	4.767	2010.0707021	306.94	0.2807	72.72	2010.0706954	306.86	0.2794	72.63
RSS_125L_X43	2010 JAN 26	4.767	2010.0707021	306.94	0.2807	72.72	2010.0706954	306.86	0.2794	72.63
RSS_125E_X63	2010 JAN 26	4.765	2010.0711581	121.22	-0.2132	246.99	2010.0711650	121.31	-0.2140	247.07
RSS_125E_K55	2010 JAN 26	4.765	2010.0711581	121.22	-0.2132	246.99	2010.0711650	121.31	-0.2140	247.07
RSS_125E_X55	2010 JAN 26	4.765	2010.0711581	121.22	-0.2132	246.99	2010.0711650	121.31	-0.2140	247.07
RSS_133L_X15	2010 JUN 18	1.883	2010.4625766	306.82	0.1616	78.26	2010.4625698	306.87	0.1622	78.31
RSS_133L_X25	2010 JUN 18	1.883	2010.4625766	306.82	0.1616	78.26	2010.4625698	306.87	0.1622	78.31
RSS_133E_X15	2010 JUN 19	1.886	2010.4630397	129.98	-0.2203	261.40	2010.4630468	129.93	-0.2192	261.36
RSS_133E_X25	2010 JUN 19	1.886	2010.4630397	129.98	-0.2203	261.40	2010.4630468	129.93	-0.2192	261.36
RSS_133E_K25	2010 JUN 19	1.886	2010.4630397	129.98	-0.2203	261.40	2010.4630468	129.93	-0.2192	261.36
RSS_133E_X34	2010 JUN 19	1.886	2010.4630398	130.00	-0.2209	261.43	2010.4630468	129.95	-0.2197	261.38
RSS_133E_X43	2010 JUN 19	1.886	2010.4630398	130.00	-0.2209	261.43	2010.4630468	129.95	-0.2197	261.38
UVIS_IotOri_159E	2012 JAN 04	-1.192	2012.0085225	253.78	0.0407	120.77	2012.0085292	251.65	0.0434	118.65
UVIS_AlPMa168I	2012 JUN 28	-13.481	2012.4913703	84.28	-0.7067	289.83	2012.4913666	83.62	-0.7067	289.83
UVIS_GamOri234I	2016 APR 03	11.227	2016.2552904	11.49	-1.0104	258.67	2016.2552828	12.56	-1.0104	258.67
VIMS_alpSco241b_1umE ^e	2016 AUG 30	-32.161	2016.6629554	34.00	6.5160	95.54	2016.6629701	30.47	17.8950	92.01
VIMS_alpSco243_1umE ^e	2016 SEP 23	-32.161	2016.7284804	32.06	10.0087	93.60	2016.7284942	28.80	104.4042	90.35
VIMS_alpSco245_1umE ^e	2016 OCT 13	-32.161	2016.7821833	32.28	9.4241	93.83	2016.7821948	28.43	-1471.0714	89.98
VIMS_alpOrI268_1umE	2017 APR 06	11.682	2017.2634126	206.14	0.5316	67.11	2017.2634220	203.44	0.4786	64.41
VIMS_alpOrI269_1umE	2017 APR 14	11.682	2017.2830482	201.36	0.4452	62.32	2017.2830565	199.08	0.4141	60.05
VIMS_alpCMa274_1umE	2017 MAY 13	-13.482	2017.3643961	267.77	0.5010	118.59	2017.3644128	270.08	0.4669	120.90
UVIS_AlPMa274E	2017 MAY 13	-13.482	2017.3643962	291.11	0.3046	141.91	2017.3644129	292.08	0.3007	142.88
VIMS_alpOrI277_1uml	2017 JUN 05	11.682	2017.4250516	346.32	-0.3540	234.26	2017.4250423	346.85	-0.3385	232.35
VIMS_alpCMa281_1uml	2017 JUN 27	-13.482	2017.4877248	106.79	-1.7511	277.87	2017.4876943	105.08	-1.0960	282.64
UVIS_AlPMa281E	2017 JUN 27	-13.482	2017.4879218	359.59	0.2779	210.39	2017.4879523	357.54	0.2724	208.34
VIMS_alpCMa281_1umE	2017 JUN 27	-13.482	2017.4879221	33.60	0.5561	244.46	2017.4879526	28.85	0.4751	239.69

^a Event IDs encode the instrument name, three-digit rev number, and direction (I for ingress, E for egress). VIMS events encode the star ID, the wavelength of the VIMS observation used, and the DSN number. RSS events encode the observing band (K for Ka-band, X for X-band) and the DSN number.

^b Region R75.5 — quantities evaluated at $r = 75,500$ km.

^c Region R77.7 — quantities evaluated at $r = 77,700$ km.

^d Fractional year evaluated at the ring plane intercept time, computed as $\text{yyyy.yyyy} = 2000 + \text{ET}/365.25/86400$, where ET is ephemeris seconds after J2000. To convert to a calendar date, use the ET, rather than the decimal year, to avoid leap year issues.

^e High $|\tan B_{\text{eff}}|$ event.

hundred km. Optical depths for UVIS and VIMS have been doubled to be directly comparable to RSS observations, for which the effective extinction efficiency asymptotically approaches 2 by Babinet's principle (see French and Nicholson, 2000 for a discussion of the validity of this approximation). Five separate high-SNR RSS occultation events spanning the inner C ring were observed at low incidence angle from multiple DSN stations at X and Ka band ($\lambda = 3.6$ and 0.9 cm, respectively) during Rev 123 (ingress), Rev 125 (ingress and egress), and Rev 133 (ingress and egress).² Representative examples of these five events are included at the top of the figure, showing intermittent short wavelength wavepackets. UVIS_IotOri_159E was observed at an exceptionally low $B^* = -1.192^\circ$ and $\tan B_{\text{eff}} = 0.0407$ (Table 1) and is particularly sensitive to short wavelength periodic vertical structure in the ring. Finally, we include nine VIMS occultations with a range of viewing geometries and sensitivities to vertical corrugations.

² Earlier RSS occultations from revs 056–067 are included in our analysis below. We excluded the RSS Rev 079 chord occultation because its minimum radius was 76,460 km, missing R75.5. RSS observations were obtained at low ring opening angle during rev 1371 as well, but were obscured by the planet below a ring plane radius of 78,000 km.

Fig. 5 shows a similar gallery of representative low-inclination RSS, UVIS, and VIMS occultation profiles for region R77.7 (77,640–77,765 km), featuring the strongest ripple structure visible anywhere in the inner C ring. The prominence of the short wavelength ripple structure varies from profile to profile, in part owing to the variation of $\tan B_{\text{eff}}$. The radial locations of the wavepackets differ from profile to profile, possibly indicative of evolution of the structure over time or as the result of differing viewing geometry, as explored in Section 5. This region lies ~ 100 – 200 km interior to the strong Titan 1:0 inner Lindblad resonance at 77857.4 km (Nicholson et al., 2014), resulting in radial distortions of the wavepackets, depending on the relative longitude of Titan (see Section 3.5). Notice that all three VIMS α Sco profiles show a single wavepacket at 77,740 km, near the inner edge of the Colombo gap, even though $|\tan B_{\text{eff}}| \gg 1$ for these observations (see Table 1), suggesting that this may represent radial (rather than vertical) wavelike structure, perhaps driven by the Titan resonance.

3. Theoretical background

In this section, we provide the theoretical background for our interpretation of the short wavelength C ring ripple structure as the result of a recent impact of a debris swarm with Saturn's ring. We expand on previous studies that attributed the $\lambda \sim 30$ km wavelength

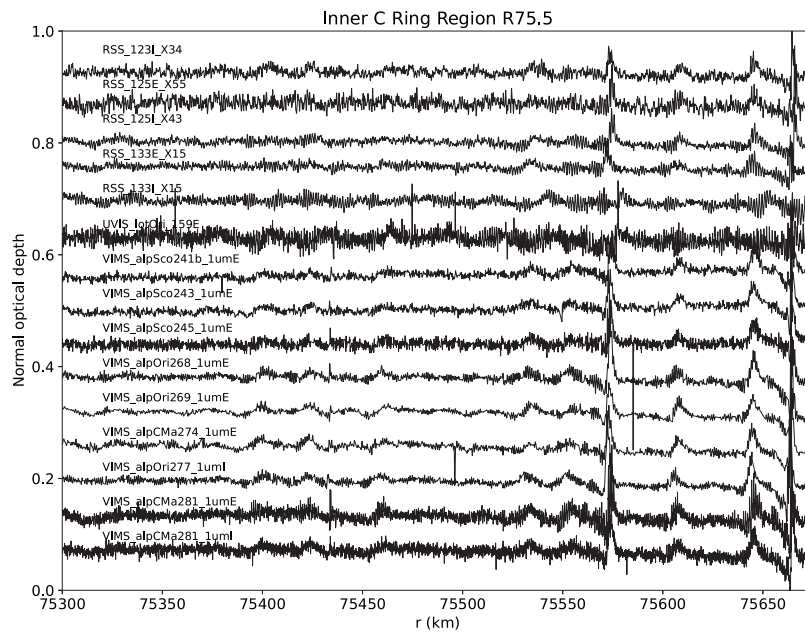


Fig. 4. Gallery of representative low inclination RSS, UVIS, and VIMS occultation profiles of region R75.5 (75,300–75,670 km). The localized features near 75,570 and 75,660 km have no measurable deviations from circular and equatorial orbits. They may be isolated embedded ringlets or short wavelength density waves of unknown origin. The prominence of the short wavelength ripple structure varies from profile to profile, in part owing to the variation of $\tan B_{\text{eff}}$. See text for details.

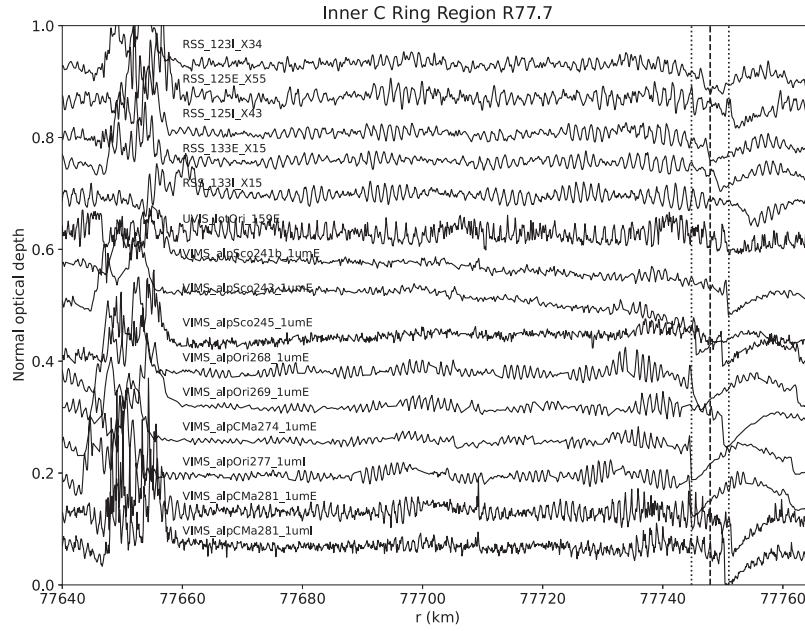


Fig. 5. Gallery of representative low inclination RSS, UVIS, and VIMS occultation profiles of region R77.7 (77,640–77,765 km). The dashed vertical line at 77747.89 km marks the mean location of the inner edge of the Colombo gap, and the dotted vertical lines denote the fitted amplitude $ae = 3.11$ km of the forced eccentricity resulting from the nearby Titan 1:0 inner Lindblad resonance at 77857.4 km (Nicholson et al., 2014) that similarly distorts the local radial structure. See text for additional details.

corrugations seen in images in Saturn's rings to differential apsidal precession and nodal regression of $m = 1$ perturbations since the time of impact (Hedman et al., 2007, 2011, 2015). These studies describe a model in which an initially circular and equatorial ring was instantaneously distorted radially and vertically into non-circular inclined keplerian orbits, with radially-dependent amplitudes in eccentricity and inclination, but aligned pericenters and nodes. Here, we broaden this conceptual framework by representing the disturbance as producing a combination of the wavenumber $m = 1$ keplerian components investigated previously with possible additional radial and vertical distortions represented by normal modes with $m \neq 1$ that might account for the $\lambda \sim 1$ km beating signatures observed in the *Cassini* occultation profiles

seen in Figs. 1–5.

3.1. Normal modes and pattern speeds

We model the ring at semimajor axis a as a keplerian orbit plus a combination of free radial and vertical distortions of azimuthal wavenumber m . For $m \neq 0$, m is the number of radial or vertical minima and maxima in the azimuthal pattern, and the pattern speed Ω_P is its angular rotation rate in inertial space. (For clarity, we will denote pattern speeds of radial modes by Ω_{P_r} and pattern speeds of vertical modes by Ω_{P_z} .) As described in Nicholson et al. (2014), the pattern speed of a radial perturbation is expected to be close to that of

a Lindblad resonance at the ring particle's orbit. For a free (or unforced) mode with $m \neq 0$, we define the radial oscillation frequency as

$$\omega_r^m(a) \equiv m\Omega_{P_r}^m(a) = (m-1)n(a) + \dot{\varpi}_{\text{sec}}(a), \quad (2)$$

where the mean motion n and apsidal precession rate $\dot{\varpi}_{\text{sec}}$ are evaluated at semimajor axis a .³ The azimuthal wavenumber m is positive for inner Lindblad resonances (ILR) and negative for outer Lindblad resonances (OLR). In either case, the pattern speed is positive. For the special case of $m = 1$, the term involving the mean motion n vanishes, and the resulting pattern speed is still positive but much slower than for $m \neq 1$, since $\dot{\varpi}_{\text{sec}} \ll n$. For an $m = 1$ equatorial keplerian orbit with eccentricity e about an oblate planet, the apsidal precession rate includes the combined effects of the zonal gravity harmonics J_2, J_4, J_6, \dots and the secular precession induced by the planet's satellites, and is given to $O(J_6)$ by

$$\begin{aligned} \dot{\varpi}_{\text{sec}} = & \sqrt{\frac{GM}{a^3}} \left\{ \frac{3}{2}J_2 \left(\frac{R_p}{a} \right)^2 (1+2e^2) - \frac{15}{4}J_4 \left(\frac{R_p}{a} \right)^4 \right. \\ & \left. + \left[\frac{27}{64}J_2^3 - \frac{45}{32}J_2J_4 + \frac{105}{16}J_6 \right] \left(\frac{R_p}{a} \right)^6 + \frac{1}{4} \sum_{j=1}^{M_o} \frac{m_j}{M} \alpha_{oj}^2 b_{3/2}^1(\alpha_{oj}) \right\}, \end{aligned} \quad (3)$$

from Jacobson (2014). To lowest order, we have

$$\begin{aligned} \dot{\varpi}_{\text{sec}} \approx & \frac{3J_2}{2} \left(\frac{R_p}{a} \right)^2 n \\ \approx & \frac{3J_2}{2} \left(\frac{R_p}{a} \right)^2 \sqrt{\frac{GM}{a^3}} \\ \propto & a^{-7/2}. \end{aligned} \quad (4)$$

Here, G is the gravitational constant, M is the mass of the planet, and R_p is the planet's equatorial radius (Borderies-Rappaport and Longaretti, 1994). The summation is carried out over outer satellites (subscript o) of mass m_j and orbital radius a_{oj} , where $\alpha_{oj} = a/a_{oj}$ and $b_{3/2}^1(\alpha_{oj})$ are Laplace coefficients as defined by Brouwer and Clemence (1961).

For vertical modes with $m \neq 0$, we define the vertical oscillation frequency as

$$\omega_z^m(a) \equiv m\Omega_{P_z}^m(a) = (m-1)n(a) + \dot{\Omega}_{\text{sec}}(a). \quad (5)$$

Here, $\dot{\Omega}_{\text{sec}}$ is the nodal regression rate, which to leading order is the negative of the apsidal precession rate.⁴ Note that $\Omega_{P_z}^m$ is also positive for all $m \neq 0$, except for $m = 1$, where $\Omega_{P_z} = \dot{\Omega}_{\text{sec}} < 0$.

To $O(J_6)$,

$$\begin{aligned} \dot{\Omega}_{\text{sec}} = & -\sqrt{\frac{GM}{a^3}} \left\{ \frac{3}{2}J_2 \left(\frac{R_p}{a} \right)^2 (1+2e^2) - \left[\frac{9}{4}J_2^2 + \frac{15}{4}J_4 \right] \left(\frac{R_p}{a} \right)^4 \right. \\ & \left. + \left[\frac{351}{64}J_2^3 + \frac{315}{32}J_2J_4 + \frac{105}{16}J_6 \right] \left(\frac{R_p}{a} \right)^6 + \frac{1}{4} \sum_{j=1}^{M_o} \frac{m_j}{M} \alpha_{oj}^2 b_{3/2}^1(\alpha_{oj}) \right\}, \end{aligned} \quad (6)$$

from Jacobson (2014).

To lowest order,

$$\begin{aligned} \dot{\Omega}_{\text{sec}}(a) \approx & -\frac{3J_2}{2} \left(\frac{R_p}{a} \right)^2 n \\ \approx & -\frac{3J_2}{2} \left(\frac{R_p}{a} \right)^2 \sqrt{\frac{GM}{a^3}} \\ \propto & -a^{-7/2}, \end{aligned} \quad (7)$$

³ This corresponds to the usual definition of a Lindblad resonance, where $m(n - \Omega_{P_r}^m) = \kappa(a) = n(a) - \dot{\varpi}_{\text{sec}}(a)$, from Shu (1984) Eq. (11).

⁴ For a vertical resonance, $m(n - \Omega_{P_z}^m) = \mu(a) = n(a) - \dot{\Omega}_{\text{sec}}(a)$, from Shu (1984) Eq. (12).

Table 2
Saturn gravity parameters.

Parameter	Value	Note
GM_s	37 931 206.0 km ³ s ⁻²	R. Jacobson (pers. comm.)
R_p	60 330 km	Reference radius for J_n
J_2	$16\ 290.573 \times 10^{-6}$	Iess et al. (2019)
J_4	-935.314×10^{-6}	Iess et al. (2019)
J_6	86.340×10^{-6}	Iess et al. (2019)
J_8	-14.624×10^{-6}	Iess et al. (2019)
J_{10}	4.672×10^{-6}	Iess et al. (2019)
J_{12}	-0.997×10^{-6}	Iess et al. (2019)
$\dot{\omega}_{\text{sat}}$ (75 000 km)	0.000166° d ⁻¹	Satellite contribution to apse rate

Once again, the pattern speed is much slower for $m = 1$ than for $m \neq 1$, since $|\dot{\Omega}_{\text{sec}}| \ll n$, but in this case it is negative.

Eqs. (3) and (6) are accurate to $O(J_6)$; in practice, we extend these results to order J_{12} using the expressions given by Nicholson and Porco (1988). The Saturn gravity parameters used for this study, as measured by *Cassini*, are given in Table 2.

For the special case of $m = 0$, there is no azimuthal dependence of the perturbations. Instead, all ring particles with a given semimajor axis oscillate either radially or vertically in concert. In the radial case, all such particles reach periape at the same time and the ring appears to "breathe" radially at the epicyclic frequency $\kappa(a)$:

$$\begin{aligned} \omega_r^0(a) &= \kappa(a) \\ &= n(a) - \dot{\varpi}_{\text{sec}}(a). \end{aligned} \quad (8)$$

For a vertical $m = 0$ mode, all ring particles with a given semimajor axis have the same vertical displacement at the same time, independent of azimuth, oscillating at the vertical epicyclic frequency $\mu(a)$:

$$\begin{aligned} \omega_z^0(a) &= \mu(a) \\ &= n(a) - \dot{\Omega}_{\text{sec}}(a). \end{aligned} \quad (9)$$

(We use μ for the vertical epicyclic frequency to avoid possible confusion with the ring viscosity v .)

To leading order, the ratio of the vertical and radial $m = 0$ oscillation frequencies is given by

$$\begin{aligned} \frac{\omega_z^0}{\omega_r^0} &\approx 1 + 3J_2 \left(\frac{R_p}{a} \right)^2 \\ &\equiv \frac{\mu(a)}{\kappa(a)}. \end{aligned} \quad (10)$$

Similarly, the vertical and radial pattern speeds $\Omega_{P_z}(m)$ and $\Omega_{P_r}(m)$ differ slightly, via Eqs. (2) and (5), for any given $m \neq 0$. We will exploit these differences in Section 4 to identify the possible vertical and radial normal modes involved in the C ring ripples.

3.2. Vertical corrugations and radial spiral structure

Hedman et al. (2015) showed that periodic structure in the C and D rings could be accounted for by an initial disturbance that simultaneously tilted the ring plane and perturbed ring particles into aligned eccentric orbits. Over time, these $m = 1$ distortions in the ring evolved into an ever-tightening pattern of vertical corrugations and a tightening spiral in the radial direction as a result of differential nodal regression and apsidal precession, respectively. Here, we generalize on this notion by imagining that the initial disturbance resulted in additional perturbations that can be represented as normal modes.

We assume radial and vertical perturbations of the form of normal modes of azimuthal wavenumber m at the local free pattern speeds:

$$r^m(a, t) = a - A_r^m \cos(m\psi_r^m) \quad (11)$$

and

$$z^m(a, t) = A_z^m \sin(m\psi_z^m), \quad (12)$$

where

$$\psi_r^m = \theta - \Omega_{Pr}^m(a)\Delta t - \delta_r^m \quad (13)$$

$$\psi_z^m = \theta - \Omega_{Pz}^m(a)\Delta t - \delta_z^m, \quad (14)$$

and

$$\Delta t = t - t_i. \quad (15)$$

We further assume that all streamlines begin at the impact time t_i with the same values of pericenter longitude δ_r^m and ascending node δ_z^m , independent of a .

For $m = 0$, there is no θ -dependence, and $m\Omega_{Pr}^m$ and $m\Omega_{Pz}^m$ are replaced by ω_r^0 and ω_z^0 :

$$r^0(a, t) = a - A_r^0 \cos[\omega_r^0 \Delta t + \delta_r^0] \quad (16)$$

and

$$z^0(a, t) = A_z^0 \sin[\omega_z^0 \Delta t + \delta_z^0], \quad (17)$$

where δ_r^0 and δ_z^0 are the phases of the radial and vertical modes, respectively, at the impact epoch. The local values of Ω_P and ω can be approximated for $m \neq 0$ by

$$\Omega_{Pr}^m(a) \simeq \Omega_{Pr}^m(r_0) + (\partial \Omega_{Pr}^m / \partial a)(a - r_0) \quad (18)$$

and

$$\Omega_{Pz}^m(a) \simeq \Omega_{Pz}^m(r_0) + (\partial \Omega_{Pz}^m / \partial a)(a - r_0), \quad (19)$$

while for $m = 0$ we have

$$\omega_r^0(a) \simeq \omega_r^0(r_0) + (\partial \omega_r^0 / \partial a)(a - r_0) \quad (20)$$

and

$$\omega_z^0(a) \simeq \omega_z^0(r_0) + (\partial \omega_z^0 / \partial a)(a - r_0). \quad (21)$$

By substitution, we have

$$\psi_r^m \simeq \theta - \Omega_{Pr}^m(r_0)\Delta t - (\partial \Omega_{Pr}^m / \partial a)(a - r_0)\Delta t - \delta_r^m \quad (22)$$

and

$$\psi_z^m \simeq \theta - \Omega_{Pz}^m(r_0)\Delta t - (\partial \Omega_{Pz}^m / \partial a)(a - r_0)\Delta t - \delta_z^m. \quad (23)$$

The third terms on the right hand sides of Eqs. (22) and (23) lead to oscillations in radius at a given time t and longitude θ with wavenumbers k_r^m and k_z^m , which may be written for $m > 1$ as

$$r^m(a, t, \theta) \simeq a - A_r^m \cos[m(\theta - \Omega_{Pr}^m(r_0)\Delta t - \delta_r^m) + k_r^m(a - r_0)] \quad (24)$$

and

$$z^m(a, t, \theta) \simeq A_z^m \sin[m(\theta - \Omega_{Pz}^m(r_0)\Delta t - \delta_z^m) + k_z^m(a - r_0)], \quad (25)$$

where after (Hedman et al., 2011, 2015) we define

$$k_r^m = \left| m \frac{\partial \Omega_{Pr}^m}{\partial a} \right| \Delta t \quad (26)$$

and

$$k_z^m = \left| m \frac{\partial \Omega_{Pz}^m}{\partial a} \right| \Delta t. \quad (27)$$

Note that for $m \neq 1$, $\partial \Omega_{Pr}^m / \partial a$ and $\partial \Omega_{Pz}^m / \partial a$ are both negative and scale approximately as $a^{-5/2}$ (Hedman et al., 2011, 2015). The corresponding radial slope of the vertical corrugations for $m > 1$ is

$$\frac{\partial z^m}{\partial a} \simeq A_z^m k_z^m \cos[m(\theta - \Omega_{Pz}^m(r_0)\Delta t - \delta_z^m) + k_z^m(a - r_0)]. \quad (28)$$

For $m = 1$, we have

$$r^1(a, t, \theta) \simeq a - A_r^1 \cos[\theta - \varpi(r_0, t) + k_r^1(a - r_0)] \quad (29)$$

and

$$z^1(a, t, \theta) \simeq A_z^1 \sin[\theta - \varpi(r_0, t) + k_z^1(a - r_0)], \quad (30)$$

where

$$k_r^1 = \left| \frac{\partial \varpi}{\partial a} \right| \Delta t \quad (31)$$

and

$$k_z^1 = \left| \frac{\partial \varpi}{\partial a} \right| \Delta t. \quad (32)$$

Note that $\partial \varpi / \partial a$ is negative, whereas $\partial \varpi / \partial a$ is positive, resulting in the minus sign for the k_z^1 term in Eq. (30). Both k_r^1 and k_z^1 scale approximately as $a^{-9/2}$. In agreement with Hedman et al. (2015), the corresponding radial slope of the vertical corrugations associated with the $m = 1$ mode is

$$\frac{\partial z^1}{\partial a} \simeq -A_z^1 k_z^1 \cos[\theta - \varpi(r_0, t) - k_z^1(a - r_0)]. \quad (33)$$

For $m = 0$, we have

$$r^0(a, t) \simeq a - A_r^0 \cos[\omega_r^0(r_0)\Delta t - k_r^0(a - r_0) + \delta_r^0] \quad (34)$$

and

$$z^0(a, t) \simeq A_z^0 \sin[\omega_z^0(r_0)\Delta t - k_z^0(a - r_0) + \delta_z^0], \quad (35)$$

independent of longitude θ , where

$$k_r^0 = \left| \frac{\partial \omega_r^0}{\partial a} \right| \Delta t \quad (36)$$

and

$$k_z^0 = \left| \frac{\partial \omega_z^0}{\partial a} \right| \Delta t. \quad (37)$$

Note that both $\partial \omega_r^0 / \partial a$ and $\partial \omega_z^0 / \partial a$ scale approximately as $a^{-5/2}$ and are negative.

The radial slope of the vertical corrugations associated with the $m = 0$ mode is

$$\frac{\partial z^0}{\partial a} \simeq -A_z^0 k_z^0 \cos[\omega_z^0(r_0)\Delta t - k_z^0(a - r_0) + \delta_z^0] \quad (38)$$

We will explore below how the observed radial optical depth profile of the perturbed ring is affected by the varying path length along the line of sight through the corrugated surface.

As the radial disturbance evolves into a spiral pattern, the corresponding radial optical depth profile observed during an occultation will be related to variations in the local surface mass density σ^m associated with each mode, which is inversely proportional to the radial separation of adjacent particle streamlines:

$$\sigma^m = \left| \frac{\sigma_0}{\partial r^m / \partial a} \right|, \quad (39)$$

where σ_0 is the unperturbed surface mass density.

For $m > 1$,

$$\frac{\sigma^m}{\sigma_0} = \frac{1}{1 + A_r^m k_r^m \sin[m(\theta - \Omega_{Pr}^m(r_0)\Delta t - \delta_r^m) + k_r^m(a - r_0)]}, \quad (40)$$

which is valid for $A_r^m k_r^m < 1$, and approximately

$$\frac{\sigma^m}{\sigma_0} \simeq 1 - A_r^m k_r^m \sin[m(\theta - \Omega_{Pr}^m(r_0)\Delta t - \delta_r^m) + k_r^m(a - r_0)] \quad (41)$$

in the limit $A_r^m k_r^m \ll 1$.

For $m = 1$,

$$\frac{\sigma^1}{\sigma_0} = \frac{1}{1 + A_r^1 k_r^1 \sin[\theta - \varpi(r_0, t) + k_r^1(a - r_0)]}, \quad (42)$$

which is valid for $A_r^1 k_r^1 < 1$, and approximately

$$\frac{\sigma^1}{\sigma_0} \simeq 1 - A_r^1 k_r^1 \sin[\theta - \varpi(r_0, t) + k_r^1(a - r_0)] \quad (43)$$

in the limit $A_r^1 k_r^1 \ll 1$.

For $m = 0$,

$$\begin{aligned} \frac{\sigma^0}{\sigma_0} &= \frac{1}{1 - A_r^0 k_r^0 \sin[\omega_r^0(r_0) \Delta t - k_r^0(a - r_0) + \delta_r^0]} \\ &\simeq 1 + A_r^0 k_r^0 \sin[\omega_r^0(r_0) \Delta t - k_r^0(a - r_0) + \delta_r^0]. \end{aligned} \quad (44)$$

The first expression is valid for $A_r^0 k_r^0 < 1$ and the final approximation is valid in the limit $A_r^0 k_r^0 \ll 1$.

3.3. Patterns of radial wavenumbers k_r^m and k_z^m

In Section 4.2, we will use the observed radial and time dependence of the best-fitting wavelengths (and their ratios) of the two components of the ripple structure to identify the azimuthal wavenumbers of candidate modes that match the observations, and to estimate the corresponding impact time t_i . Although in general the radial wavenumbers k_r^m and k_z^m vary linearly in time since impact Δt (ignoring the self-gravity of the ring), their ratios are time-independent, and thus contain no assumptions about the time history of the observed ripple structure. In Appendix B, we derive approximate wavenumber formulae for k_r^m and k_z^m , evaluate them numerically, and show that there are near-degeneracies that prevent the unique identification of the modes that contribute to the ripples observed in a single observation. We show that $k_r^m = k_z^{2-m}$ and $k_z^m \simeq k_r^{2-m}$, and that their ratios have a similar degeneracy:

$$\frac{k_z^{2-m}(a)}{k_z^{2-m}(a)} \simeq \frac{k_z^m(a)}{k_r^m(a)}. \quad (45)$$

To resolve the ambiguity of the modes that are actually present in the data, we will compare observations at different times with different viewing geometry.

3.4. Influence of ring self-gravity on k_r^m and k_z^m

So far, we have assumed that the ring precession rate is due entirely to Saturn's gravity and to the much weaker contributions of external satellites, but as noted by Hedman et al. (2011), a ring with finite surface mass density σ that might also vary with radius changes the nodal regression rate by a small amount that can be estimated using the dispersion relation for free vertical waves. Hedman et al. (2011) showed (see Eqs. (S16)–(S23) in Supporting Online Material) that, for $m = 1$:

$$k_z^1(a) = k_{z0}^1(a) \left[1 + \frac{\pi G}{2\mu} \left(\frac{3\sigma}{a} - \frac{\partial\sigma}{\partial a} \right) \Delta t \right], \quad (46)$$

where $k_{z0}^1(a)$ is the unperturbed vertical wavenumber for $m = 1$ given by Eqs. (6), (9) and (32) above and $\mu = n - \dot{\Omega}_{\text{sec}}$ is the vertical epicyclic frequency. From the symmetry of the dispersion relations for vertical and radial modes, the corresponding result for an $m = 1$ radial mode is

$$k_r^1(a) = k_{r0}^1(a) \left[1 - \frac{\pi G}{2\kappa} \left(\frac{3\sigma}{a} - \frac{\partial\sigma}{\partial a} \right) \Delta t \right], \quad (47)$$

where $k_{r0}^1(a)$ is the unperturbed radial wavenumber for $m = 1$ given by Eqs. (3), (8) and (31) above and $\kappa = n - \dot{\varpi}_{\text{sec}}$ is the radial epicyclic frequency. (Note that, since $k_{z0}^1(a)$ and $k_{r0}^1(a)$ are already proportional to Δt via Eqs. (31) and (32), the corresponding wavenumbers corrected for self-gravity are quadratic functions of Δt .)

Following Hedman et al. (2011), we use the density wave and bending wave dispersion relations to estimate corrections to Ω_{Pr} and Ω_{Pz} , and thence to k_r^m and k_z^m for ring self-gravity. As shown in Appendix A, for $m \neq 0$ or 1, we find that

$$k_r^m = k_{r0}^m \left[1 + \frac{\pi G}{2\kappa} \left(\frac{\sigma_0}{a} - \frac{\partial\sigma_0}{\partial a} \right) \Delta t \right] \quad (48)$$

and

$$k_z^m = k_{z0}^m \left[1 - \frac{\pi G}{2\mu} \left(\frac{\sigma_0}{a} - \frac{\partial\sigma_0}{\partial a} \right) \Delta t \right]. \quad (49)$$

For $m = 0$, we have

$$k_r^0 = k_{r0}^0 \left[1 - \frac{\pi G}{2\kappa} \left(\frac{\sigma_0}{a} - \frac{\partial\sigma_0}{\partial a} \right) \Delta t \right] \quad (50)$$

and

$$k_z^0 = k_{z0}^0 \left[1 + \frac{\pi G}{2\mu} \left(\frac{\sigma_0}{a} - \frac{\partial\sigma_0}{\partial a} \right) \Delta t \right] \quad (51)$$

In practice, we can slightly simplify the above expressions by setting $\kappa \simeq \mu \simeq n$ (from Eqs. (8) and (9)), without significant loss of accuracy. We will make use of these results to estimate the possible effects of a finite ring surface mass density on the windup rates of the ripple structure.

3.5. Influence of the titan 1:0 apsidal resonance on the radial wavenumber k_r

Titan has a strong 1:0 apsidal resonance located in the C ring at $a_{\text{res}} = 77857.4$ km that produces measurable forced eccentricities in ring orbits over the range $r = 74,500$ –79,400 km (see Fig. 19 Nicholson et al., 2014). The measured amplitudes $ae_{\text{Titan}}(a)$ closely match the predicted test particle response to the theoretical resonance strength S determined from the mass and orbital elements of Titan:

$$ae_{\text{Titan}}(a) = \frac{S}{|a - a_{\text{res}}|}, \quad (52)$$

where $S \simeq 382$ km² (Nicholson et al., 2014). For orbits interior to the resonance radius, the perapse is approximately aligned with Titan, and in this case the radial location of a circular ring at longitude θ with semimajor axis a perturbed by the Titan resonance is given by

$$r_{\text{Titan}}(a) = a - \frac{S}{|a - a_{\text{res}}|} \cos(\theta - \theta_{\text{Titan}}), \quad (53)$$

where θ_{Titan} is the mean longitude of Titan at the ring intercept point and observation time. A radial or vertical wave with unperturbed radial wavelength λ will have a perturbed wavelength given by

$$\frac{\lambda_{\text{Titan}}(a)}{\lambda} = \left| \frac{\partial r_{\text{Titan}}}{\partial a} \right| = 1 + \frac{S}{(a - a_{\text{res}})^2} \cos(\theta - \theta_{\text{Titan}}), \quad (54)$$

with corresponding perturbed wavenumber

$$\frac{k_{\text{Titan}}(a)}{k} \simeq 1 - \frac{S}{(a - a_{\text{res}})^2} \cos(\theta - \theta_{\text{Titan}}) \quad (55)$$

and perturbed optical depth

$$\frac{\tau_{\text{Titan}}(a)}{\tau} \simeq 1 - \frac{S}{(a - a_{\text{res}})^2} \cos(\theta - \theta_{\text{Titan}}). \quad (56)$$

Numerically, the fractional change in k is quite small in the inner C ring ($\sim 5 \times 10^{-5}$ at $a = 75,000$ km), but much larger ($\sim 4\%$) in the vicinity of the observed ripple structure near $a = 77,760$ km, only about 100 km interior to a_{res} . We will make use of these results in the interpretation of distortions in the wavepackets evident in the outer R77.7 region.

3.6. Radial optical depth profiles from vertical corrugations and radial spiral structure

The observed signal strength during a ring occultation is modulated by the abundance of ring material encountered along the ray path. Under the assumption that the ring behaves like a classical many-particles-thick layer, the observed normalized intensity I is just

$$\begin{aligned} I &= e^{-\tau_n / |\sin B^*|} \\ &= e^{-\tau}, \end{aligned} \quad (57)$$

where τ_n is the normal optical depth, and τ is the “observed” optical depth. Our goal is to predict the radial optical depth profile $\tau_n(r)$ for an occultation of a ring perturbed by vertical corrugations and radial spiral structure of specified azimuthal wavenumber m .

3.6.1. Vertical corrugations

Under the assumption that ring particles in a thin layer are uniformly distributed along the ray path, the observed optical depth is proportional to the path length of the ray through the ring layer, which depends on the viewing geometry, the effective slope of the ring, and the assumed thickness of the layer. Assuming that the thickness of the ring is constant perpendicular to the local radial slope dz/dr and that an occultation ray penetrates the ring plane only once, Hedman et al. (2015) showed that the optical depth profile $\tau_z(r)$ of a warped ring is given by

$$\tau_z(r) = \frac{\tau_n}{|\sin B^*|} \left[\frac{\sqrt{1 + (dz/dr)^2}}{1 - \cot B^* \cos \phi(dz/dr)} \right], \quad (58)$$

where the slope of the corrugation is assumed to be sufficiently small that the denominator in brackets is always positive. We rewrite the apparent optical depth as

$$\tau_z(r) = \tau_0 \left[\frac{\sqrt{1 + (dz/dr)^2}}{1 - (dz/dr)/\tan B_{\text{eff}}} \right], \quad (59)$$

where $\tau_0 = \tau_n/|\sin B^*|$ is the quiescent optical depth of the undisturbed ring.

Gresh et al. (1986) obtained a slightly different result under the assumption that the vertical thickness of the ring is unchanged by the perturbation:

$$\tau_z(r) = \frac{\tau_0}{1 - (dz/dr)/\tan B_{\text{eff}}}. \quad (60)$$

Since for the present application $dz/dr < 0.05$, the numerator in Eq. (59) differs from unity by at most 0.00125 and can be safely neglected, and the two approaches are effectively identical. In cases where $|(dz/dr)/\tan B_{\text{eff}}| \ll 1$, we have the approximate result

$$\tau_z(r) \simeq \tau_0 [1 + (dz/dr)/\tan B_{\text{eff}}], \quad (61)$$

although this approximation can be violated for ring occultations where $\tan B_{\text{eff}}$ is very small ($\lesssim 0.1$).

For a sinusoidal vertical perturbation, substituting for dz/dr from Eq. (25) for $m \geq 1$, we have

$$\tau_z^m(r) = \frac{\tau_0}{1 - A_z^m k_z^m \sin[m(\theta - \Omega_{P_z}(m, r_0)\Delta t - \delta_z^m) + k_z^m(r - r_0)]/\tan B_{\text{eff}}}, \quad (62)$$

and for $m = 0$ from Eq. (38):

$$\tau_z^0(r) = \frac{\tau_0}{1 - A_0 k_0 \cos[\omega_z^0(r_0)\Delta t - k_z^0(a - r_0) + \delta_z^0]/\tan B_{\text{eff}}}. \quad (63)$$

Notice that the detectability of a vertical corrugation depends strongly on the viewing geometry. If the occultation rays are parallel to the corrugations ($|\phi| \simeq 90^\circ$), then by Eq. (1) $|\tan B_{\text{eff}}| \rightarrow \infty$, and the vertical structure does not affect the observed optical depth, at least under the geometric assumptions of the distribution of ring material.

In the general case that the oblique occultation ray penetrates the corrugated surface at a height z above the ring plane, the apparent radius r_{ap} probed by an occultation ray is offset from the true radius by the projected distance $z/\tan B_{\text{eff}}$:

$$r_{ap} = r - z/\tan B_{\text{eff}}. \quad (64)$$

3.6.2. Radial spiral structure

Under the assumption that τ_n is proportional to the ring’s unperturbed surface density σ_0 , the perturbed optical depth profile associated with radial spiral structure is given by $\tau_r(r) = (\sigma/\sigma_0)\tau_0$. From Eq. (42)

we have for $m \geq 1$:

$$\tau_r^m(r) = \frac{\tau_0}{1 + A_{mr} k_{mr} \sin[m(\theta - \delta_{mr}) - k_{mr}(r - r_0)]} \quad (65)$$

and from Eq. (44) for $m = 0$:

$$\tau_r^0(r) = \frac{\tau_0}{1 + A_r^0 k_r^0 \sin[\omega_r^0(r_0)\Delta t - k_r^0(a - r_0) + \delta_r^0]}. \quad (66)$$

Unlike the case for vertical corrugations, the visibility of radial spiral structure for a given ring opening angle is independent of the azimuthal viewing geometry. Note that $\tau_r^0(r)$ and $\tau_z^0(r)$ are functionally identical, and therefore indistinguishable, if $A_r^0 k_r^0 = A_z^0 k_z^0 / \tan B_{\text{eff}}$, $k_r^0 = k_z^0$, and $\delta_z^0 = \delta_r^0 + 90^\circ$.

3.6.3. Model optical depth profiles with simultaneous vertical and/or radial modes

When multiple vertical or radial modes are present, our prescription for computing the model optical depth profile in this composite case is as follows:

1. Specify the characteristics of any radial normal modes, optionally accounting for the gravitational effect on $k_r(r)$ of a finite surface mass density using Eqs. (48) and (50), and solve for (σ/σ_0) , optionally accounting for the distortion of the radius scale and radial wavenumber by the Titan 1:0 apsidal resonance.
2. Specify the characteristics of any vertical normal modes, optionally accounting for the gravitational effect on $k_z(r)$ of a finite surface mass density using Eqs. (49) and (51) and the effects of the Titan 1:0 resonance, and compute the nominal slope $dz(r)/dr$.
3. Multiply the nominal slope by σ/σ_0 to account for the radial distortion $\partial r/\partial a$ due to any radial modes.⁵
4. Use the modified slope to compute $\tau_z(r)$.
5. Compute the composite optical depth profile τ_c resulting from the ensemble of vertical and radial modes:

$$\tau_c(r) = (\sigma/\sigma_0)\tau_z(r). \quad (67)$$

6. If vertical modes are present, apply the mapping between the true radius and the apparent radius scale from $z(r)$ and $\tan B_{\text{eff}}$.
7. Evaluate $\tau_c(r)$ at the apparent radius values of the observations to enable a direct comparison of the model and the data.

It is sometimes useful to compare the relative contributions of radial and vertical modes to observed perturbations in the background optical depth. Combining Eqs. (63) and (66), and defining $\Delta\tau_r(r) = \tau_r(r) - \tau_0$ and $\Delta\tau_z(r) = \tau_z(r) - \tau_0$, we have for $m = 0$:

$$\frac{\Delta\tau_z(r)}{\Delta\tau_r(r)} \simeq \frac{A_{0z} k_{0z} / |\tan B_{\text{eff}}|}{A_{0r} k_{0r}}. \quad (68)$$

For vertical and radial waves of comparable amplitudes (i.e., $A_{0z} k_{0z} \simeq A_{0r} k_{0r}$), $\Delta\tau_z(r)/\Delta\tau_r(r) \simeq 1/|\tan B_{\text{eff}}|$. Interpreted geometrically, the vertical structure dominates the observed optical depth profile (i.e., $\Delta\tau_z(r)/\Delta\tau_r(r) > 1$) for low-incidence occultations viewed perpendicular to the vertical corrugations when $|\tan B_{\text{eff}}| < 1$, and radial structure dominates (even for low-incidence occultations) when $|\tan B_{\text{eff}}| > 1$.

To illustrate the properties of composite models that include combined radial and/or vertical normal modes, we next compare analytical models of the predicted radial optical depth profiles with the results of ray tracing simulations in which the ring is represented as a multi-layered thin slab of material distorted vertically and radially by a variety of normal modes. Table 3 lists the parameters of the six

⁵ This is a purely kinematical effect, and assumes there is no dynamic coupling between radial and vertical modes. Imagine a sinusoidal vertical corrugation. Now perturb the radial locations of the points on the vertical sine wave with a radial compression/rarefaction. The local slope of the vertical corrugation will be modified by the changed radial distance between streamlines.

Table 3
Composite models of multiple normal modes.

Parameter	Model					
	1	2	3	4	5	6
τ_n	0.045	0.045	0.045	0.045	0.045	0.045
ϕ (°)	78.26	78.26	78.26	78.26	78.26	78.26
B^* (°)	1.883	1.883	1.883	1.883	1.883	1.883
$\tan B_{\text{eff}}$	0.1616	0.1616	0.1616	0.1616	0.1616	0.1616
A_{ra}^0 (km)	0.025		0.025		0.025	
λ_{ra}^0 (km)	1.04		1.04		1.04	
δ_{ra}^0 (°)	265		265		265	
A_{rb}^0 (km)	0.025			0.025		
λ_{rb}^0 (km)	1.20			1.20		
δ_{rb}^0 (°)	263			263		
A_{za}^0 (km)		0.025 $\tan B_{\text{eff}}$		0.025 $\tan B_{\text{eff}}$		
λ_{za}^0 (km)		1.04		1.04		
δ_{za}^0 (°)		$\delta_{ra}^0 - 90^\circ$		$\delta_{ra}^0 - 90^\circ$		
A_{zb}^0 (km)		0.025 $\tan B_{\text{eff}}$	0.025 $\tan B_{\text{eff}}$		0.025 $\tan B_{\text{eff}}$	
λ_{zb}^0 (km)		1.20	1.20		1.20	
δ_{zb}^0 (°)		$\delta_{rb}^0 - 90^\circ$	$\delta_{rb}^0 - 90^\circ$		$\delta_{rb}^0 - 90^\circ$	
A_{rc}^1 (km)					0.03/tan B_{eff}	0.03/tan B_{eff}
λ_{rc}^1 (km)					30	30
δ_{rc}^1 (°)					0.	0.
A_{zc}^1 (km)					0.03	0.03
λ_{zc}^1 (km)					30/0.9720	30/0.9720
δ_{zc}^1 (°)					$\delta_{rc}^1 - 90^\circ$	$\delta_{rc}^1 - 90^\circ$

models shown in Fig. 6. We adopt the geometric parameters for the RSS_133I_X25 event and include combinations of radial and vertical $m = 0$ and $m = 1$ modes. The relative phases and amplitudes of the $m = 0$ modes are adjusted so that the predicted optical depth profiles from Eqs. (63) and (66) are similar for a given wavelength λ_0 .

For each model, the left panel shows a horizontal view of the ring, shaded by color to reflect the variations in ring surface mass density associated with any radial modes. A representative occultation ray is shown as a dashed line with slope $\tan B_{\text{eff}}$. At right, the solid line shows the analytic model for the optical depth profile of the composite wave, and the result of a numerical ray tracing of the ring layer shown at left is plotted as a shaded gray band. In all cases, the ray tracing models closely match the expected analytic model, confirming the self-consistency between the physical model of the ring layer and the theoretical profile.

The models have the following properties:

- Model 1 corresponds to the simultaneous presence of two $m = 0$ radial modes (a and b) of identical amplitudes with closely spaced wavelengths $\lambda_{0ra} = 1.04$ km and $\lambda_{0ra} = 1.20$ km. The ring layer is flat, but with periodic variations in the surface mass density associated with the rarefaction and compression of the two radial waves. The resulting optical depth profile at right shows the beating signature as the two component waves change their relative phases, and qualitatively resembles the observations in Fig. 1.
- Model 2 is similar to the first model, except that two vertical modes are combined instead of two radial modes. In this case, the ring has a complex corrugated vertical structure of variable amplitude as the two waves change their relative phase. Once again, the ray tracing results at right agree with the analytic prediction, and the corresponding optical depth profile is very similar to that for Model 1.
- Model 3 combines an $m = 0$ radial mode from Model 1 and an $m = 0$ vertical mode from Model 2. In this case, the vertical corrugations vary sinusoidally and the surface mass density also varies sinusoidally, but with a slightly different wavelength. The ray tracing results at right closely resemble the previous two models.

- Model 4 swaps the radial and vertical $m = 0$ modes from Model 3. Notice that the wavelength of the vertical corrugations is shorter for this model than for Model 3, while the radial compressions indicated by the colored shading at left have a longer wavelength than for Model 3. Nevertheless, the resulting composite optical depth profile is nearly identical to that for Model 3.

A comparison of the results of Models 1–4 demonstrates that nearly identical optical depth profiles can be generated by four different combinations of radial and vertical modes, supporting the point made above that the signatures of radial and vertical modes are very similar. In the absence of independent evidence (e.g., a dependence on B_{eff} or ring longitude θ), the underlying physical nature of the two waves responsible for the observed beating pattern cannot be uniquely identified as vertical or radial modes.

- Model 5 adds to Model 1 by including radial and vertical $m = 1$ modes (labeled c) with wavelengths $\lambda_1 \sim 30$ km and a vertical corrugation amplitude of 0.03 km, comparable to the maximum value observed in the inner C ring by Hedman et al. (2011). Following Hedman et al. (2015), we assume that $\lambda_r^1/\lambda_z^1 = 0.9720$, which we confirm using Eqs. (26) and (27). The horizontal view of the ring clearly shows the long-wavelength undulations that are responsible for the resulting comparable variability of the background optical depth superimposed on the usual short-wavelength interacting $m = 0$ radial and vertical modes. The overplotted sinusoid at right corresponds to the radial optical depth profile predicted from the two $m = 1$ modes alone.
- Model 6 includes only the two $m = 1$ modes and spans a larger radial range. Because of the smaller fractional wavelength difference between the two $m = 1$ modes compared to the two $m = 0$ modes, it takes many wavelengths for their relative phases to drift by 360° . Consequently, the 600 km range contains less than one wavepacket.

These results show that additional evidence beyond the appearance of a single optical depth profile is required to characterize any modes that contribute to its overall structure. Furthermore, they demonstrate that the $m = 1$ corrugations visible in the Cassini ISS images may be evident in the low- $\tan B_{\text{eff}}$ occultation profiles as well if the vertical

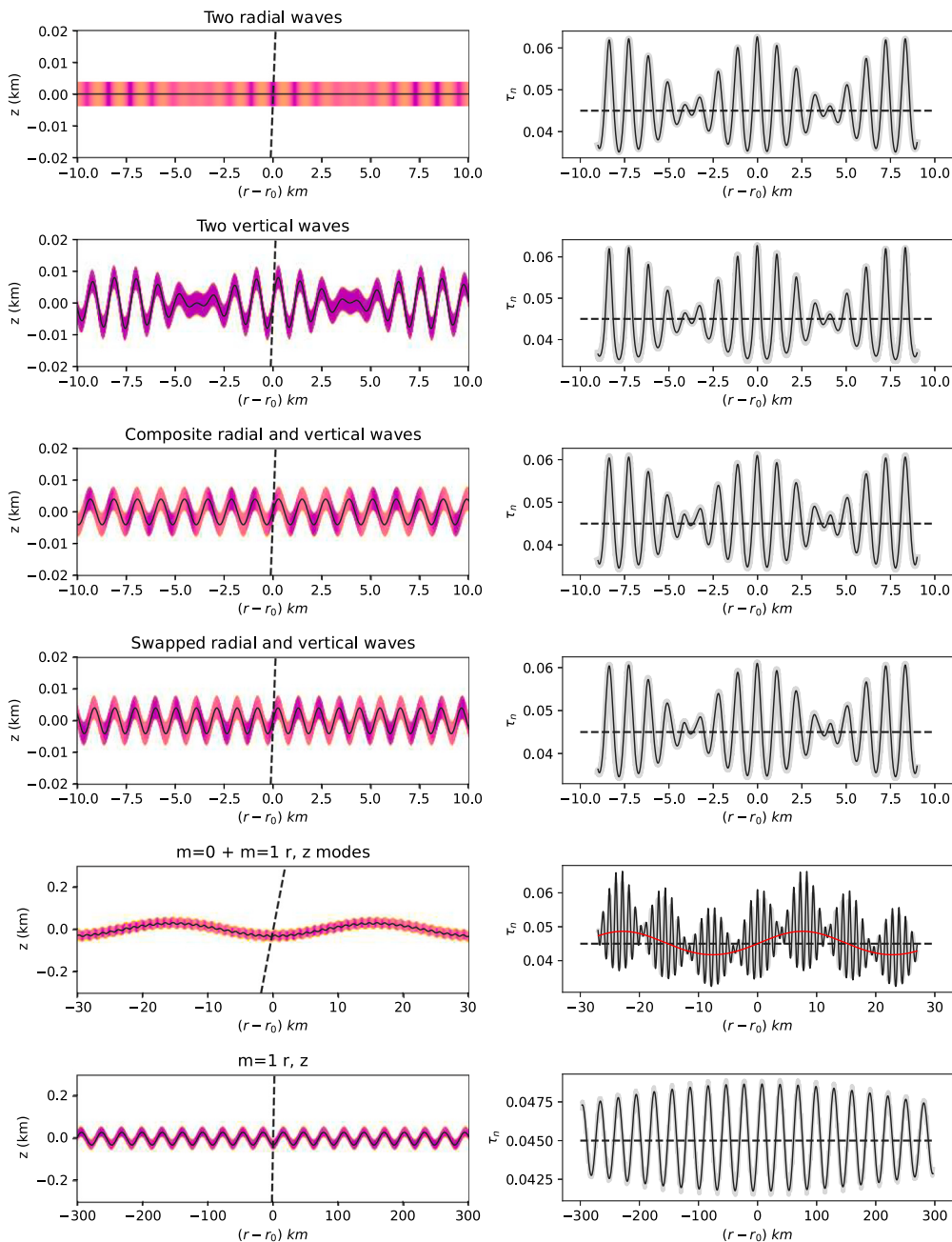


Fig. 6. Comparison of ray-tracing calculations and analytical composite models of a ring perturbed by combinations of radial and vertical normal modes. The left column of panels shows the side view of the ring, with colored shading representing the radial variation in surface mass density associated with radial modes and the vertical offset resulting from vertical modes. At right, the corresponding analytic composite optical depth profile $\tau_c(r)$ is shown as a solid line, and the numerical ray-tracing result is shown in shaded gray. Models 1–6 (described in the text) are shown from top to bottom. (For interpretation of the references to color in this figure legend, the reader is referred to the web version of this article.)

amplitudes are sufficiently large. We will show below that very little damping of the $m = 1$ corrugation amplitude is expected over timescales of decades.

4. Normal mode identification and inferred impact date

With this theoretical background in hand, we are in a position to identify the specific normal modes responsible for the observed beat patterns in the C ring ripple structure and to estimate the corresponding impact date for the proposed particle swarm that initially disturbed the ring. We begin by fitting two-component composite models to three observed wavetrains to determine the wavelengths of the contributing modes. We then compare the ratio of the two wavelengths to dynamical

predictions for a range of possible azimuthal wavenumbers for vertical and radial waves, and show that there are four possible combinations that match the observed values. Using a variety of arguments, we resolve this ambiguity and demonstrate that the ripple structure is due to the interference of $m = 0$ and $m = 2$ vertical waves of comparable amplitude. Given this identification, we show that the fitted wavelengths are consistent with an impact date in late 1983, the same time as the impact that produced the $m = 1$ corrugations in the C ring (Hedman et al., 2007, 2011, 2015). From the power spectra of radial optical depth profiles in the R75.5 region, we confirm that the strongest contributions to the observed periodic signals have the expected wavelengths for the candidate $m = 0$ and $m = 2$ vertical modes, with no detected signal for additional azimuthal wavenumbers other

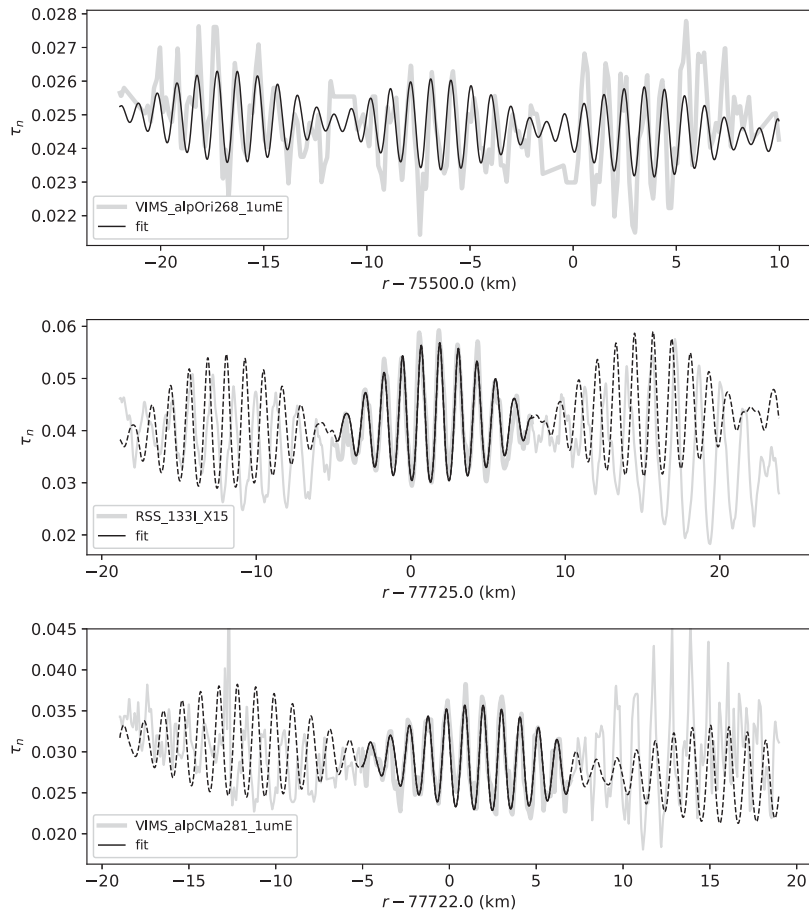


Fig. 7. Two-component composite fits to three inner C ring wavepackets. (Top) The 2017 April 6 VIMS_{alpOri268_1umE} occultation centered at $r_0 = 75,550$ km. (Middle) The 2010 June 18 RSS_{133I_X15} occultation centered at $r_0 = 77,725$ km. (Bottom) The 2017 June 27 VIMS_{alpCMa281_1umE} event occultation centered at $r_0 = 77,722$ km. The least-squares fit solves for the amplitudes, phases, and wavelengths of two vertical modes with $m = 0$ and $m = 2$. The observations are plotted in gray and the best-fitting model is shown as a solid line, extrapolated to the adjacent wavepackets as dashed lines for the two lower panels. The fitted parameters are given in Table 4.

than $m = 1$, which has marginal detections in the examples shown. Finally, using *Cassini* occultations between 2008–2017, we measure the time evolution of the vertical wavenumbers $k_z^0(r, t)$ and $k_z^2(r, t)$. We show that the empirically-estimated impact date is consistent with dynamical predictions of the windup rate of the $m = 0$ and $m = 2$ vertical corrugations, taking into account the effects of the self-gravity of the rings.

4.1. Wavepacket fits

From the gallery of occultation profiles shown in Figs. 4 and 5, we selected three examples that clearly exhibit the beat pattern of two $\lambda \sim 1$ km waves. The first is located in region R75.5: the VIMS_{alpOri268_1umE} wavetrain centered near 75,500 km. The other two are in the outer part of region R77.7: the RSS_{133I_X15} wavetrain centered near 77,725 km and the VIMS_{alpCMa281_1umE} wavetrain centered near 77,722 km, observed seven years later. We performed least-squares fits to portions of each wavetrain, solving for the best-fitting amplitudes, phases, and wavelengths of $m = 0$ vertical and radial modes, under the assumption that $k_z > k_r$, as expected theoretically for these modes (see Eq. (B.4)). (As noted above, the actual identity of the contributing modes cannot be determined from individual profiles, and we use the $m = 0$ vertical and radial components for simplicity.) The results of the fits are shown in Fig. 7 and the fitted parameters are given in Table 4.

The upper panel of Fig. 7 shows three contiguous wavepackets of VIMS_{alpOri268_1umE} optical depth profile in gray. This event was observed at incidence angle $B^* = 11.682^\circ$ and $\tan B_{\text{eff}} = 0.5316$, providing modest sensitivity to vertical corrugations. The overplotted solid curve shows the best-fitting two-component model to all three wavepackets, which nicely matches the observed phases of the ripple pattern across the entire radial region shown, with fitted amplitudes $A_z^0 = 2.56 \pm 0.11$ m, $A_r^0 = 3.76 \pm 0.24$ m (with equivalent vertical amplitude $A^0 \tan B_{\text{eff}} = 2.00 \pm 0.13$ m, as noted previously in Section 3.6.2), and wavelengths $\lambda_z^0 = 0.9403 \pm 0.0007$ km and $\lambda_r^0 = 1.0369 \pm 0.0012$ km. The ratios $k_z^0/k_r^0 = 1.1027$ and $k_r^0/k_z^0 = 0.9069$ are included in Table 4 for later identification of the possible modes responsible for the observed ripple structure.

The middle panel shows three wavepackets from the RSS_{133I_X15} occultation in 2010. This event was observed at low incidence angle $B^* = 1.883^\circ$ with $\tan B_{\text{eff}} = 0.1622$, providing excellent sensitivity to vertical corrugations. The overplotted solid curve shows the best-fitting two-component model, which nicely matches the ~ 10 peaks of the central wavepacket, with fitted amplitudes $A_z^0 = 4.44 \pm 0.25$ m and $A_r^0 = 33.24 \pm 1.46$ m, with equivalent vertical amplitude $A^0 \tan B_{\text{eff}} = 5.39 \pm 0.24$ m. The fitted wavelengths $\lambda_z^0 = 1.1502 \pm 0.0040$ km and $\lambda_r^0 = 1.2561 \pm 0.0044$ km have corresponding ratios $k_z^0/k_r^0 = 1.0921$ and $k_r^0/k_z^0 = 0.9157$. The dashed line shows the extrapolation of the model fit to the two adjacent wavepackets, exhibiting a clear phase drift over the 40 km width of the region shown. More elaborate fits that attempted to model the radial distortion due to the nearby Titan 1:0

Table 4
Wavepacket fits with two arbitrary modes.

Parameter ^a	VIMS_alpOri268_1umE	RSS_133E_X15	VIMS_alpCMa281_1umE
r_0 (km)	75 500.0	77 725.0	77 722.0
B^* ($^\circ$)	11.6819	1.8833	-13.4824
$\tan B_{\text{eff}}$	0.5317	0.1622	0.4745
A_z^0 (m)	2.56 ± 0.11	4.44 ± 0.25	6.55 ± 0.59
A_r^0 (m) ^b	3.76 ± 0.24	33.24 ± 1.46	23.59 ± 1.22
$A_r^0 \tan B_{\text{eff}}$ (m)	2.00 ± 0.13	5.39 ± 0.24	11.20 ± 0.58
λ_z^0 (km)	0.9403 ± 0.0007	1.1502 ± 0.0040	1.0099 ± 0.0050
λ_r^0 (km)	1.0369 ± 0.0012	1.2561 ± 0.0044	1.0898 ± 0.0036
k_z^0 (km $^{-1}$)	6.6819	5.4628	6.2218
k_r^0 (km $^{-1}$)	6.0597	5.0022	5.7652
k_z^0/k_r^0	1.1027	1.0921	1.0792
k_r^0/k_z^0	0.9069	0.9157	0.9266
τ_n	0.0245 ± 0.0000	0.0402 ± 0.0001	0.0285 ± 0.0001
t (yr)	2017.2634	2010.4626	2017.4880

^a Assuming $k_z^0 > k_r^0$.

^b A_r^0 is the amplitude of the assumed radial mode. If instead it is a vertical mode, its vertical amplitude is $A_r^0 \tan B_{\text{eff}}$.

resonance, or that included the gradual compression/rarefaction due to a longer-wavelength $m = 1$ mode, did not result in an improved regional fit. Nevertheless, the simple model does reliably match the central wavepacket.

The lower panel shows the corresponding results for the VIMS alpCMa281_1umE wavetrain. This event was observed at a more modest ring opening angle $B^* = -13.482^\circ$ but with a favorable viewing angle ϕ , resulting in $|\tan B_{\text{eff}}| = 0.4745 < 1$, providing somewhat enhanced sensitivity to vertical structure. Again, the best-fitting two-component model matches the ~ 10 peaks of the central wavepacket, with fitted amplitudes $A_z^0 = 6.55 \pm 0.59$ m, $A_r^0 = 23.59 \pm 1.22$ m, and equivalent vertical amplitude $A_r^0 \tan B_{\text{eff}} = 11.20 \pm 0.58$ m. The fitted wavelengths $\lambda_z^0 = 1.0099 \pm 0.0050$ km and $\lambda_r^0 = 1.0898 \pm 0.0036$ km have corresponding ratios $k_z^0/k_r^0 = 1.0792$ and $k_r^0/k_z^0 = 0.9266$. Notably, the fitted wavelengths are significantly shorter than those for the RSS_133I_X15 event observed seven years earlier, a clear indication of time evolution of the two separate ripple patterns. As before, while the model nicely fits the central wavepacket, it drifts out of phase when extrapolated to the adjacent wavepackets on each side.

4.2. Normal mode identification

4.2.1. Candidate modes

The wavepacket fits shown in Fig. 7, while admittedly imperfect in matching the observed ring structure in detail, nevertheless are sufficiently robust to restrict the possible combinations of vertical and radial modes and azimuthal wavenumbers that match the measured properties of the interacting waves. The dynamically predicted wavenumbers k_a and k_b for any two candidate vertical or radial modes of azimuthal wavenumbers m_a and m_b vary with time since impact Δt and with orbital radius r_0 , but in the absence of self-gravity, their ratios are independent of time, as seen from Eqs. (36) and (37), and thus contain no assumptions about the time history of the ripple structure.

In Table 5, we list k_a and k_b , their equivalent radial wavelengths λ_a and λ_b , and the ratios k_a/k_b and k_b/k_a for combinations of radial and vertical modes with m from -3 to 5, computed from Eqs. (26)–(37) for the circumstances and geometry of the three wavepacket fits shown in Fig. 7, assuming $t_i = 1983.7$, the approximate date of the proposed impact that produced detectable $m = 1$ corrugations in the C ring (Hedman et al., 2011). At the top of each section of the table, we include the results of the wavepacket fits for an event from Table 4. We assumed that $k_z^0 > k_r^0$ in our wavepacket fits, but this was an arbitrary choice, and as we showed both analytically and from ray tracing, it is not possible from the shape of an observed wavepacket alone to identify

whether the contributing modes are radial or horizontal. Instead, we compare both the fitted ratio k_a/k_b and its inverse to the predictions for each listed combination of vertical and radial modes for m_a and m_b . We seek tabulated values of k_a/k_b or k_b/k_a in each section of the table closest to the observed ratios 1.1027 for the $t = 2017.2634$ VIMS alpOri268_1umE wavepacket at $r_0 = 75,500$ km, 1.0921 for the $t = 2010.4626$ RSS_133I wavepacket at $r_0 = 77,725$ km, and 1.0792 for the $t = 2017.4880$ VIMS alpCMa281_1umE wavepacket at $r_0 = 77,722$ km.

A checkmark in the right-hand column indicates a potential match between the calculated and observed wavenumbers, as derived from fits to the beat patterns in Fig. 7. Note that, because of the degeneracy described in Section 3.3, models with both radial and vertical $m = 0$ perturbations, radial and vertical $m = 2$ perturbations, $m = 0$ and 2 radial perturbations and $m = 0$ and 2 vertical perturbations can all fit the observed ripple wavelengths and beat frequencies equally well, although the interpretation of the individual periodic signals varies between the four cases. On the other hand, a mixed combination of $m = 0$ radial and $m = 2$ vertical oscillations, or vice versa, does not work because these pairs of modes have almost identical wavenumbers, as noted above.

This provisional identification of the perturbations responsible for the ~ 1 km ripple structure can be strengthened by comparing the fitted wavelengths themselves (rather than just their ratios) to the predicted values, assuming $t_i = 1983.7$. The same combinations of checkmarked $m = 0$ and $m = 2$ modes pass these tests as well: the VIMS alpOri268_1umE wavelengths $\lambda = 0.94$ and 1.04 km closely match the predicted values of 0.95 and 1.03 km, the RSS_133I wavelengths 1.15 and 1.26 km come closest to matching the predicted values of 1.28 and 1.39 km, and the VIMS alpCMa281_1umE wavelengths 1.01 and 1.09 km are very similar to the predicted values of 1.02 and 1.10 km. On the other hand, the predicted wavelengths for m other than 0, 1, or 2 are all less than 0.68 km, well below the wavelengths of the components of the observed ripple patterns.

4.2.2. Resolving the ambiguity of the mode identification

At this point, we have four candidate pairs of modes that match the observed C ring ripple wavenumbers/wavelengths and their ratios:

- A: k_z^0 and k_r^0 (a vertical and a radial mode, each with $m = 0$)
- B: k_z^2 and k_r^2 (a vertical and a radial mode, each with $m = 2$)
- C: k_z^0 and k_z^2 (two vertical modes, with $m = 0$ and $m = 2$)
- D: k_r^0 and k_r^2 (two radial modes, with $m = 0$ and $m = 2$).

We reject the two other potential combinations of $m = 0$ and $m = 2$ modes because (contrary to the observations) both components in each pair have the same wavelength:

- E: k_r^0 and k_z^2 (a radial $m = 0$ mode and a vertical $m = 2$ mode)
- F: k_r^2 and k_z^0 (a radial $m = 2$ mode and a vertical $m = 0$ mode).

In the wavepacket fits shown in Fig. 7, we assumed model A, but any of the four options (A through D) would have given nearly identical fitted lightcurves, different only in the phases of the component waves and the interpretation of the mode amplitudes as vertical corrugations or radial perturbations, which differ by a factor of $\tan B_{\text{eff}}$. However, we can use the fitted parameters for each of the four models for a given wavepacket to predict the detailed ripple structure in the same radial location for a second observation at a different time and ring longitude, which differentially affect the model predictions. A model is favored that consistently gives closer matches than the others. To limit the magnified effects of small errors in pattern speeds propagated over long time intervals, we restrict our attention primarily to ingress/egress pairs of a given occultation that show the same wavepacket near the same location in both profiles.

We illustrate this approach in Fig. 8. In the upper left panel, we show a single wavepacket from the RSS_133I_X15 occultation near

Table 5
Azimuthal wavenumber identification from wave packet fits.

m_a		m_b		k_a/k_b	k_b/k_a	λ_a (km)	λ_b (km)	Match
VIMS_alpOri268_1umE^c								
-3	z	-3	r	1.0208	0.9796	0.2441	0.2492	
-2	z	-2	r	1.0278	0.9729	0.3244	0.3335	
-1	z	-1	r	1.0420	0.9596	0.4834	0.5038	
0	z	0	r	1.0859	0.9209	0.9481	1.0295	✓
1	r	1	z	1.0324	0.9686	23.5851	24.3502	
2	z	2	r	0.9210	1.0858	1.0281	0.9469	✓
2	r	0	z	1.0013	0.9987	0.9469	0.9481	
2	z	0	r	1.0014	0.9986	1.0281	1.0295	
2	z	0	z	0.9221	1.0844	1.0281	0.9481	✓
2	r	0	r	1.0873	0.9197	0.9469	1.0295	✓
3	z	3	r	0.9597	1.0420	0.5034	0.4831	
4	z	4	r	0.9729	1.0278	0.3333	0.3243	
5	z	5	r	0.9796	1.0208	0.2491	0.2441	
RSS_133I_X15^c								
-3	z	-3	r	1.0195	0.9809	0.3298	0.3363	
-2	z	-2	r	1.0260	0.9746	0.4384	0.4498	
-1	z	-1	r	1.0393	0.9622	0.6535	0.6792	
0	z	0	r	1.0803	0.9257	1.2831	1.3861	✓
1	r	1	z	1.0299	0.9710	34.0436	35.0600	
2	z	2	r	0.9258	1.0802	1.3845	1.2817	✓
2	r	0	z	1.0011	0.9989	1.2817	1.2831	
2	z	0	r	1.0012	0.9988	1.3845	1.3861	
2	z	0	z	0.9268	1.0790	1.3845	1.2831	✓
2	r	0	r	1.0814	0.9247	1.2817	1.3861	✓
3	z	3	r	0.9622	1.0393	0.6788	0.6532	
4	z	4	r	0.9746	1.0260	0.4497	0.4382	
5	z	5	r	0.9809	1.0195	0.3362	0.3297	
VIMS_alpCMa281_1umE^c								
-3	z	-3	r	1.0195	0.9809	0.2612	0.2663	
-2	z	-2	r	1.0260	0.9746	0.3472	0.3563	
-1	z	-1	r	1.0393	0.9622	0.5176	0.5379	
0	z	0	r	1.0803	0.9257	1.0162	1.0978	✓
1	r	1	z	1.0299	0.9710	26.9600	27.7650	
2	z	2	r	0.9258	1.0802	1.0965	1.0151	✓
2	r	0	z	1.0011	0.9989	1.0151	1.0162	
2	z	0	r	1.0012	0.9988	1.0965	1.0978	
2	z	0	z	0.9268	1.0790	1.0965	1.0162	✓
2	r	0	r	1.0814	0.9247	1.0151	1.0978	✓
3	z	3	r	0.9622	1.0393	0.5376	0.5173	
4	z	4	r	0.9746	1.0260	0.3561	0.3471	
5	z	5	r	0.9809	1.0195	0.2662	0.2612	

^a Computed from Eqs. (26)–(37) for each m at the specified r_0 in Table 4.

^b Computed from Eqs. (26)–(37) for each m at the specified r_0 and t in Table 4, assuming $t_i = 1983.7$.

^c Entries from wave packet fits in Table 4.

$r_0 = 77,725$ km (the same feature shown in the middle panel of Fig. 7). The best-fitting profiles for models A through D are overplotted, and as expected are nearly identical to each other. In the upper right panel, we show the egress profile (RSS_133E_X15) at the same radial location and the corresponding best-fitting model fits to this wavepacket. Qualitatively, the ingress and egress wavepackets appear to be quite similar in general form. In the four panels below, we show the RSS_133E_X15 profile again (in blue), along with the predicted ripple pattern (shown as an orange dashed line) computed using the RSS_133I_X15 fitted parameters in turn for each of the four models A through D, moving across and then down from middle left to lower right. The legend in each panel identifies the modes corresponding to case, and lists the RMS difference (σ) between the observations and the predicted wavepacket. Only model C (lower left) shows a good match of the phase and overall shape of the egress wavepacket, with the lowest σ of the four comparisons.

As a second example, in Fig. 9, we use the same two RSS datasets to compare a wavepacket in the R75.5 region (with $r_0 = 75,555$ km). Once again, the closest match is given by model C at the lower left. The phases of the model and observed wavepacket match well, and although the observed and modeled amplitudes of the individual peaks

differ somewhat for model C, the other three models (A, B, and D) give much poorer matches.

We carried out a similar exercise for several other observations that had ingress/egress pairs of identifiable wavepackets located at similar orbital radii. In most cases, model C provided a uniquely good match to the comparison observations, with some exceptions where no models provided a good match, possibly due to slight errors in the ring plane radius scale or unmodeled radial perturbations. Evidently, there are regions in the rings where our simple two-component model is not sufficient to capture the observed variations in ripple structure over time, ring longitude and viewing geometry.

As a variant on these comparisons, we can take advantage of the fact that among models A through D, only model C has no radial modes. In the galleries in Figs. 4 and 5, the lowest $|\tan B_{\text{eff}}|$ data sets show the most prominent ripples, supporting the idea that at least one of the ripple components is a vertical corrugation. However, as shown from Eqs. (65) and (66), the fractional optical depth variation due to a radial wave is independent of $\tan B_{\text{eff}}$ and should be equally visible in high-SNR occultations at both low and high $|\tan B_{\text{eff}}|$. In Fig. 10, we compare the model predictions from the RSS_133E_X15 wavepacket fits near $r_0 = 77,725$ km given in Table 4, scaled in wavelength to

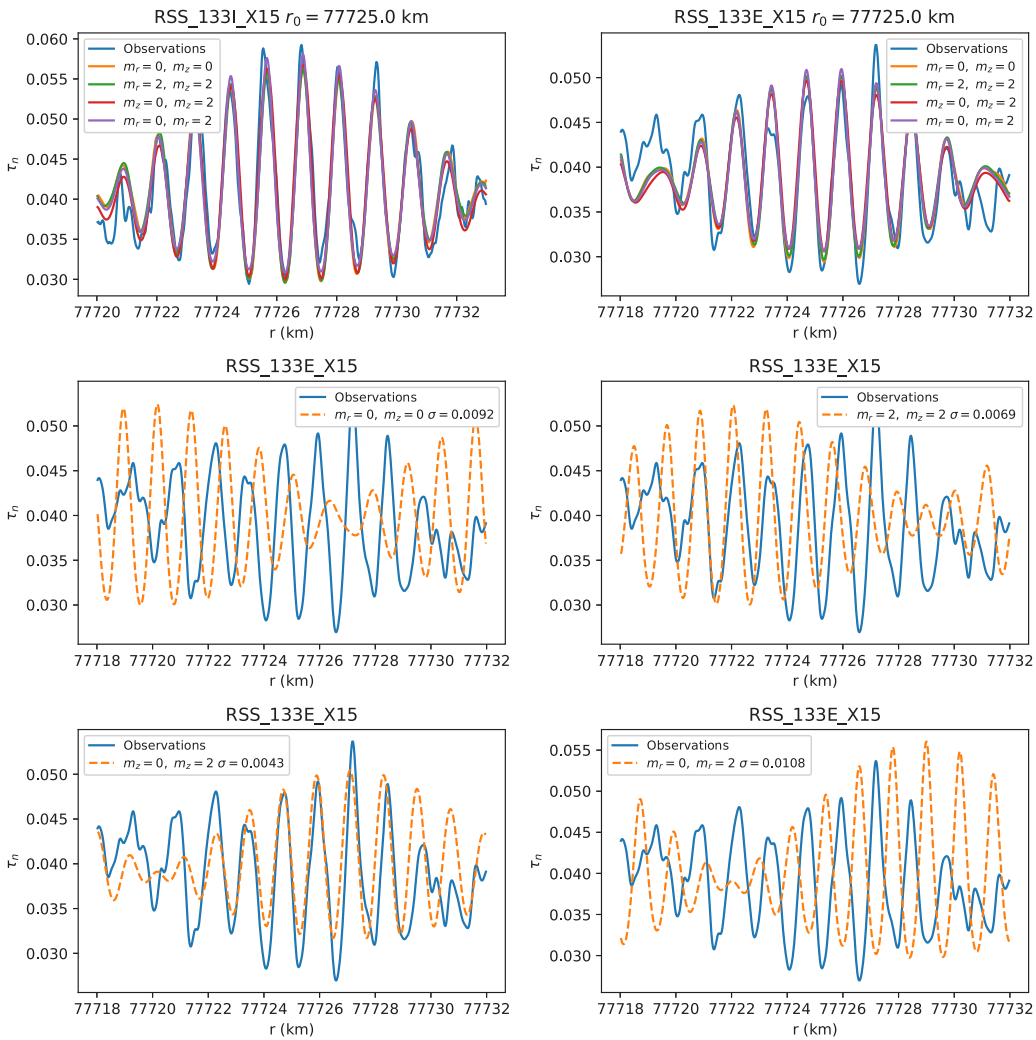


Fig. 8. Comparison of fits to the RSS_133E_X15 wavepacket near $r_0 = 77,725$ km, and the corresponding predicted ripple patterns for RSS_133I_X15 in R77.5, for models A through D. The upper row shows the RSS_133E_X15 and RSS_133I_X15 observations and the best-fitting model curves. The middle and lower rows compare the observed RSS_133I_X15 wavepacket (in blue) and the predicted pattern (dashed orange line) using the geometry and time of the RSS_133I_X15 event but the model parameters from RSS_133E_X15 for each of the four cases A through D, from middle left to lower right. Only the model C (two vertical modes, with $m = 0$ and $m = 2$) predictions from the egress fits match the general shape and phase of the ingress wavepacket. (For interpretation of the references to color in this figure legend, the reader is referred to the web version of this article.)

match the expected values for the high-SNR VIMS_alpSco243_1umE event. Near the radial region shown, $|\tan B_{\text{eff}}| = 104.4$, making it quite insensitive to detecting vertical structure in the rings. Each panel shows the observed optical depth profile for VIMS_alpSco243_1umE event (blue), and the predicted profiles (dashed orange lines) sequentially for models A through D from upper left to lower right. Models A and B each have a radial and a vertical mode. Because of the unfavorable viewing geometry, the vertical wave is absent from the predicted models, and the predicted radial mode appears as a pure sinusoid. In both cases, the model amplitude is well above the noise level of the observations, suggesting a radial mode with an amplitude $A_r = 33$ m (Table 4) would be readily detected in the VIMS_alpSco243_1umE data. Model D at lower right has two radial modes of different wavelengths and comparable amplitudes, resulting in the familiar wavepacket appearance of the two interfering modes. Again, the model profile has optical depth variations much larger than in the observations. Finally, the model C predictions at lower left show a flat model optical depth profile, indicating that neither vertical mode would be detectable for the geometry of the VIMS_alpSco243_1umE event at this radius.

In an additional series of tests, we searched the VIMS_alpSco241, VIMS_alpSco243, and VIMS_alpSco245 egress profiles for evidence of

~ 1 km periodic structure comparable to the more obvious ripples in low-incidence observations. The most prominent such structure (other than just interior to the Titan 1:0 resonance) is visible in the VIMS_alpSco243E profile near $r_0 = 75,556$ km, shown in Fig. 11. The periodic structure appears to be real, but it has a wavelength of about 0.75 km, well below the expected wavelengths of 0.96–1.05 km from the model predictions at this radius and event date for $m = 0$ or $m = 2$ vertical or radial modes, and does not appear to be related to the 1983.7 impact event.

Taken together, the detailed wavepacket comparisons of the four candidate models and the absence of any sign of radial structure of the expected wavelengths associated with radial modes for $m = 0$ or $m = 2$ demonstrate that only model C, with two vertical modes of wavenumber $m = 0$ and $m = 2$, is compatible with the observations. In Section 4.6, where we compare the signatures of ring self-gravity in the time variation of radial and vertical modes, we will show that there is additional strong evidence favoring model C. Henceforth, we will assume that the ripple structure can be described physically as two vertical corrugations with slightly different radial wavelengths. Furthermore, the fact that the wavepackets show nulls between adjacent phase bundles suggests that the $m = 0$ and $m = 2$ vertical modes have roughly comparable amplitudes.

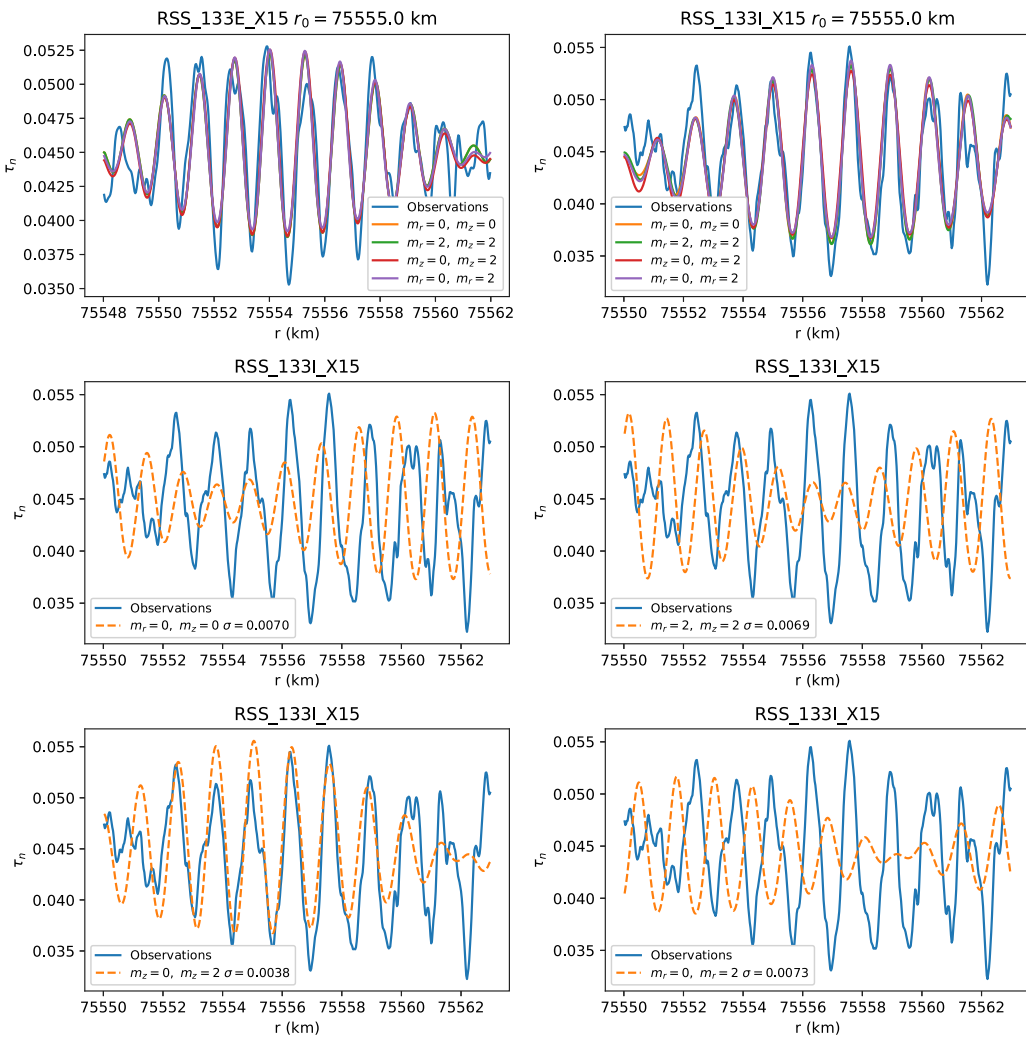


Fig. 9. Comparison of fits to the RSS_133E_X15 wavepacket near $r_0 = 75,555$ km, and the corresponding predicted ripple patterns for RSS_133I_X15 in R77.5, for models A through D. See caption for Fig. 8 for additional details. Model C (lower left) gives the best match between the ingress observations and the egress models, propagated to the time and geometry of ingress profile.

4.3. Regional power spectral analysis

The results in hand provide strong evidence that the initial disturbance that produced the observed $m = 1$ modes detected by Hedman et al. (2011) also produced the $m = 0$ and $m = 2$ vertical corrugations detected in the occultation profiles considered here. However, the imprecision of the wavepacket fits over a very restricted range of radii severely limits the accuracy of the inferred windup rates of the two corrugation patterns. To make further progress, we turn to spectral analysis of the occultation observations over a much larger radial range.

4.3.1. Power spectra of km-scale radial structure

We note first that since the putative spiral patterns for all $m \neq 1$ have radially-dependent wavenumber $k(a) \propto |\partial n/\partial a| \propto a^{-5/2}$, the search for signatures of spirals can be considerably improved by adopting a revised radius scale prior to computing the power spectrum that compensates for this expected dispersion. Following Hedman et al. (2015), we first transform the observed ring radius r into a rescaled distance parameter d given by

$$d = \frac{2r}{3} \left(\frac{r_0}{r} \right)^{5/2}, \quad (69)$$

where r_0 is a specified reference radius and the factor of 2/3 is chosen so that the wavelength of a feature at r_0 is the same in both the actual radius and rescaled distance (*i.e.*, that $|\partial d/\partial r| = 1$ when $r = r_0$). For

modes with pattern speeds given by the mean motion n , the rescaled wavelength across the range of the power spectrum should be roughly constant. The spectral power is computed using a continuous Fourier transform (CFT), where the power at a given wavenumber k (where $k/2\pi = 1/\lambda$) is given by

$$P(k) = \left[\sum_j \tau_n(r_j) e^{-ik(r_j - r_0)} \right]^2, \quad (70)$$

and r is either the nominal radius or the rescaled distance d . Note that the CFT power estimates are not normalized or orthogonal and therefore cannot be directly compared to the power from a standard Fourier transform, but they provide a means of localizing the peaks in the power spectrum at a higher resolution. In practice, we compute $P(k)$ with a very fine mesh ($\delta k/k = 0.0001$) to provide an accurate estimate of the wavenumber of any peak found in the power spectrum.

In Fig. 12, we show the power spectra of the optical depth profiles from three low-incidence observations, plotted as a function of wavelength and computed over the radial range 75,100–75,675 km (region R75.4), chosen because it is the longest interval of roughly constant low optical depth in the inner C ring with visible ripple structure throughout. The predicted wavelengths at a reference radius $r_0 = 75,400$ km for radial and vertical modes for azimuthal wavenumbers $m = -3, -2, -2, 0, 2$, and 3 are plotted as vertical lines, assuming $t_i = 1983.7$. (As noted above, several modes have the same predicted

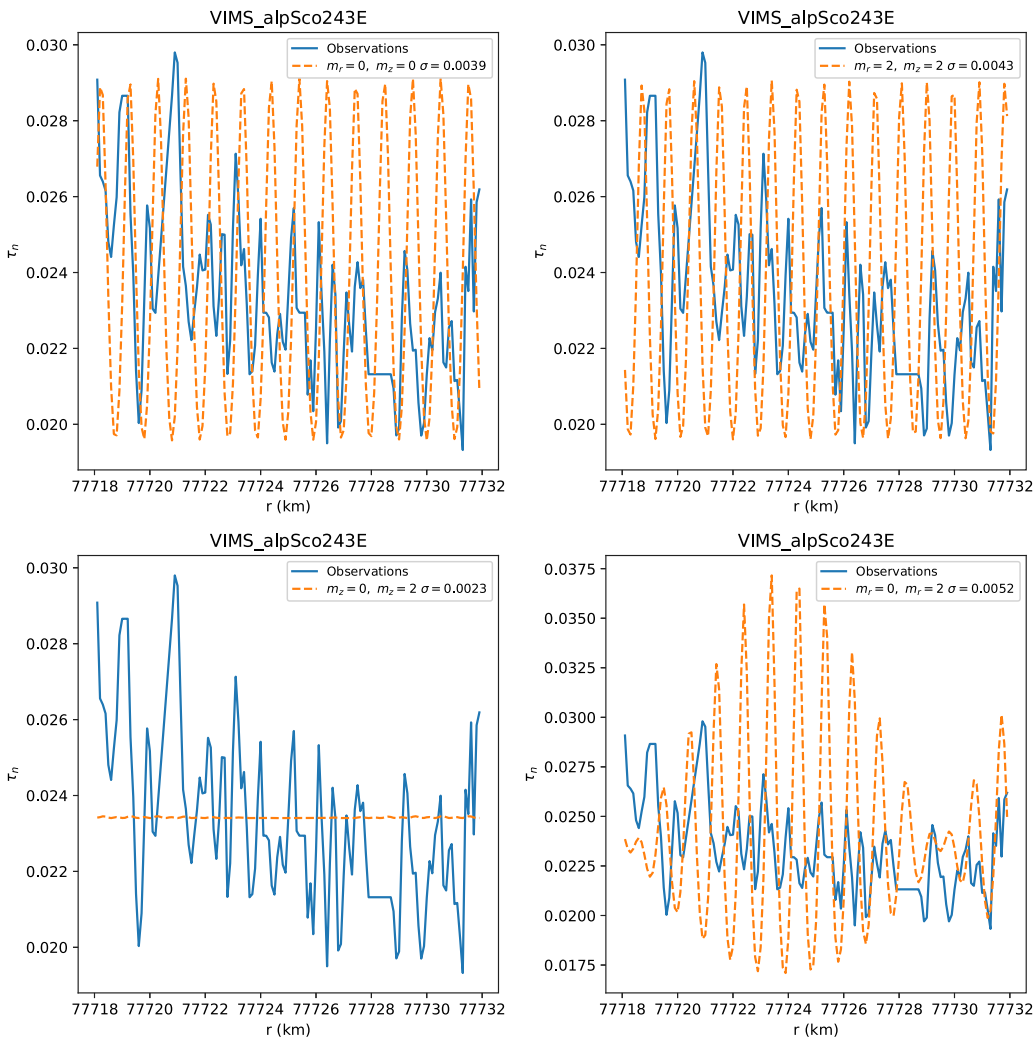


Fig. 10. Comparison of the observed VIMS_alfSco243_1umE optical depth profile near $r_0 = 77,723$ km (shown in blue) and predictions (shown as dashed orange lines) from the corresponding RSS_133E_X15 wavepacket fits for each of the four models A through D from upper left to lower right. The model wavelengths were scaled to compensate for the six year interval between the observations. The unfavorable viewing geometry of the VIMS_alfSco243_1umE occultation for vertical waves results in model profiles that show only radial modes. For models A and B, a single radial mode is present, resulting in a constant-amplitude sinusoids for both cases. For model D, two radial modes of slightly different wavelength beat against each other, resulting the wavepacket bundle at lower right. For model C (lower left), with two vertical modes, the predicted signal is a flat line. For all other cases, however, the model predictions exceed the SNR of the VIMS data and the corresponding modeled radial modes would be easily detectable if present. (For interpretation of the references to color in this figure legend, the reader is referred to the web version of this article.)

wavelengths, resulting in overplotted vertical lines.) The upper panels show the power spectra computed using the nominal observed radius scale, plotted as a function of radial wavelength. The bottom panels show the power spectra computed using the rescaled distance, plotted as a function of the corresponding wavelength at reference radius $r_0 = 75,400$ km. In both cases, the power is normalized to 100 for the maximum power observed in the vicinity of the expected wavelengths for $m = 0$ and $m = 2$ vertical modes.

Qualitatively, the power spectra for all three observations have similar characteristics. Using the nominal radius scale, the top row shows a broad and somewhat noisy pedestal of power in each spectrum near the expected wavelengths for the $m = 0$ and $m = 2$ vertical modes at the time of each observation. Using the rescaled distance instead, the bottom row isolates the power into two narrow peaks, in most cases centered near the expected wavelengths for the time of the observation based on an impact date of 1983.7, supporting the inference from the wavepacket fits that the periodic structure visible in Fig. 4 is associated with $m = 0$ and $m = 2$ vertical modes. There are no such peaks near any of the predicted wavelengths for other values of m , assuming that $t_i = 1983.7$.

Looking at the results in Fig. 12 in more detail, the left column of panels shows the results for the RSS_125I_X34 event observed at $t = 2010.0707$. In the bottom panel, there are two isolated power peaks that fall almost exactly on the predicted wavelengths for the $m = 0$ and $m = 2$ vertical modes. To provide an estimate of the physical amplitude of the two modes, we computed $P(k)$ for the predicted wavelengths of the modes at time t and effective incidence angle $\tan B_{\text{eff}}$, and solved iteratively for the amplitudes A_z^0 and A_z^2 in the model that yielded the observed power at the two predicted wavelengths. In this case, $A_z^2 = 1.52$ m and $A_z^0 = 1.68$ m. The middle column shows the results for the very low inclination UVIS_IotOri_159E event observed two years later at $t = 2012.0085$. The predicted wavelengths are shorter than for the RSS_125I_X34 event and the observed spectrum shows a sharp peak near the predicted wavelength of the $m = 2$ vertical mode and a weaker peak at the predicted wavelength of the $m = 0$ vertical mode, with substantial power over the entire wavelength range $\lambda = 0.95\text{--}1.45$ km. The occulted star ι Ori is a multiple star system and the observed optical depth profile shows radially offset contributions from at least three stars. This is likely to be responsible in part for the differences in the appearance between the RSS_125I_X34 results and

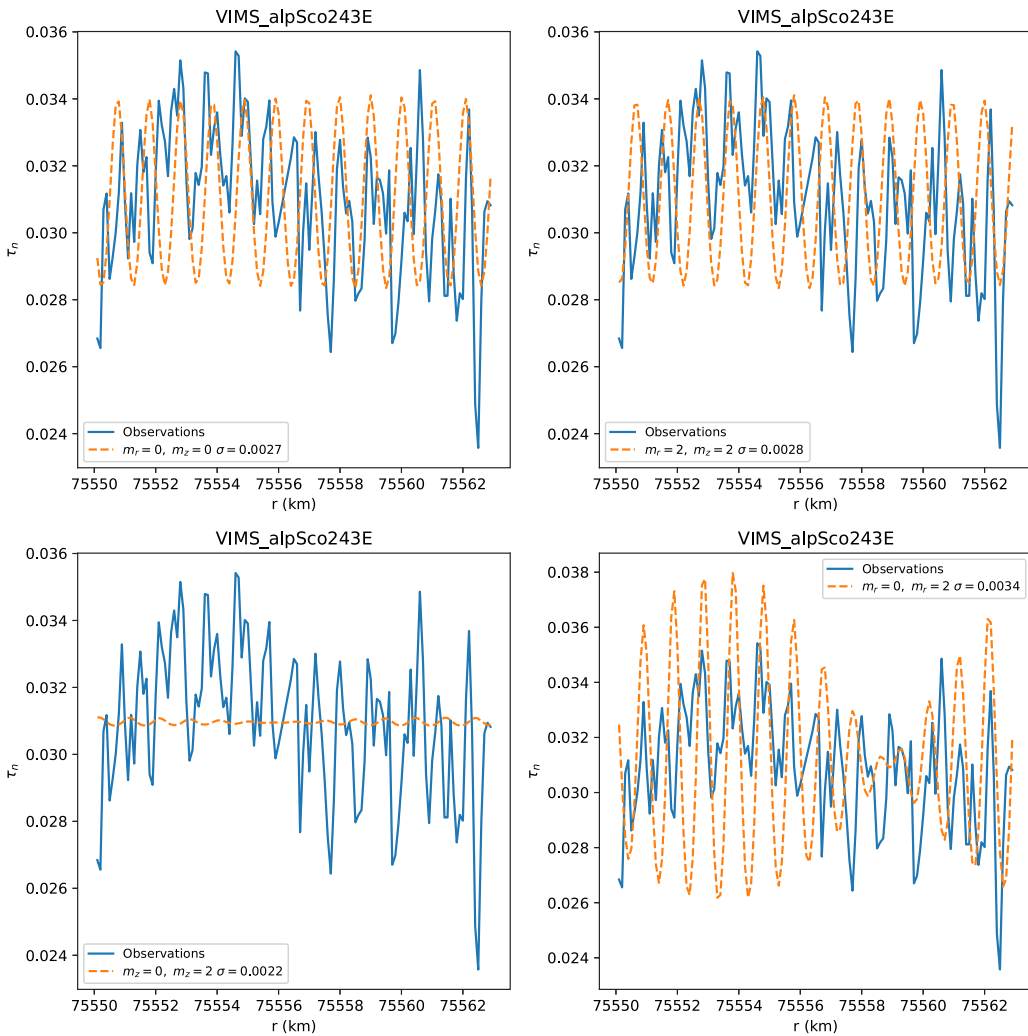


Fig. 11. The VIMS_alfSco243.1umE occultation profile near $r_0 = 75,556$ km, showing periodic structure of unknown origin. Model predictions based on combinations of $m = 0$ and $m = 2$ radial and vertical modes for the radius and date of the observations all show wavelengths ≈ 1 km, substantially longer than the estimated ~ 0.75 m wavelength of the observed periodic structure, which therefore does not seem to be associated with the ripples seen in low-incidence angle occultations.

the UVIS power spectra. The inferred amplitudes of the two modes are $A_z^2 = 0.45$ m and $A_z^0 = 0.27$ m. The right column shows the results for the VIMS_alfOri277.1uml event observed at $t = 2017.4251$, 5.4 years after the UVIS_IotOri_159E observation. The predicted wavelengths are shifted to even lower values because of the further windup of the waves. Here, there is a conspicuous pair of narrow peaks in observed power in the bottom right plot centered on the predicted wavelengths, with derived amplitudes $A_z^2 = 0.93$ m and $A_z^0 = 0.80$ m.

4.3.2. Evidence for 30-km scale $m = 1$ structure

We now examine the same three observations for evidence of the $m = 1$ structure detected in the C ring by Hedman et al. (2011). Fig. 13 shows the power spectra of the observations computed using a conventional Fourier transform over the radial range 75,100–75,675 km after rebinning the data to a uniform radial resolution of 1 km. As seen in Table 5, the predicted $m = 1$ radial and vertical wavelengths are closely spaced, differing by only a few percent, which is below the fractional resolution of the power spectrum over the relatively narrow radial range compared to the expected wavelength $\lambda \sim 30$ km for significant power for $m = 1$. There are peaks in each of the three spectra in the vicinity of the predicted $m = 1$ locations, with the wavelength of maximum power decreasing with time, as expected for a gradually tightening corrugation pattern. The RSS_1251_X34 spectrum shows a pronounced peak near $\lambda = 32$ km, a bit larger than the predicted $m_z = 1$

value. The UVIS_IotOri_159E event shows an isolated peak near the predicted $m = 1$ mode wavelengths, although the close spacing of the radial and vertical wavelengths makes it impossible to identify the relative contributions of either mode. Finally, the VIMS_alfOri277.1uml power spectrum shows an isolated peak in the general vicinity of $\lambda = 24$ km, with a subsidiary peak in power near $\lambda = 19$ km.

These results provide suggestive but not conclusive evidence for the detection of $\lambda = 25$ –35 km periodic signatures in the optical depth profiles associated with the $m = 1$ disturbance from the 1983.7 impact. Note that the radial range of 650 km used for these power spectra corresponds to only about 20 cycles, limiting the spectral resolution, so that it is not possible to distinguish between the possible contributions of $m = 1$ vertical and radial modes. Hedman et al. (2011) concluded that the periodic 30-km scale structure in Cassini ISS images of the C ring represented vertical corrugations, and in Figs. 1 and 2 we show that the undulatory signatures in the optical depth profiles at this scale are plausibly matched by $m = 1$ vertical corrugations with amplitude of order $A_z^1 \sim 100$ m, larger by a factor of several than the amplitude inferred by Hedman et al. (2011) from photometric estimates averaged over 500 km, but somewhat smaller than the inferred vertical amplitude of several hundred m for the D ring ripple structure attributed to the 1983.7 impact (Hedman et al., 2015).

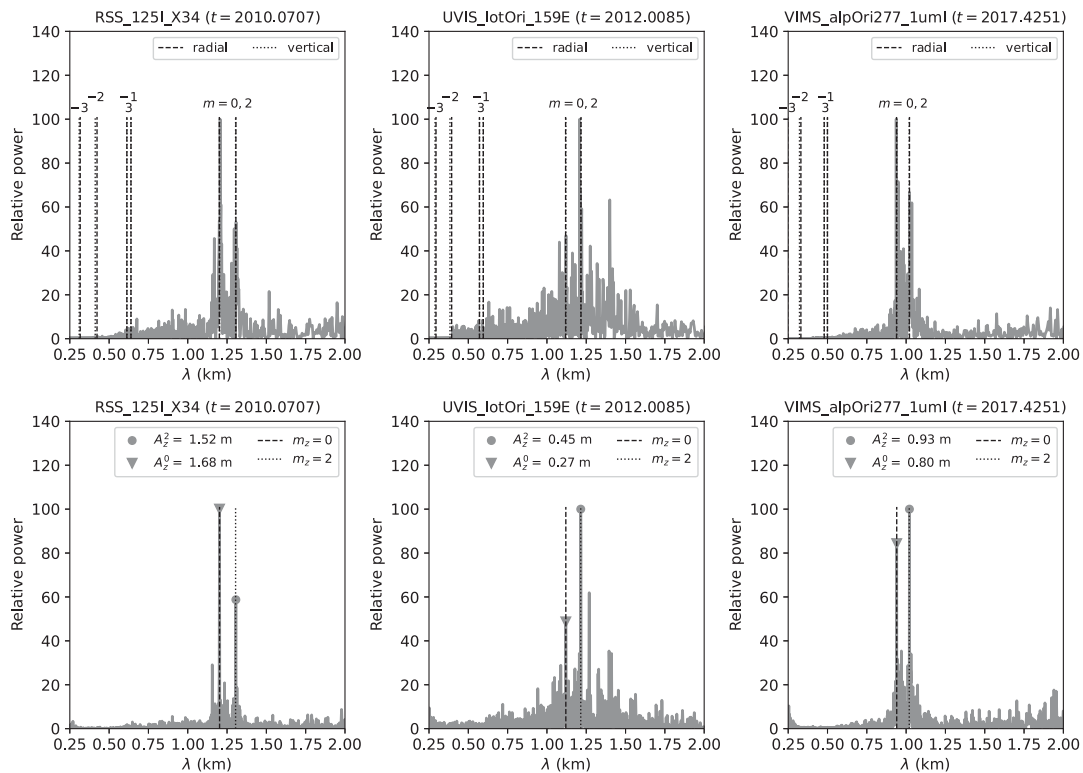


Fig. 12. Power spectra of three low-incidence occultation profiles computed over the radial range 75,100–75,675 km, plotted as a function of radial wavelength λ at a reference radius $r_0 = 75,400$ km. For each event, the predicted wavelengths of the $m = -3, -2, -1, 0, 2$, and 3 modes are shown at top, with radial and vertical locations marked by dashed and dotted lines, respectively. An impact date $t_i = 1983.7$ is assumed for all calculations. The upper row shows relative power in the continuous Fourier transform (CFT) of the observations using the nominal radius scale, and the lower row shows the CFT power using a distance scale that corrects for the predicted dispersion of a spiral wave with $m \neq 1$. For each observation, a broad pedestal of power is visible near the predicted $m = 0$ mode wavelengths in the upper row, with considerably sharper isolated peaks in the scaled radius results in the lower row. The observed wavelengths of maximum power decrease systematically from the earliest shown occultation (RSS_125I_X34, $t = 2010.0707$) at left to the VIMS_alphaOri277_1uml event ($t = 2017.4251$) spectrum at right. The UVIS_IotOri_159E occultation in the middle panel is of a multiple-star system (ι Ori), contributing to the complexity of the observed power spectra. Under the assumption that the two contributing modes are the $m = 0$ and $m = 2$ vertical modes, their amplitudes are estimated by iteratively determining the amplitudes A_z^0 and A_z^2 of a composite model wave that match the observed peak power at the corresponding predicted wavelengths. No statistically significant power is seen for other values of m .

4.3.3. Direct retrieval of vertical structure

Assuming that all of the observed variations in optical depth are due to vertical structure of the ring, rather than to radial variations in the background optical depth, and that the vertical slopes are sufficiently small that every occultation ray penetrates the rings only once, it is possible to retrieve the vertical structure of the ring $z(r)$ directly from the optical depth profile $\tau_z(r)$ (Gresh et al., 1986). Solving iteratively for $dz(r)/dr$ from Eq. (59) and then integrating the result, we have:

$$z(r) = \int_{r_i}^r \frac{dz(r')}{dr'} dr'. \quad (71)$$

To illustrate the technique, Fig. 14 shows the vertical profile derived from a triple wavepacket in the RSS_133I_X15 radial optical depth profile over the radial range 77,705–77,745 km, assuming that the ring has a uniform background optical depth and that all of the observed variations in $\tau_n(r)$ are the result of variations in the slant-path optical depth as each occultation ray penetrates the vertically-corrugated ring only once. The resulting vertical profile $z(r)$ is dominated by a $\lambda \sim 25$ –30 km periodic signature with vertical amplitude $A_z \sim 75$ m, with superimposed smaller-amplitude shorter-wavelength ripples with vertical amplitudes ~ 5 –10 m associated with the prominent ~ 1 -km scale beat pattern in wavepackets. For comparison, the predicted wavelength of an $m_z = 1$ mode for this event at this radial location is $\lambda_z^1 \sim 35$ km, assuming an impact date of 1983.7, as illustrated in the lower right panel of Fig. 1.

We will return in Section 5 to assess the detectability of the $m = 1$ modes in the occultation data, but for now we will concentrate on the more certain $\lambda \sim 1$ km corrugations to estimate the impact date.

4.4. Localized power spectra of region R75.5

To refine the estimates of the best-fitting $m = 0$ and $m = 2$ vertical mode wavelengths and their dependence on orbital radius, we determine the wavenumbers k_z^0 and k_z^2 of the peaks within more localized regions of each optical depth profile, choosing a fixed window halfwidth $w = 200$ km and stepping in boxcar fashion along the radial profile. To illustrate the technique, Fig. 15 shows examples of the resulting power spectra for instances of each of the four time periods during which the $\lambda \sim 1$ km C ring ripples are detectable: an early RSS event in 2008, a later RSS event in 2010, a UVIS occultation in 2012, and a VIMS occultation in 2017. Each panel shows the CFT computed using a scaled radius $d(r)$ for a single boxcar width centered within region R75.5. In every instance, there are two isolated and prominent peaks in power at wavenumbers k_z^0 and k_z^2 closely matching the predicted values (shown by vertical lines) for $m = 0$ and $m = 2$ vertical modes produced by an impact in 1983.7:

- (a) The RSS_060E_X14 event (upper left, $t = 2008.16594$) was observed at a ring opening angle $B^* = -8.642^\circ$ and $\tan B_{\text{eff}} = 0.3410$, and although the data are too noisy to reveal the periodic ripple structure in the optical depth profile itself at the resolution shown, the power spectrum clearly shows the presence of two modes at the predicted locations, both well above the noise level.
- (b) The RSS_125I_X34 occultation (upper right, $t = 2010.07070$) was observed at a smaller ring opening angle $B^* = 4.767^\circ$, providing higher SNR but at less favorable azimuth ϕ for detecting vertical structure, resulting in a marginally smaller $\tan B_{\text{eff}} = 0.2807$

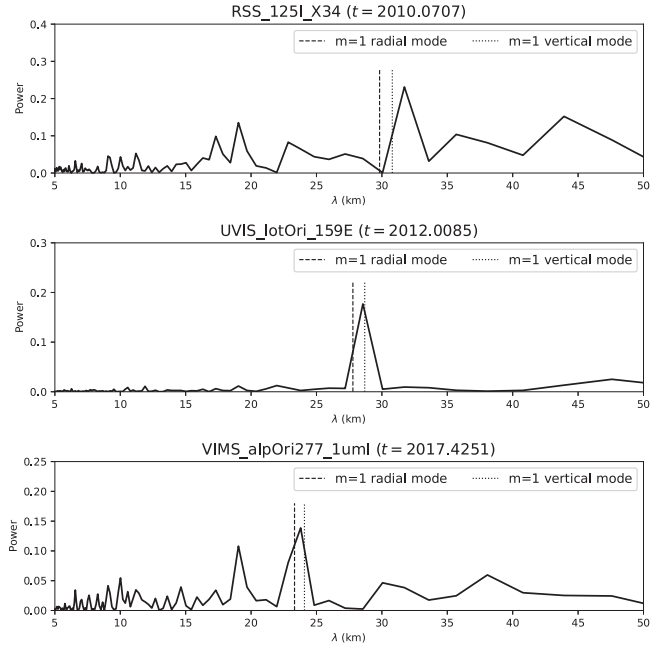


Fig. 13. Conventional Fourier transform power spectra of the same three events and data intervals shown in Fig. 12. For each event, the predicted wavelengths of the $m = 1$ radial and vertical modes assuming an impact date of 1983.7 are marked by dashed and dotted lines, respectively. The wavelength of the observed peak power decreases from about 32 km for RSS_125I in 2010 to about 24 km for VIMS_alpOri277_1umI (2017), consistent with windup of the $m = 1$ mode over the seven-year interval between these two events. On the other hand, compared to the examples in Fig. 12, which showed strong and narrow peaks in power at the expected wavelengths for $m = 0$ and $m = 2$ vertical modes, the peaks in the power spectra in the $\lambda = 22–31$ km range are broader and are thus less securely attributable to $m = 1$ modes.

than for RSS_060E_X14. The spiral patterns have tightened over the 1.90 yr interval between these two events, and the higher SNR is reflected in the prominent power peaks compared to the noise level in the spectrum. The optical depth profile shows both short-scale periodic structure and longer-scale quasiperiodic undulations that may be the signature of the $m = 1$ spiral pattern identified in the *Cassini* ISS images (Hedman et al., 2011).

- (c) The UVIS_IotOri_159E event (lower left, $t = 2012.0085$) was observed at a ring opening angle $B^* = -1.192^\circ$, with $|\tan B_{\text{eff}}| = 0.0407$, the lowest of any of the observations considered in this study. Once again, the wavenumbers of the two modes have increased since the previous observations and match the predicted values for an impact with $t_i = 1983.7$.
- (d) The high-SNR VIMS_alpOri277_1umI occultation (lower right, $t = 2017.42505$) was observed at ring opening angle $B^* = 11.682^\circ$ and $|\tan B_{\text{eff}}| = 0.3540$ (comparable to the RSS_060E_X14 event), with noticeably higher k_z^0 and k_z^2 than the early RSS event shown in panel (a).

These examples provide snapshots of the process whereby we determine the radial variations of $k_z^0(r)$ and $k_z^2(r)$ across a chosen radial region for a given observation. For a given boxcar halfwidth w , we step in radius along the optical depth profile in increments of 5 km, compute the CFT within the corresponding window, and tabulate for each step the power and wavenumbers of the two strongest isolated peaks in the CFT power spectrum within a bounded region of the power spectrum centered on the expected wavenumbers of the two vertical modes. Fig. 16 shows the results for the RSS_060E_X14 event, with halfwidth $w = 200$ km boxcar centers spanning the radial range 75,300–75,675 km. The upper panel shows the normal optical depth profile. A vertical solid line marks the reference radius $r_0 = 75,500$ km at which

we estimate k_z^0 and k_z^2 , using the scaled radius d centered at r_0 . The vertical dashed lines mark the inner and outer boundaries of the central radii sampled by the sliding boxcar window. The orange portion of the profile shows the data used for the boxcar at the center of the selected radial range. The horizontal range of the panel shows the inclusive radial range of the data included in the full set of boxcar steps. The radial trends in the power of the two power spectrum peaks shown in the lower panel are plotted as orange and blue dots in the upper panel of the figure, scaled vertically to fit within the plot window.

The lower panel of Fig. 16 shows the results of the individual determinations of the wavenumbers of the two peaks in the power spectrum for the central radius of each boxcar step, plotted as filled circles (blue for the stronger of the two power peaks and orange for the weaker). They fall along two parallel downward-sloping lines as a function of radius, with decreasing wavenumber and increasing corresponding wavelength $\lambda = 2\pi/k$ labeled on the right vertical axis. The upper set of points matches nearly perfectly the nearly-hidden dot-dashed line marking predicted $k_z^0(r)$ for an $m = 0$ vertical mode with an assumed impact date $t_i = 1983.7$, while the lower set of points similarly match the predicted $k_z^2(r)$ for an $m = 2$ vertical mode, marked by a nearly-hidden dashed line. Both lines are bracketed by a nearby pair of dotted lines separated by $\Delta k/2\pi = \pm 0.01 \text{ km}^{-1}$ of the predicted wavenumber. The best-fitting $k_z^2(r)$ and $k_z^0(r)$ models computed from Eqs. (27) and (37) for measured peaks in the power spectra that lie within the respective pairs of bounding lines are overplotted on the measured points. (Outlier peaks in the power spectrum that fall outside of these bounds are excluded from the fit.) In this instance, the wavenumbers at the reference radius r_0 are $k_z^2(r_0)/2\pi = 0.7076 \text{ km}^{-1}$ and $k_z^0(r_0)/2\pi = 0.7691 \text{ km}^{-1}$, with corresponding wavelengths $\lambda_k^2(r_0)$ and $\lambda_z^0(r_0) = 1.4132 \text{ km}$ and 1.3002 km and inferred impact times $t_i = 1983.7479$ and 1983.6927 , respectively, computed from Eqs. (27) and (37) and ignoring any contribution from the ring's self-gravity. In Section 5 below, we will make use of these measurements to estimate the radial variations in the amplitudes $A_z^2(r)$ and $A_z^0(r)$.

Similarly, Fig. 17 shows the results for the RSS_125I_X34 event, for boxcar halfwidth $w = 200$ km with boxcar centers spanning the radial range 75,300–75,675 km. In this instance, the wavenumbers at the reference radius r_0 are $k_z^2(r_0)/2\pi = 0.7631 \text{ km}^{-1}$ and $k_z^0(r_0)/2\pi = 0.8291 \text{ km}^{-1}$, with corresponding wavelengths $\lambda_k^2(r_0)$ and $\lambda_z^0(r_0) = 1.3105 \text{ km}$ and 1.2061 km and inferred impact times $t_i = 1983.7390$ and 1983.6882 , respectively, ignoring any contribution from the ring's self-gravity.

Fig. 18 shows the results of a similar analysis of the UVIS_IotOri_159E event, for boxcar halfwidth $w = 125$ km, chosen because it resulted in a more complete set of mode detections than $w = 200$ km. Note that there are instances in which the wavenumbers of one or both of the strongest pair of peaks on the power spectrum fall outside of the expected vicinity of the $m = 0$ and $m = 2$ vertical modes. For example, between 75,600 and 75,660 km neither of the two power spectrum peaks falls near the predicted range for the vertical mode, and there is instead a set of points with $\lambda \approx 1.28 \text{ km}$ at the lower right that follow the same slope as the model $k_z^2(r)$ and $k_z^0(r)$ trends. We attribute these signals to the co-addition of radially offset wavepackets associated with weaker components of the multiple star system. The estimated impact dates are $t_i = 1983.6739$ and 1983.7143 from the fits to the two sets of observations lying within the bounded ranges of expected wavenumbers for the $m_z = 2$ and $m_z = 0$ modes, respectively.

Fig. 19 shows the results for the VIMS_alpOri277_1umI event, one of the highest SNR occultations in our set. In this instance, both modes are prominent, clearly separated, and yield estimated impact times $t_i = 1983.7601$ and 1983.6813 for the $m_z = 2$ and $m_z = 0$ modes, respectively.

We performed a similar analysis for region R75.5 for each observation listed in Table 1, using a range of window halfwidths w

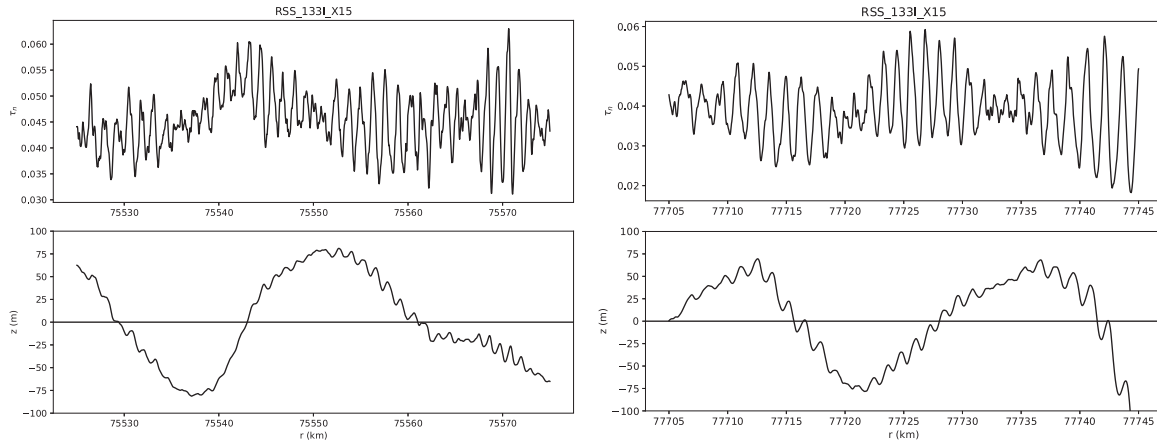


Fig. 14. Ring vertical structure obtained by direct retrieval from the RSS_133L_X15 radial optical depth profile over the radial ranges 75,525–75,575 km (top left) and 77,705–77,745 km (top right), under the assumption that the background optical depth is uniform and that the observed optical depth variations result from the varying slant path optical depth as the occultation probes the vertically corrugated surface of the ring. The lower panels show the resulting vertical profile $z(r)$, featuring a $\lambda \sim 25 - 30$ km periodic signature with vertical amplitude $A_z \sim 75$ m, with superimposed smaller vertical amplitude ($\sim 5-10$ m) shorter-wavelength ripples associated with the ~ 1 -km scale variations in the optical depth profile. (Note that the vertical amplitudes of the 1-km wavelength ripples are somewhat smaller for the R75.5 wavepacket at left than for the R77.7 wavepacket at right.).

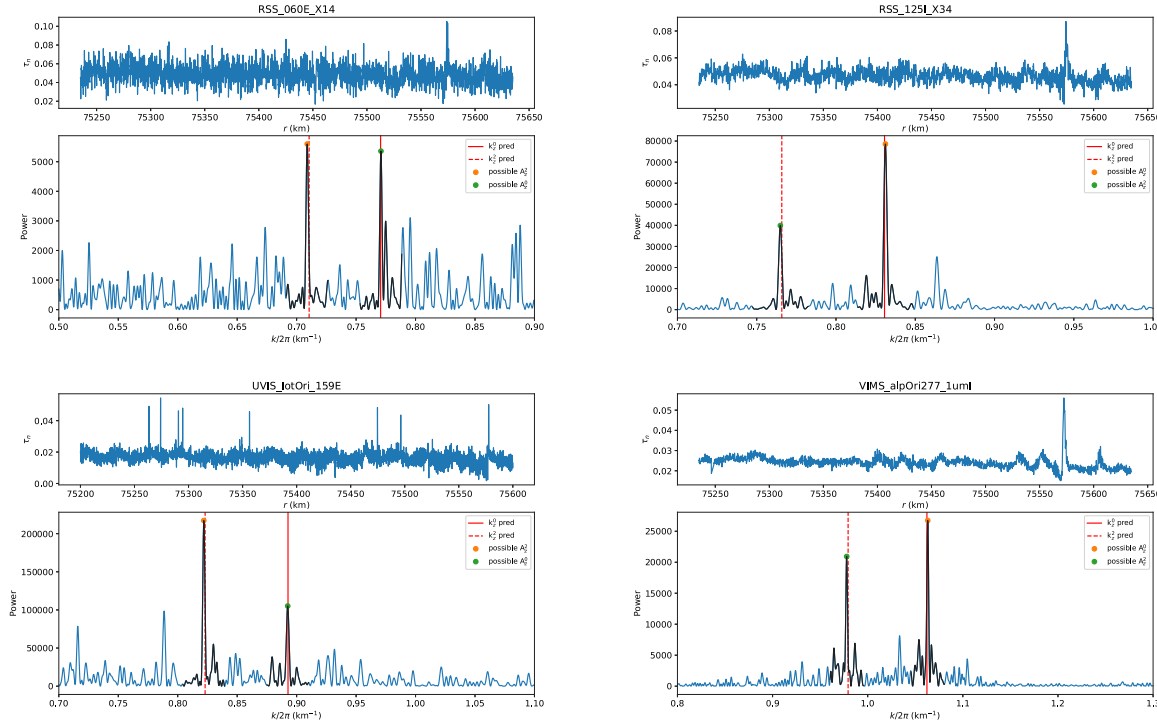


Fig. 15. Continuous Fourier transform (CFT) power spectra representing the four separate time intervals of observations that revealed evidence of C ring ripples, computed using a scaled radius scale $d(r)$ for the radial ranges shown, all within region R75.5. Upper left: RSS_060E_X14 ($t = 2008.16594$). Upper right: RSS_125I_X34 ($t = 2010.07070$). Lower left: UVIS_IotOri_159E ($t = 2012.00852$). Lower right: VIMS_alpOri277_1uml ($t = 2017.42505$). See text for details.

from 100 to 200 km in steps of 25 km. (We omit the R77.7 region here because of the effects of the Titan 1:0 resonance on k_r .) Many, but not all, events showed convincing evidence for periodic structure with the expected wavelengths of $m = 0$ and $m = 2$ vertical modes. For each occultation, we retained the result for a given mode for the widest window halfwidth w that yielded the largest number $N \geq 20$ of measured points with wavenumbers falling within the $\Delta k/2\pi = \pm 0.01 \text{ km}^{-1}$ band of the predicted values, assuming an impact date $t_i = 1983.7$. The results are given in Table 6. For each retained event and detected mode, we include the number of power spectrum

measurements N lying within the expected wavenumber band, the window halfwidth w , the fitted wavenumber $k/2\pi$ and corresponding wavelength λ , the observed time t , and the inferred impact date t_i . These results ignore ring surface gravity, which introduces systematic fractional correction terms in the wavenumber ~ 0.001 and consequent changes in the inferred impact date of up to 0.03 yr for the 2017 observations. Note that these corrections are of opposite sign for radial and vertical modes of a given m , as shown in Appendix A, Eqs. (A.12) and (A.14) for $m \neq 1$ or 0, and Eqs. (A.24) and (A.28) for $m = 0$. We explore these effects in Section 4.6 below.

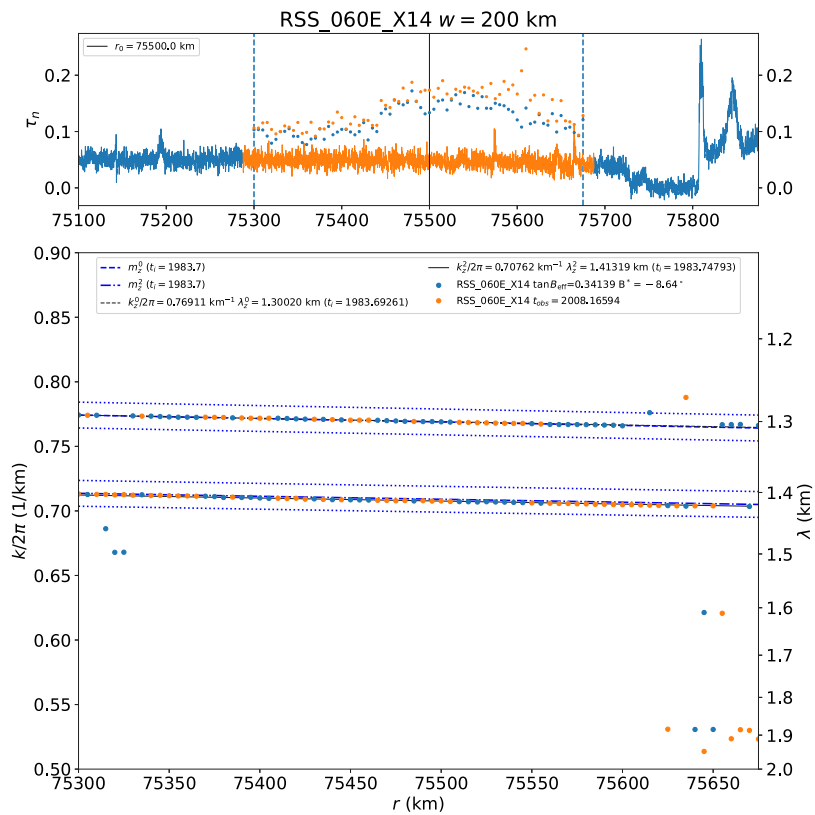


Fig. 16. Results of power spectral analysis of the RSS_060E_X14 occultation. The upper panel shows the radial optical depth profile over which the power spectrum was computed, using a boxcar halfwidth $w = 200$ km in steps of 5 km. The radial trends in the power of the two power spectrum peaks in the lower panel are shown by the orange and blue dots, scaled vertically to fit within the plot window. The lower panel shows the wavenumbers $k/2\pi$ of the two strongest peaks in the power spectrum for the central radius of each boxcar step (orange dots for the stronger and blue dots for the weaker of the two peaks). The corresponding radial wavelengths are indicated by the right axis labels. The measured points follow a sloping line, indicating that the periodic structure responsible for the power peaks increases in wavelength with increasing radius. The observed slope and wavenumbers closely match the predictions for $m = 0$ vertical (upper line of points) and $m = 2$ vertical (lower line) modes, shown as dot-dashed lines underneath the data points, assuming an impact date $t_i = 1983.7$. Lines overplotted on the measured points show the best-fitting $k_z^2(r)$ and $k_z^0(r)$ models computed from Eqs. (27) and (37) for measured peaks in the power spectra that lie within the respective pairs of bounding lines separated by $\Delta k/2\pi = \pm 0.01$ km $^{-1}$ of the predicted wavenumber. (Outlier peaks in the power spectrum that fall outside of these bounds are excluded from the fit.) See text for additional details. (For interpretation of the references to color in this figure legend, the reader is referred to the web version of this article.)

4.5. Estimated impact date

We are now in a position to use the full set of observations to determine the date of the impact that produced the observed short-wavelength ripple structure in the C ring. Independent of the detailed dynamics that govern the radial dependence of the windup rate of the observed spiral structure, the time dependence of the wavenumber at a given radial location can be linearly extrapolated back in time to the instant at which $k = 0$, under the assumption that $k(t - t_i) \propto (t - t_i)$. (This proportionality follows from Eqs. (36) and (37), and ignores the possible role of the self-gravity of the ring in affecting the windup rate.) In Fig. 20, we plot the observed $k_z^2(r_0, t)$ and $k_z^0(r_0, t)$ from Table 6 as a function of observation time t , for $r_0 = 75,500$ km. The black solid and dashed lines show the best fits to the individual RSS, UVIS, and VIMS wavenumber values from Table 6, plotted as color-coded dots. The fitted straight lines, extrapolated to $k = 0$, yield the inferred impact dates $t_i = 1983.747 \pm 0.016$ and 1983.691 ± 0.020 for the k_z^2 and k_z^0 modes, respectively. This corresponds to Fit 1 in Table 7.

These results establish that the component modes of the $\lambda \sim 1$ km C ring ripples are some combination of $m = 0$ and $m = 2$ radial and vertical modes. Fig. 20 includes the predicted time evolution of radial and vertical modes for other possible azimuthal wavenumbers $m = -2, -1, 1, 3$ and 4, all of which are far removed from the observations. In contrast, the predictions for the $m = 0$ and $m = 2$ modes shown as gray bands fall almost exactly along the fitted lines based solely on the observed time dependence of the wavenumber measurements, with the

fitted impact date from the k_z^2 observations being 0.057 yr (i.e., ~ 21 days) after the k_z^0 result. (We will investigate this apparent time offset in more detail below.)

A second approach to estimating the impact date is to use the dynamically-based results of the power spectrum analysis that yield the observed $k_z^0(r_0, t)$ and $k_z^2(r_0, t)$ for each event and observed time t . A separate estimate of the impact time t_i from the two vertical modes for a given event follows directly from Eq. (37), based on the dispersion relation for bending waves. The top panel of Fig. 21 shows the results of this analysis, listed as Fit 2 in Table 7. The individually estimated impact times are plotted on the vertical axis, with the corresponding observation date t on the horizontal axis. The results are color-coded by Cassini instrument (blue for RSS, orange for UVIS, and green for VIMS), with filled and open symbols corresponding to impact dates derived from $k_z^0(r_0, t)$ and $k_z^2(r_0, t)$, respectively. The average of all values ($t_i = 1983.717 \pm 0.029$) is shown as a horizontal blue line. The results for the two modes differ systematically: the mean value of the impact times derived from the k_z^2 measurements ($t_i = 1983.743 \pm 0.015$) is significantly later than that for the k_z^0 measurements ($t_i = 1983.691 \pm 0.011$), with measurable trends in time for both modes, shown as the fitted sloping dotted and dashed lines. The average slope of the combined set of measurements is shown as a solid black line, and is almost zero, but the systematic trends in the derived impact dates over the observation period 2008 to 2017 suggest that the assumption that $k(t) \propto (t - t_i)$ is oversimplified. This ignores the self-gravity of the ring, which introduces small time-dependent terms of opposite signs into the

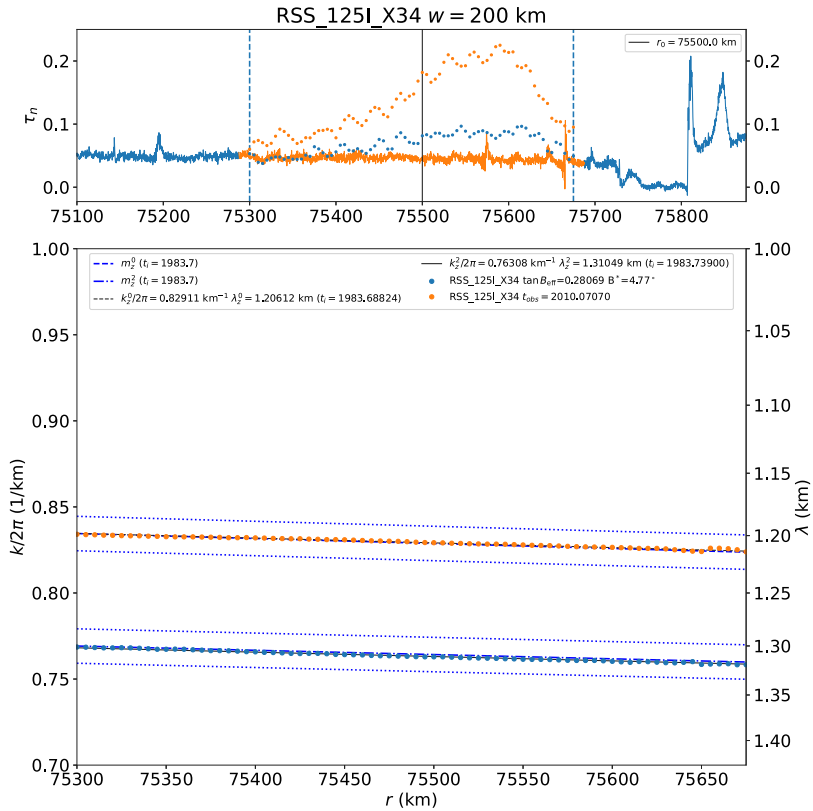


Fig. 17. Results of power spectral analysis of the RSS_125I_X34 occultation. See caption for Fig. 16 and text for additional details.

expressions for $k_z^2(r)$ and $k_z^0(r)$ given in Eqs. (49) and (51). Hedman et al. (2011) showed that perturbations in the $m = 1$ vertical corrugation wavenumber were correlated with local gradients in the surface mass density of the middle C ring, and we now explore the possibility that ring self-gravity can similarly account for the systematic trends in the top panel of Fig. 21.

We define a self-gravity parameter

$$\epsilon(r_0) = \frac{\pi G}{2n} \left[\frac{\sigma(r_0)}{r_0} - \frac{\partial \sigma(r_0)}{\partial r} \right] \quad (72)$$

(with units of yr^{-1}) to represent the magnitude of the fractional change in k_z^2 or k_z^0 resulting from ring self-gravity, evaluated at a reference radius r_0 . (For the moment, we postpone the consideration of the relative contributions of the two surface mass density terms σ/r_0 and $\partial\sigma/\partial r$ to the sum.) We generalized the power spectrum method illustrated in Figs. 17–19 to solve for the impact date t_i as a function of ϵ , according to

$$k_z^0 = k_{z0}^0(1 + \epsilon \Delta t) \quad (73)$$

and

$$k_z^2 = k_{z0}^2(1 - \epsilon \Delta t), \quad (74)$$

where $\Delta t = t - t_i$.

We repeated the full power spectrum analysis for all data sets for a range of ϵ from 0 to $7 \times 10^{-5} \text{ yr}^{-1}$. The results are shown in Fig. 22. In the top panel, we plot the standard deviation σ of the residuals of linear fits to k_z^0 and k_z^2 , both separately and when combined (k_z^0, k_z^2). The dispersion in the combined measurements reaches a minimum near $\epsilon = 3.25 \times 10^{-5} \text{ yr}^{-1}$, while the standard deviations for the fits for the separate modes are only weakly dependent on ϵ . We assign an estimated uncertainty $\sigma(\epsilon) = 1 \times 10^{-5} \text{ yr}^{-1}$. The middle panel of the figure shows the derived impact times from the three separate linear fits, as a function of ϵ . Note that for $\epsilon = 3.25 \times 10^{-5} \text{ yr}^{-1}$, all three fits

give nearly the same impact times, as shown in Table 7 for Fit 3 and the lower panel of Fig. 21. Finally, in the bottom panel of Fig. 22, we plot the slopes of the linear fits to the separate and combined observations of the two modes. Once again, for the favored value of $\epsilon = 3.25 \times 10^{-5} \text{ yr}^{-1}$, the slopes of all three fits are nearly zero.

As an independent test of the validity of our assignment of the k_z^0 and k_z^2 modes as responsible for the C ring ripple structure, we tested the alternative possibilities enumerated as Cases A, B, and D in Section 4.2.2 by performing a suite of power spectral analyses for a range of self-gravity parameters ϵ for each case. Compared to the summary results in Fig. 22, none of the three alternative mode assignments resulted in a unique value of ϵ that simultaneously minimized the RMS of the joint estimate for the impact date, yielded the same impact dates for the two modes, and minimized the slopes of $k(t)$ to nearly zero. Only the k_z^0, k_z^2 mode combination achieved this, lending support to the proposal that the effects of ring self-gravity are detectable in the occultation data.

To explore the influence of ring self-gravity on the empirical fits to $k_z^0(t)$ and $k_z^2(t)$ (Fit 1), we performed quadratic fits with the same functional form as Eqs. (73) and (74):

$$k_z^0(\Delta t) = k_z^{0'} \Delta t(1 + \epsilon \Delta t) \quad (75)$$

and

$$k_z^2(\Delta t) = k_z^{2'} \Delta t(1 - \epsilon \Delta t), \quad (76)$$

constraining ϵ to be the value from our adopted dynamical solution but removing the requirement that the leading factors $k_z^{0'}(t)$ and $k_z^{2'}(t)$ correspond to the unperturbed values computed from the planet's gravity field using Eqs. (27) and (37). The results (Fit 4) yield fitted impact dates for the two modes that are in excellent mutual agreement: $t_i = 1983.719 \pm 0.020$ and 1983.719 ± 0.016 for k_z^0 and k_z^2 , respectively, and very close to our adopted joint solution of $t_i = 1983.715 \pm 0.015$ (Fit 3).

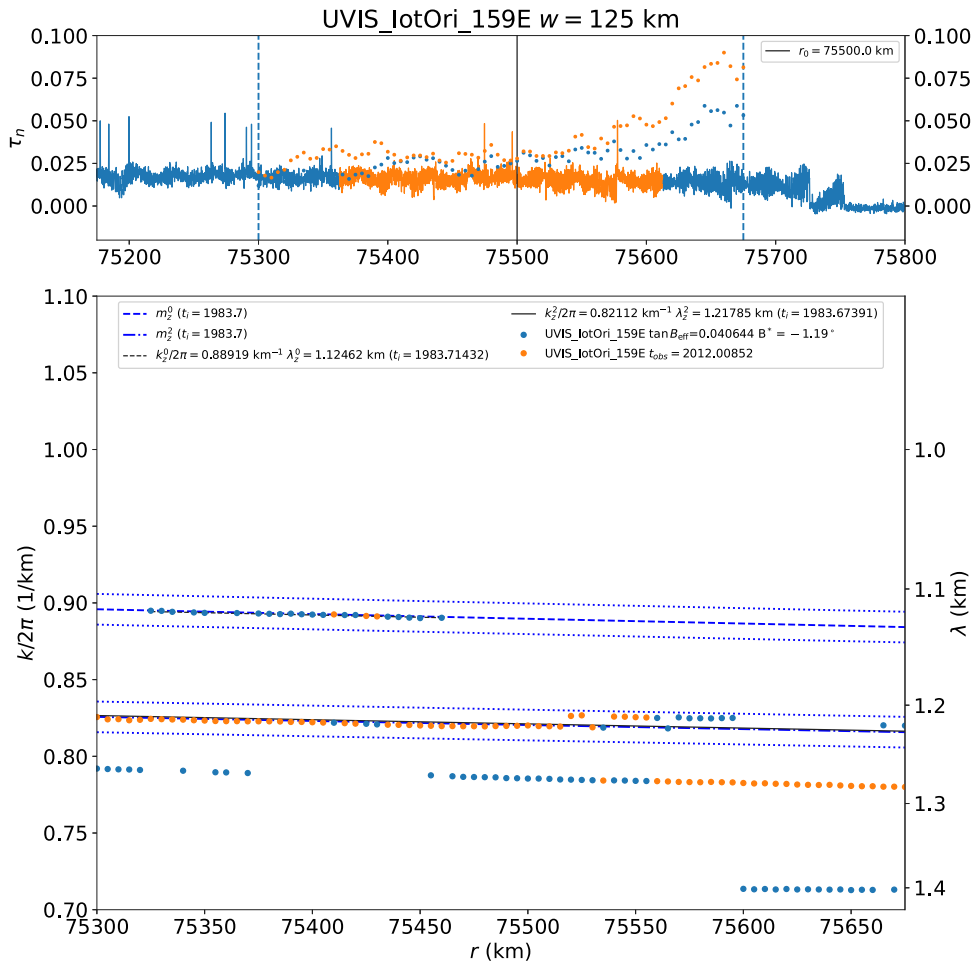


Fig. 18. Results of power spectral analysis of the UVIS_IotOri_159E occultation. The upper panel shows the radial optical depth profile over which the power spectrum was computed, using a boxcar halfwidth $w = 125$ km in steps of 5 km. Several clusters of measured points intermittently fall in the vicinity of the predict wavenumbers for $m = 0$ vertical (upper line of points) and $m = 2$ vertical (lower line) modes, assuming an impact date $t_i = 1983.7$. See caption for Fig. 16 and text for additional details.

Fig. 23 summarizes the results of the suite of fits given in Table 7. The Fit 1 impact dates result from empirical linear fits to the ensemble of measurements of k_z^0 and k_z^2 as a function of time under the assumption that the corrugation windup rates are constant in time. Fit 2 gives the averages of the impact dates obtained from power spectrum analysis of individual occultation events, using a dynamical model for the windup rate of the vertical corrugations. Both Fits 1 and 2 ignore the possible effects of ring surface density, and show systematic differences between the inferred impact dates derived separately from the two modes. Fit 3 (our adopted solution) includes the predicted effects of ring self-gravity, with a best-fitting value of the ring self-gravity parameter $\epsilon = (3.25 \pm 1.0) \times 10^{-5} \text{ yr}^{-1}$. The systematic differences seen in Fits 1 and 2 between the impact times derived from the two modes have been virtually eliminated, with a best-fitted mean impact date $t_i = 1983.715 \pm 0.015$ (UTC 1983 Sep 19.25 ± 5.5 d). Fits 3 and 4 are in excellent agreement with the impact date $t_i = 1983.717 \pm 0.11$ (Fit 5, UTC 1983 Sep 20 ± 40 d) estimated by Hedman et al. (2011) from an analysis of $m = 1$ vertical corrugations, suggesting that the vertical structure evident in the short-wavelength $m = 0$ and $m = 2$ corrugations was produced within a few days at most of the $m = 1$ structure.

4.6. Effects of ring self-gravity

Our adopted value for the impact time is based on the fit shown in the lower panel of Fig. 21 that included ring self-gravity, chosen to minimize the differences and systematic trends in the massless ring fit shown in the upper panel. Here, we explore whether these results are

consistent with the optical depth, surface density, and opacity of the inner C ring. The two terms in ϵ related to surface density are σ/a and $\partial\sigma/\partial a$. The first of these is quite small: assuming that the mean surface density near R75.5 is $\bar{\sigma} = 1.5 \text{ g cm}^{-3}$, from an analysis of density and bending waves (Afigbo et al., 2025),⁶ and assuming $\partial\sigma/\partial a = 0$, we find $\epsilon = 0.2 \times 10^{-5} \text{ yr}^{-1}$, much smaller than the fitted value of $\epsilon = 3.25 \times 10^{-5} \text{ yr}^{-1}$ for our adopted solution (Fit 3) in Table 7. The more significant gradient term in the definition of ϵ can be expressed in terms of the corresponding fractional change in surface density over a given radial range Δa : $\frac{1}{\bar{\sigma}} \frac{\partial\sigma}{\partial a} \Delta a$.

We now combine the inferred fractional decrease in surface density from the analysis of the $m = 0$ vertical and radial modes and the measured slope in the normal optical depth to estimate the corresponding variation in ring opacity K in this region.⁷ A trustworthy comparison requires observations of exceptional photometric stability and SNR, ideally with large $|\tan B_{\text{eff}}|$ to minimize the visibility of the $m = 0$ waves and the $m = 1$ corrugations. Two such occultations are the VIMS_omiCet135I (Nicholson et al., 2020) and the UVIS_KapOri212I observations, shown in Fig. 24 at ~ 2 km and 1 km resolution, respectively. The two data sets have very similar mean optical depth and detailed radial structure, confirming that the observed variations are intrinsic features of the ring and not artifacts of photometric variability

⁶ By comparison, Baillié et al. (2011) obtained $\bar{\sigma} = 0.58 \pm 0.09 \text{ g cm}^{-3}$ from an analysis of the Mimas 4:1 density wave at 74,890 km.

⁷ We denote opacity as $K = \tau/\sigma$ instead of the more usual κ to avoid possible confusion with the epicyclic frequency.

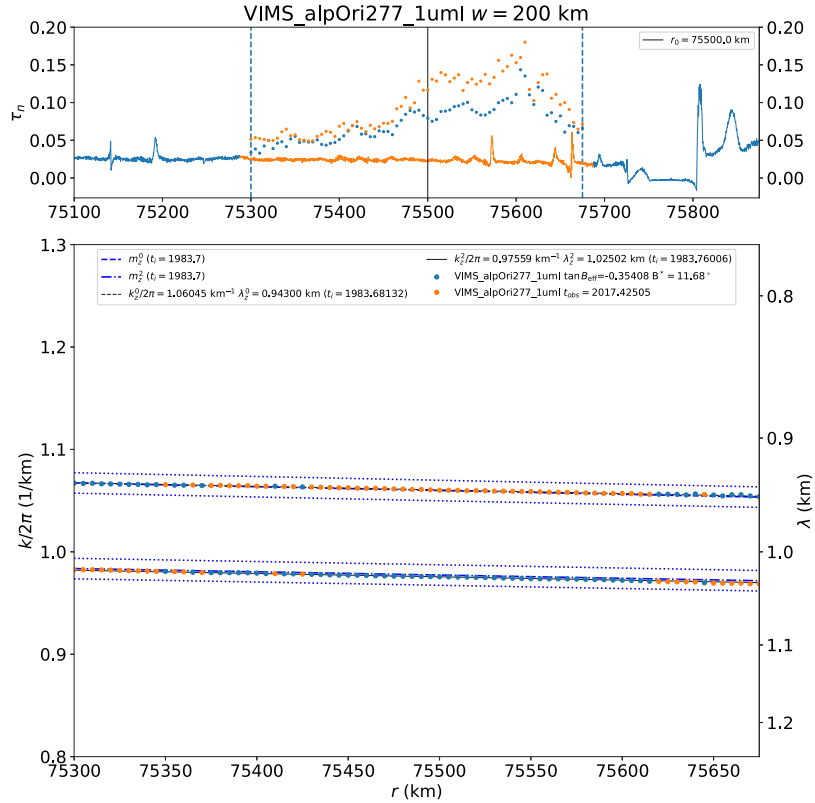


Fig. 19. Results of power spectral analysis of the VIMS_alpOri277_1uml occultation. See caption for Fig. 16 and text for additional details.

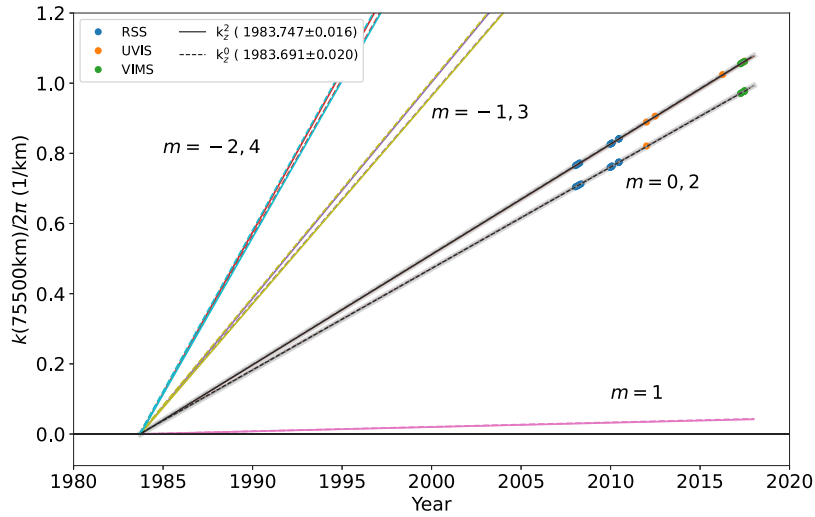


Fig. 20. Linear fits to the measured values of $k_z^2(t)$ and $k_r^m(t)$ at a reference radius $r_0 = 75,500$ km, determined from spectral analysis of region R75.5 for all events listed in Table 6. The observations fall in four groups: early and late RSS events (blue), UVIS events in 2012 (orange), and post-2016 UVIS and VIMS events (orange and green). The solid and dashed lines show $k_z^m(t)$ and $k_r^m(t)$ for azimuthal wavenumbers $m = -2$ through 4, computed from Eqs. (26) and (27) for an assumed impact time $t_i = 1983.7$. The observed points fall almost exactly on the predicted lines for $m = 0$ and $m = 2$, shown as the underlying gray bands for clarity. These results confirm the identification of the observed C ring ripples as some combination of $m = 0$ and/or $m = 2$ radial and vertical modes. Note the near-commensurability of $k_r^m \sim k_z^{m+2}$ (or, equivalently, $k_z^m \sim k_r^{2-m}$), for $m \neq 1$ (see Appendix B), resulting in an ambiguity in the mode identification in the absence of additional information. (For interpretation of the references to color in this figure legend, the reader is referred to the web version of this article.)

in the observations. Over the radial range shown $\Delta r = 370$ km, the fractional change in the VIMS optical depth is $(\partial \tau_n / \partial r) / \bar{\tau}_n \times 370$ km = −0.100, shown by the linear fit plotted in orange. The mean optical depth is shown as a black line, and the derived fractional change in surface mass density across the region for Fit 3 [$(\partial \sigma / \partial r) / \bar{\sigma} \times 370$ km] is −0.068 (green), respectively, scaled in the figure to match the mean optical depth at $r_0 = 75,500$ km. Combining these results, we can

estimate the corresponding fractional change in ring opacity $K = \tau_n / \sigma$ over the range Δr :

$$\frac{1}{K} \frac{\partial K}{\partial r} \Delta r = \frac{1}{\bar{\tau}_n} \frac{\partial \tau_n}{\partial r} \Delta r - \frac{1}{\bar{\sigma}} \frac{\partial \sigma}{\partial r} \Delta r, \quad (77)$$

where $\bar{K} = \bar{\tau}_n / \bar{\sigma} = 0.025 / 1.5 \text{ cm}^2 \text{ g}^{-1} = 0.017 \text{ cm}^2 \text{ g}^{-1}$, very similar to estimates near this radial range from density waves associated with

Table 6
Results of spectral analysis for region R75.5.

Event	N_z^2	w_z^2 (km)	$k_z^2/2\pi$ (1/km)	λ_z^2 (km)	N_z^0	w_z^0 (km)	$k_z^0/2\pi$ (1/km)	λ_z^0 (km)	t_f (yr)	t_i (yr)		
RSS_056E_X34	72	200	0.70444	1.41956		52	125	0.76513	1.30698	2008.03931	1983.73086	
RSS_057E_X43	68	200	0.70514	1.41815		76	200	0.76593	1.30561	2008.07195	1983.73931	
RSS_060E_X26	38	200	0.70770	1.41303		59	125	0.76866	1.30097	2008.16594	1983.74520	
RSS_060E_X14	71	200	0.70762	1.41319		63	125	0.76925	1.29996	2008.16594	1983.74793	
RSS_063E_X63	74	200	0.70990	1.40865		59	200	0.77229	1.29485	2008.24975	1983.75299	
RSS_064E_X43	22	200	0.71115	1.40617		73	200	0.77233	1.29478	2008.27598	1983.73608	
RSS_067E_X14	76	200	0.71306	1.40240						2008.35447	1983.74862	
RSS_123I_X34	66	200	0.76004	1.31572		76	125	0.82653	1.20987	2009.98326	1983.75638	
RSS_123I_X43	53	200	0.76022	1.31541		76	125	0.82629	1.21022	2009.98326	1983.75016	
RSS_123I_K34	63	200	0.76028	1.31531		76	125	0.82630	1.21021	2009.98326	1983.74819	
RSS_125I_X43	76	125	0.76283	1.31090		76	200	0.82892	1.20639	2010.07070	1983.74738	
RSS_125I_K34	76	200	0.76295	1.31071		76	125	0.82920	1.20598	2010.07070	1983.74339	
RSS_125I_X34	76	200	0.76307	1.31049		76	200	0.82911	1.20612	2010.07070	1983.73900	
RSS_125E_X63	68	200	0.76310	1.31045		76	200	0.82852	1.20697	2010.07116	1983.73873	
RSS_125E_X55	61	200	0.76314	1.31037		76	200	0.82851	1.20699	2010.07116	1983.73720	
RSS_125E_K55	75	200	0.76372	1.30937						2010.07116	1983.71706	
RSS_133I_X15	57	200	0.77433	1.29143		68	200	0.82908	1.20616	2010.07116	1983.68972	
RSS_133E_X34	65	200	0.77473	1.29077						2010.46258	1983.74238	
RSS_133E_X43	64	200	0.77446	1.29122		76	200	0.84135	1.18856	2010.46304	1983.69091	
RSS_133E_X25	69	200	0.77459	1.29100		76	125	0.84116	1.18883	2010.46304	1983.69700	
RSS_133E_X15	73	200	0.77457	1.29104		76	125	0.84134	1.18858	2010.46304	1983.73386	
RSS_133E_K34	74	200	0.77463	1.29094		76	125	0.84149	1.18837	2010.46304	1983.68651	
RSS_133E_K25	65	200	0.77465	1.29090		76	125	0.84132	1.18860	2010.46304	1983.73174	
UVIS_IotOri_159E	62	125	0.82112	1.21785						2012.00852	1983.69183	
UVIS_AlPMa168I					23	125	0.88919	1.12462		2012.00852	1983.71432	
UVIS_GamOri234I					48	200	0.90604	1.10371		2012.49137	1983.66102	
VIMS_alpOri268_1umE	74	200	0.97055	1.03035		22	200	1.02453	0.97606		2016.25529	1983.65455
VIMS_alpOri269_1umE	67	200	0.97171	1.02912						2017.26341	1983.77238	
UVIS_AlPMa274E					75	200	1.05557	0.94736		2017.28305	1983.69458	
VIMS_alpCMa274_1umE	72	200	0.97420	1.02648		60	200	1.05840	0.94482		2017.36440	1983.68574
VIMS_alpOri277_1uml	76	200	0.97559	1.02502		74	200	1.05907	0.94422		2017.36440	1983.74727
VIMS_alpCMa281_1uml	76	200	0.97902	1.02143						2017.42505	1983.66437	
VIMS_alpCMa281_1umE	74	200	0.97677	1.02378		76	200	1.06045	0.94300		2017.48772	1983.70431
UVIS_AlPMa281E	68	200	0.97762	1.02289						2017.48792	1983.78206	
					74	200	1.06207	0.94156		2017.48792	1983.69247	
										2017.48792	1983.75288	
										2017.48792	1983.66939	

Table 7
Summary of fits for date of impact t_i .

Fit #	$t_i(k_z^0)$ (yr)	$t_i(k_z^2)$ (yr)	$t_i(k_z^0, k_z^2)$ (yr)	ϵ (10^{-5} yr $^{-1}$)	Description
1	1983.691 ± 0.020	1983.747 ± 0.016		0.0	Linear fits to $k_z^0(t)$ and $k_z^2(t)$ (Fig. 20)
2	1983.691 ± 0.011	1983.743 ± 0.015	1983.717 ± 0.029	0.00	Dynamical fits (Fig. 21 top)
3	1983.715 ± 0.019	1983.714 ± 0.009	1983.715 ± 0.015^a	3.25 ± 1.00	Dynamical fits (Fig. 21 bottom) - adopted solution
4	1983.719 ± 0.020	1983.719 ± 0.016		[3.25]	Quadratic fits to $k_z^0(t)$ and $k_z^2(t)$ with ϵ from Fit 3
5	1983.717 ± 0.110^b				Hedman et al. (2011) $m = 1$ vertical corrugations

^a UTC 1983 Sep 19.25 \pm 5.5 d.

^b UTC 1983 Sep 20 \pm 40 d.

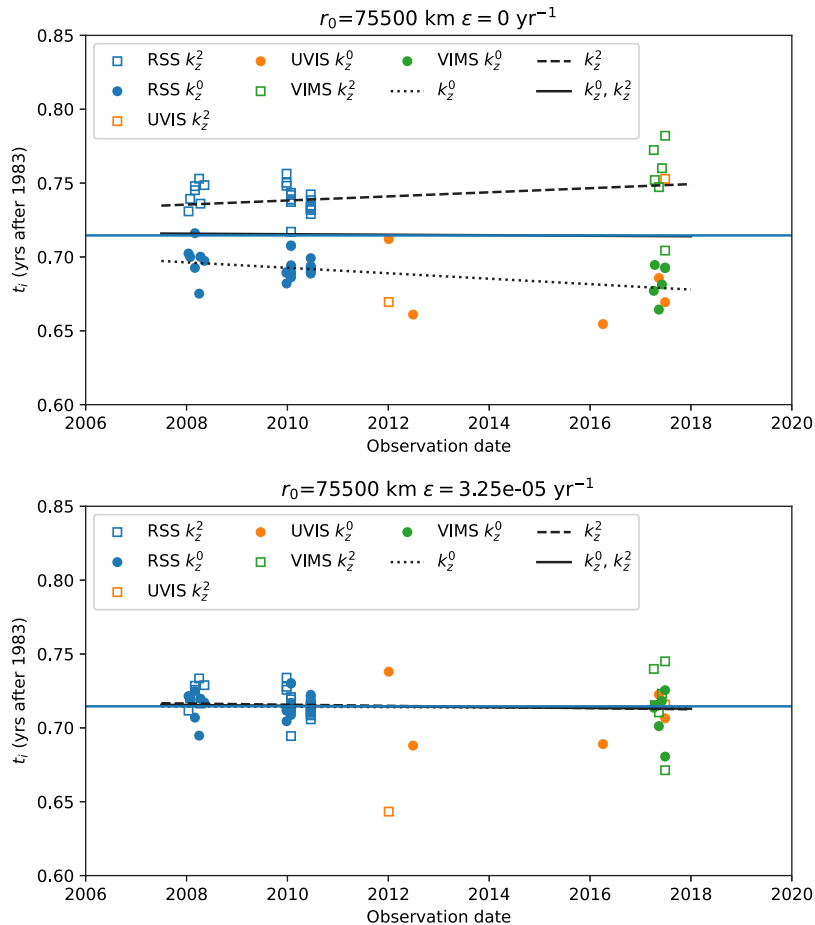


Fig. 21. Estimated impact dates t_i from two regional power spectrum analyses of the RSS, UVIS, and VIMS observations of region R75.5. Top: The inferred impact dates derived separately from each observation, assuming that $k(t) \propto (t - t_i)$ and ignoring any effects of ring self-gravity (i.e., $\epsilon = 0$). Open symbols show the results from the k_z^2 measurements and filled symbols show the values for the k_z^0 measurements. There are clear systematic differences between the two modes, with the $m = 2$ vertical mode giving later impact dates than the $m = 0$ vertical mode. The sloping lines show linear fits over time to the inferred impact dates. Bottom: The corresponding results for an analysis in which the self-gravity of the ring was included, where the adopted value of $\epsilon = 3.25 \times 10^{-5} \text{ yr}^{-1}$ was chosen to minimize the systematic residual trends seen in the top panel, under the assumption that the two modes originated at the same time t_i . Note that the slopes of the fits to k_z^0 and k_z^2 are nearly zero. (For interpretation of the references to color in this figure legend, the reader is referred to the web version of this article.)

planetary resonances (Baillié et al., 2011; Afigbo et al., 2025). Numerically, $[(\partial K / \partial r)/K \times 370 \text{ km}] = -0.032 \pm 0.021$ for Fit 3, taking account of the uncertainty in ϵ . These results are summarized in Table 8.

The inferred few percent decrease in ring opacity with radius across R75.5 is only marginally statistically significant. If real, it might reflect a modest increase in the average ring particle size over this range. Colwell et al. (2018) found no systematic trends in the effective particle size a_{eff} at this location from UVIS photon statistics, whereas (Jerousek et al., 2020) found a slight increase in the maximum particle size a_{max} , although this parameter is only weakly constrained by the differential opacity measurements from Cassini VIMS, UVIS, and RSS occultations. Given the uncertainties, the best we can say is that the proposed opacity gradient is not ruled out by this pair of studies. Probably the most important conclusion is that the modest ring surface density gradient required to offset the systematic errors in the gravity-free analysis of the C ring ripples is physically plausible and does not require substantial variations in ring particle properties in this region of generally uniform optical depth.

4.7. Revisiting the early impact hypothesis

The Voyager RSS Saturn ring occultation observations of 1980 Nov 13 provide a critical test of the original suggestion by Marouf et al.

Table 8
Ring opacity estimates for R75.5^a.

Quantity	Value	Note
\bar{r}_n	0.025	VIMS_omiCet135I
$\bar{\sigma}$	1.5 g cm^{-2}	(Afigbo et al., 2025)
\bar{K}	$0.017 \text{ cm}^2 \text{ g}^{-1}$	$\bar{r}_n/\bar{\sigma}$
Δr	370 km	R75.5
$\frac{1}{\bar{r}_n} \frac{\partial \bar{r}_n}{\partial r} \Delta r$	-0.100	Fit to VIMS_omiCet135I
$\frac{1}{\bar{\sigma}} \frac{\partial \bar{\sigma}}{\partial r} \Delta r$	-0.068 ± 0.021	Fit 3 ($\epsilon = (3.25 \pm 1.00) \times 10^{-5} \text{ yr}^{-1}$)
$\frac{1}{\bar{K}} \frac{\partial \bar{K}}{\partial r} \Delta r$	-0.032 ± 0.021	Fit 3 ($\epsilon = (3.25 \pm 1.00) \times 10^{-5} \text{ yr}^{-1}$)
$\frac{\partial \sigma}{\partial r}$	-0.276 ± 0.085	$\text{g cm}^{-2} (1000 \text{ km})^{-1}$
$\frac{\partial K}{\partial r}$	-0.00020 ± 0.00012	$\text{cm}^2 \text{ g}^{-1} (1000 \text{ km})^{-1}$

^a Radial range 75,300–75,670 km, $\Delta r = 370$ km.

(2011) that the C ring ripples were produced by two impacts several centuries ago. If this were the case, then there would have been relatively little change in the wavelengths of the ripples over the 28–37 year interval between the Voyager epoch and the Cassini observations considered here, which is a small fraction of several hundred years. The Voyager occultation was observed at low incidence angle ($B^* = 5.93^\circ$, $\tan B_{\text{eff}} = -0.239$), comparable to the Cassini low-incidence RSS observations, providing high sensitivity to vertical structure. Fig. 25

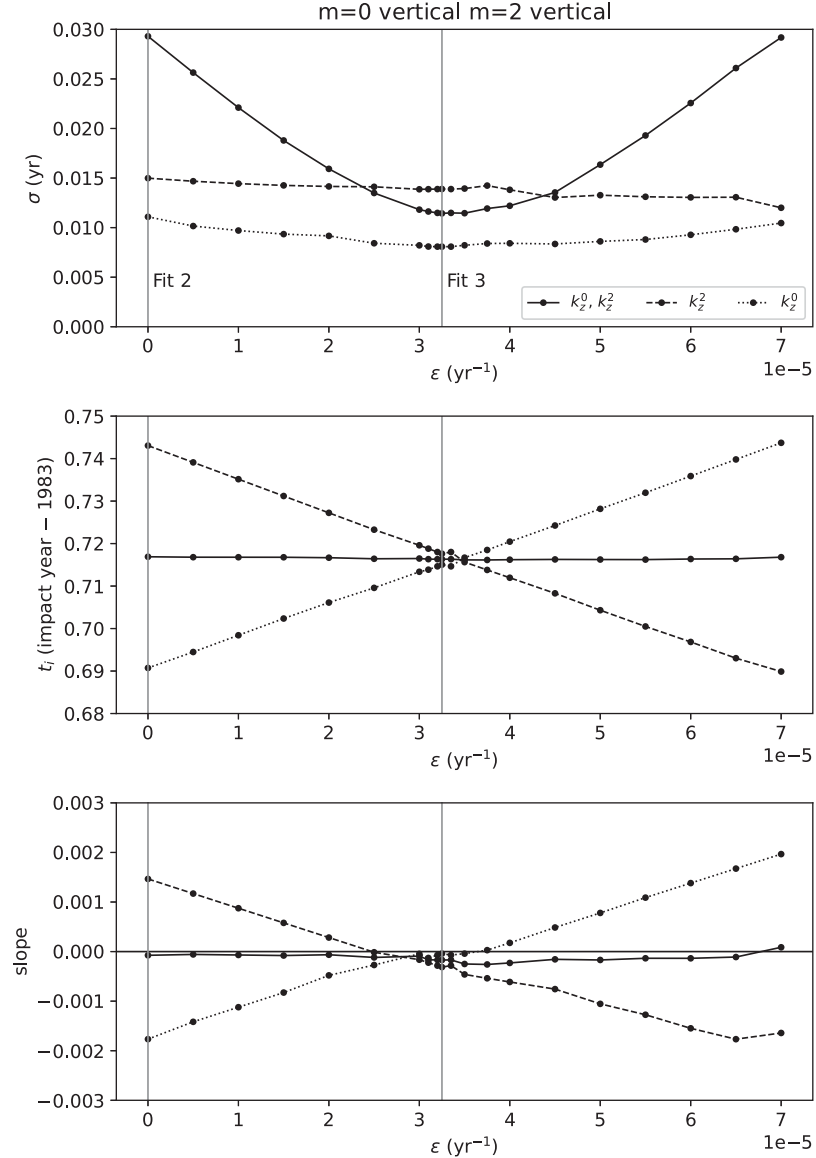


Fig. 22. Sensitivity of the derived impact dates to the ring self-gravity parameter ϵ . Top: The standard deviation σ of the residuals of linear fits to the ensemble of individual estimates of the impact dates based on $k_z^2(t)$, $k_z^0(t)$, and both ($k_z^2(t)$, $k_z^0(t)$), as a function of ϵ . Fit 2 corresponds to the top panel of Fig. 21, with $\epsilon = 0$ (no ring self-gravity). The best fit to (k_z^2 , k_z^0) corresponds to $\epsilon = (3.25 \pm 1.0) \times 10^{-5}$ yr $^{-1}$, marked by a vertical solid line in each panel (Fit 3, shown in the lower panel of Fig. 21). Middle: Impact dates t_i computed separately for the $m = 0$ and $m = 2$ vertical modes, and jointly for both modes, as a function of ϵ . For Fit 3, the impact dates for the two modes are virtually identical. Bottom: Slopes of the individual and combined fits to $k_z^2(t)$ and $k_z^0(t)$, reaching a minimum in absolute value near $\epsilon = 3.25 \times 10^{-5}$ yr $^{-1}$.

shows the *Voyager 1* RSS optical depth profile of the inner C ring at a resolution of 0.2 km. Although somewhat noisier than the *Cassini* observations, which benefited from an exquisite USO (ultra-stable oscillator) that permitted accurate diffraction correction at high spatial resolution, the SNR is adequate to have revealed 1-km periodic structure in the inner C ring similar to what is shown in Fig. 1. No such structure is visible in the data.

Further confirmation of the absence of evidence for a centuries-old impact event is provided by Fig. 26, which shows the power spectrum for the *Voyager* RSS profile over the range 75,300–75,635 km. The predicted wavelengths for $m = 1$ vertical and radial modes, assuming an impact date $t_i = 1300$, are marked by vertical lines. (The date is chosen such that the windup of the $m = 1$ pattern would produce radial structure with a wavelength $\lambda \sim 1$ km characteristic of the observed C ring ripple structure.) The upper panel shows the raw power spectrum,

and the bottom panel is the CFT with the radius scaled appropriately for $m = 1$ waves with a pattern speed given by the nodal precession rate. There are no sharp peaks in the vicinity of the predicted wavenumber, unlike Fig. 12. Peaks near $\lambda = 1.9$ km and 2.8 km are of comparable strength to additional peaks for $\lambda > 3$ km (off-scale in the figure) and are far removed from the $\lambda \sim 1$ -km ripples observed in the *Cassini* data.

The absence of any sign of short-wavelength periodic structure in the 1980 *Voyager* observations is consistent with our inference that the C ring ripple structure visible in the *Cassini* occultation data resulted from an impact that occurred in 1983, several years after the *Voyager* encounter with Saturn. A final compelling argument against a centuries-old origin is provided by estimates of vertical wave damping rates obtained from N-body collisional simulations in Section 6, which show that for any plausible initial $m = 1$ wave amplitude and ring

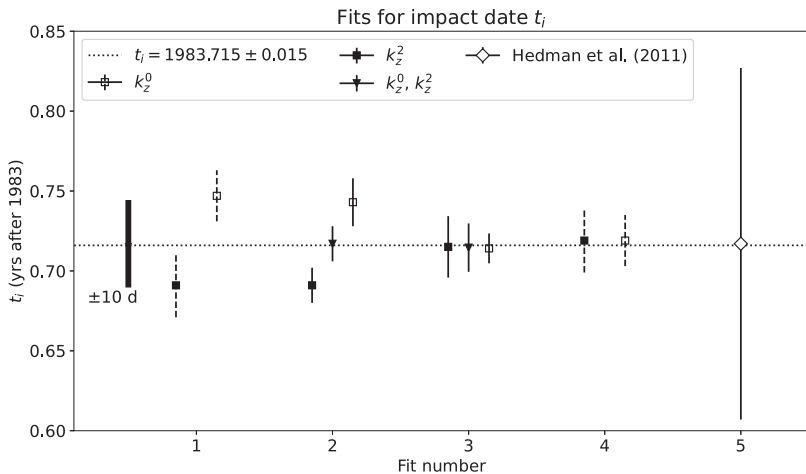


Fig. 23. Impact dates t_i estimated from the series of fits listed in Table 7. The thick vertical bar at left has length ± 10 days. The dotted horizontal line corresponds to the impact date from Fit 3, our adopted fit. Dashed error bars correspond to empirical fits to the observed $k_z^0(t)$ and $k_z^2(t)$ shown in Fig. 20. Solid error bars correspond to fits for t_i based on the averages of dynamical fits to $k_z^0(r_0)$ and $k_z^2(r_0)$ derived separately from power spectral analysis of individual occultation profiles. Fit 5 corresponds to the (Hedman et al., 2011) impact date inferred from an analysis of the $\lambda \sim 30$ km $m = 1$ vertical corrugations visible in Cassini ISS images.

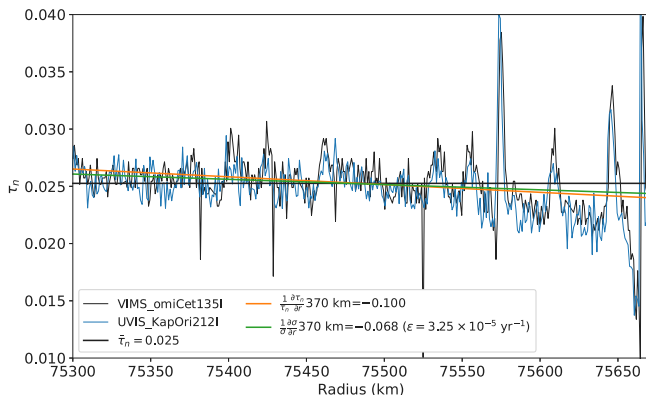


Fig. 24. VIMS_omiCet135I (black) and UVIS_KapOri212I (blue) optical depth profiles for region R75.5, showing very similar mean optical depth and detailed radial structure. The mean optical depth of the VIMS profile over this region is shown as a black line, and a linear fit is shown as an orange line, with a fractional change in optical depth of -0.100 across the 370 km-wide range. The fractional change in surface density derived from the adopted Fit 3 is plotted as a green line, with a variation of -0.068 across the region. (For interpretation of the references to color in this figure legend, the reader is referred to the web version of this article.)

particle properties, the final amplitude ~ 700 years later would be effectively zero.

5. Amplitudes of the $m = 0$ and $m = 2$ vertical waves across the inner C ring

In this section, we describe several methods to estimate the vertical amplitudes A_z^0 and A_z^2 of the $m = 0$ and $m = 2$ vertical corrugations, and their temporal and spatial variability. Hedman et al. (2011) showed that the inferred 1983 impact produced $m = 1$, $\lambda = 30$ km corrugations in Saturn's rings with vertical amplitudes ranging from as much as 25 m in the low optical depth inner C ring (75,000–78,000 km) to as little as 2 m near 83,000 km, where the optical depth reaches a local maximum over a region ~ 1000 km in radial extent. Assuming that the shorter-wavelength ripples visible in the inner C ring were produced during the same impact event as the $m = 1$ corrugations, a comparison of the relative amplitudes of these structures could provide important constraints on the detailed characteristics of the impact itself.

We begin with an overview of the regional variation in the estimated amplitudes A_z^0 and A_z^2 derived from power spectra of the optical

depth profiles. For each region shown in Fig. 1, we computed the CFT spectrum for each occultation event and identified the maximum observed power within a narrow range of wavelengths centered on the predicted wavenumbers k_z^0 and k_z^2 , assuming an impact date $t_i = 1983.7$. Then, as we described in Section 4.3 and illustrated in Fig. 12, we solved iteratively for the model amplitudes A_z^0 and A_z^2 that matched the observed CFT power at the two predicted wavelengths, retaining only those cases in which the CFT of the observations showed statistically significant power near the expected locations. This idealized approach is likely to underestimate the true mode amplitudes because the actual ripple patterns are not perfectly phase-coherent across the 370 km window used for the CFT, as can be seen from the wavepacket examples in Fig. 7. Nevertheless, they provide useful metrics of comparative amplitudes with time and from region to region.

Fig. 27 shows the results of this procedure for the low-inclination RSS events (revs 123–133) from 2010 and VIMS events from 2017. In the upper panel, we show a representative RSS optical depth profile from this set, with each region marked. Below, we show the RSS (middle panel) and VIMS (lower panel) mode amplitudes. The thin blue and orange horizontal lines show the inferred average vertical amplitudes A_z^0 and A_z^2 , respectively, for each region. The mean values for each region are shown by the thick horizontal lines. The amplitudes are largest in the low optical depth R76.6 and R77.7 regions and smaller in R74.9, R76.9, and R77.3, where the mean optical depth is generally higher.

The scatter in the amplitude measurements in Fig. 27 for each region is surprisingly large, especially for the RSS observations. Upon closer inspection, we find that the inferred vertical amplitudes are strongly correlated with $\tan B_{\text{eff}}$, as illustrated in Fig. 28. Here, we show the measured amplitudes A_z^0 for RSS (blue) and VIMS (orange) as a function of $\tan B_{\text{eff}}$ for four regions (R74.9, R75.2, R75.5, and R76.6) for which this correlation is particularly evident. The overplotted lines show the best-fitting linear regression, with the corresponding correlation coefficient ranging from $\rho = 0.54$ to 0.92 . The RSS observations span a larger range of $\tan B_{\text{eff}}$ than the VIMS measurements, accounting for the larger scatter in measured amplitudes just noted. We choose $\tan B_{\text{eff}} = 0.4$ as a reference value at which to compute the ratio of the RSS to VIMS amplitudes, computed from the best-fitting linear fits to each set of measurements, yielding $A_z^0(\text{RSS 2010})/A_z^0(\text{VIMS 2017}) = 1.94 - 2.54$ for these four regions.

The empirical correlation between the estimated vertical amplitudes and $\tan B_{\text{eff}}$ is somewhat surprising, since our simple geometric model for the ring optical depth is designed to account for the effects of

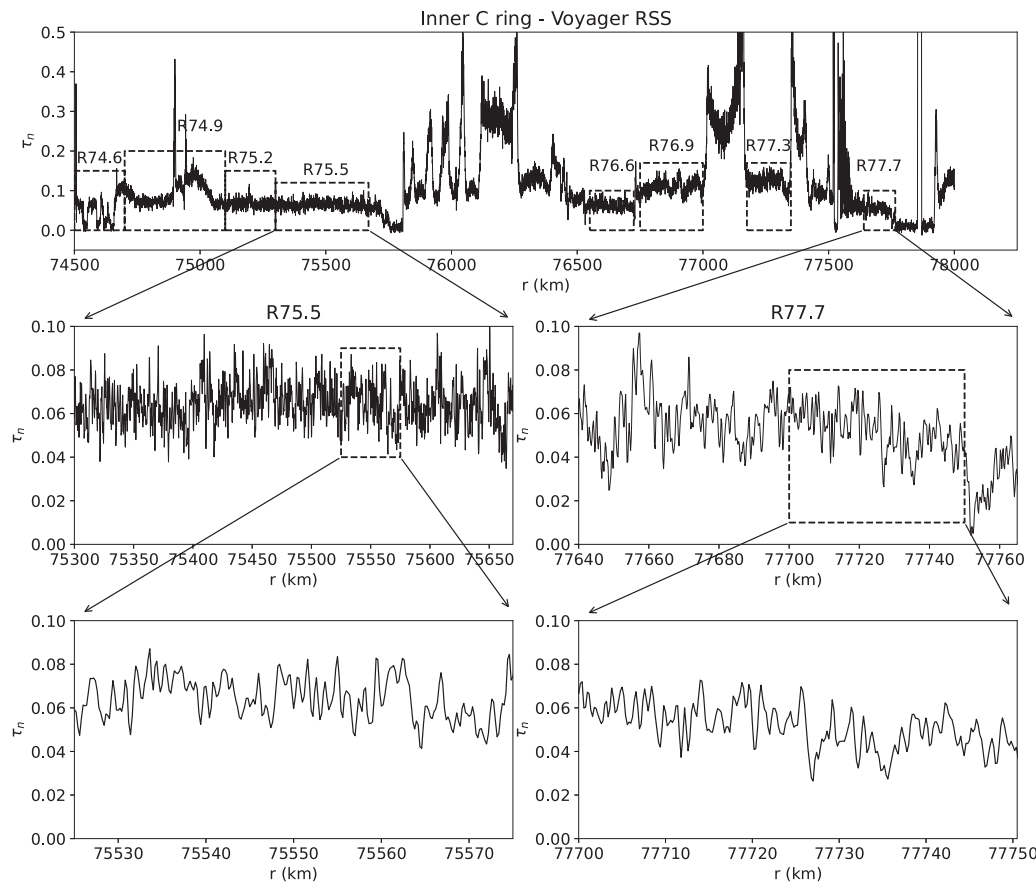


Fig. 25. The radial normal optical depth profile of the inner C ring, from the *Voyager 1* RSS X-band occultation of 1980 Nov 13 observed at low incidence angle ($B^* = 5.93^\circ$, $\tan B_{\text{eff}} = -0.239$). The RSS data were diffraction-corrected with a processing resolution of 0.2 km. No ripple structure is visible. Compare to Fig. 1.

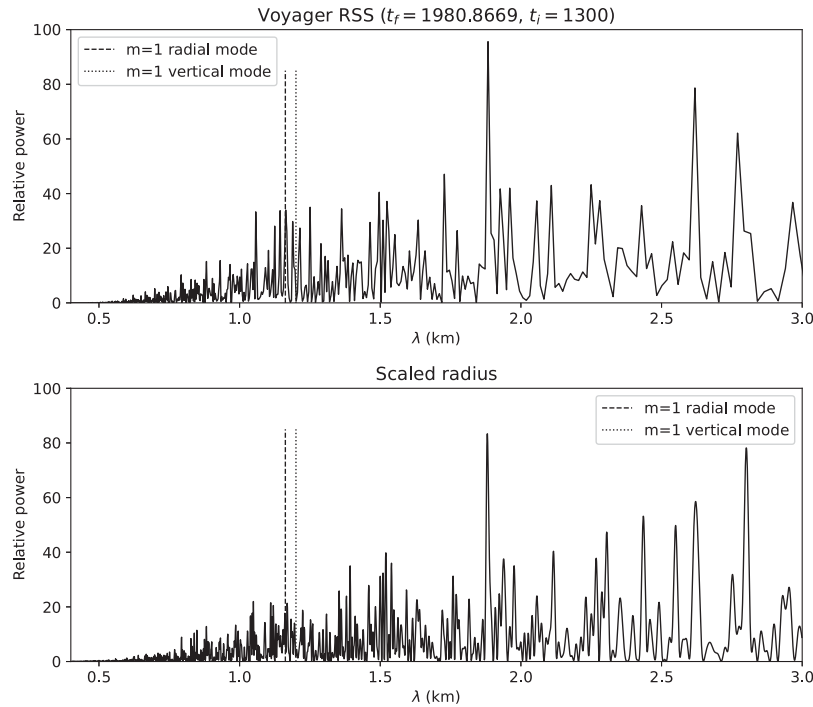


Fig. 26. CFT spectra of the *Voyager* RSS Saturn ring occultation profile for R75.5 and a reference radius $r_0 = 75,500$ km, over a wavelength range chosen to reveal any 1-km wavelength periodic structure comparable to what is visible in the more recent *Cassini* observations. The predicted $m = 1$ vertical and radial mode wavelengths are marked for an assumed impact date $t_i = 1300$. The top panel shows the power spectrum using the nominal radius scale, with no evident power in the vicinity of $\lambda \sim 1$ km. In the bottom panel, the radius has been scaled to account for the predicted radial dependence of an $m = 1$ spiral structure. Unlike the case for the *Cassini* observations shown in Fig. 12, there are no sharpened narrow peaks in the power spectrum characteristic of spiral structure with the expected radial dispersion.

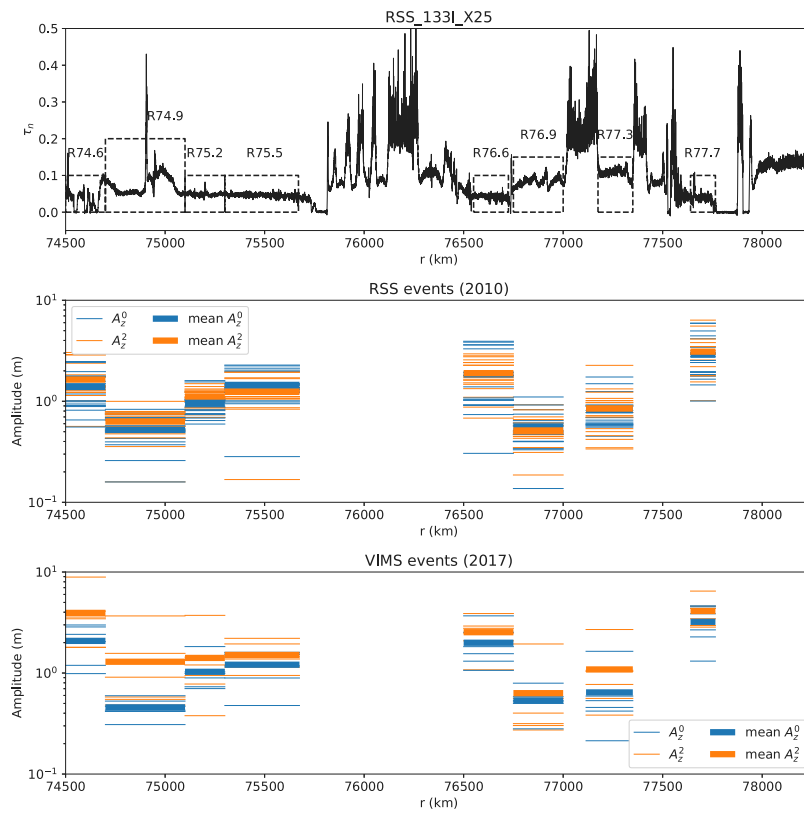


Fig. 27. Average mode amplitudes A_z^0 and A_z^2 for each of the regions labeled in the optical depth profile in the upper panel, computed from RSS observations in 2010 (middle panel) and VIMS observations in 2017 (lower panel). For each labeled region, the CFT power spectrum was computed for each data set and the mean amplitudes A_z^0 and A_z^2 were estimated by comparing the observed power peaks near the predicted wavenumbers with values from an idealized composite wave model. The individual estimates from each data set are shown as thin horizontal lines, color-coded by mode, and the mean values for each region are shown as bold horizontal lines. Generally, the amplitudes are anticorrelated with ring optical depth. (For interpretation of the references to color in this figure legend, the reader is referred to the web version of this article.)

viewing geometry (see Eqs. (62) and (63)). However, a similar correlation is present in the estimates of the $m = 1$ corrugation amplitude derived from near-equinox images (Hedman et al., 2011). In particular, the brightness variations shown in Figure S2 of that paper, which are derived from observations obtained at $\tan B_{\text{eff}} > 0.3$, yield corrugation amplitudes roughly a factor of two greater than those derived from observations obtained closer to equinox at $\tan B_{\text{eff}} < 0.25$. We have not yet identified a sensible way to model these variations of the inferred vertical amplitude on the effective ring opening angle, and so we leave that task for future work. Instead, we will simply make use of the RSS/VIMS amplitude ratios at a common $\tan B_{\text{eff}}$ (as illustrated in Fig. 28) to estimate the time history of the mode amplitudes since the original impact.

The estimates shown in Fig. 27 are useful for revealing general trends in the A_z^0 and A_z^2 mode amplitudes across the entire inner C ring, but to get a more detailed view of radial variations, we make use of the regional power spectral analysis of R75.5, which provides an estimate of A_z^0 and A_z^2 for each position of the sliding boxcar window. The overlap of the data included in successive boxcar windows limits the radial resolution, but the averaging process increases the accuracy of the mean amplitudes. Fig. 29 compares the radial profiles of $A_z^0(r)$ and $A_z^2(r)$ for the early RSS events (revs 057–067) from 2008, the later RSS events (revs 123–133) from 2010, and the VIMS observations (revs 268–274) from 2017. Each amplitude profile is derived from a separate occultation data set, and the figure includes results from a range of $\tan B_{\text{eff}}$. Note that the amplitudes are somewhat larger than those shown in Fig. 27 because the ripples are more phase-coherent over the limited boxcar radial width than over the full range used for the power spectrum amplitude estimates. For all three periods, the amplitudes of both modes rise gradually to a maximum value near

75,600 km. There is also a notable decrease in amplitude with the passage of time across the three panels. We will return to this pattern in Section 6 below, when we characterize the temporal damping behavior of the A_z^0 and A_z^2 amplitudes.

We noted above that power spectrum method of determining wave amplitudes provides average values that may well underestimate locally-determined amplitudes, since they are based on a constant-amplitude model that perfectly matches the normalized radius scale used to compensate for the dispersion of the wave across the radial range of the spectrum. An alternative approach is to perform wavepacket fits similar to those in Fig. 7 for all such features in the observations, using a two-component model for $\tau(r)$ computed for the geometry of each event and radial location. We identified a set of radial windows that contained such wavepackets and performed a series of robust least-squares fits designed to span the full range of parameter space and thereby avoid false convergence to a local minimum. Fig. 30 shows the results of this ensemble of fits. The top row shows the results for R75.5, with fitted amplitudes A_z^0 from each wavepacket fit shown at left and the corresponding A_z^2 shown at right. RSS observations from revs 123–133 are plotted in blue, with typical values of ~ 5 m (similar to those seen in Fig. 14 for R75.5), and VIMS events from 2017 are shown in orange. For comparison, we include the amplitude profiles obtained from power spectral analysis (Fig. 29) for these two sets of observations. The wavepacket fits give somewhat larger local amplitudes than the regional averages by a factor of about 2. In the bottom row of the figure, we show the wavepacket results for region R77.7, which exhibit somewhat higher amplitudes, with typical values of ~ 10 m (similar to those seen in Fig. 14 for R77.7) and reaching 30 m in some cases. There are no obvious systematic differences between the amplitudes of the 2010 RSS wavepacket fits and the VIMS results from 2017, but

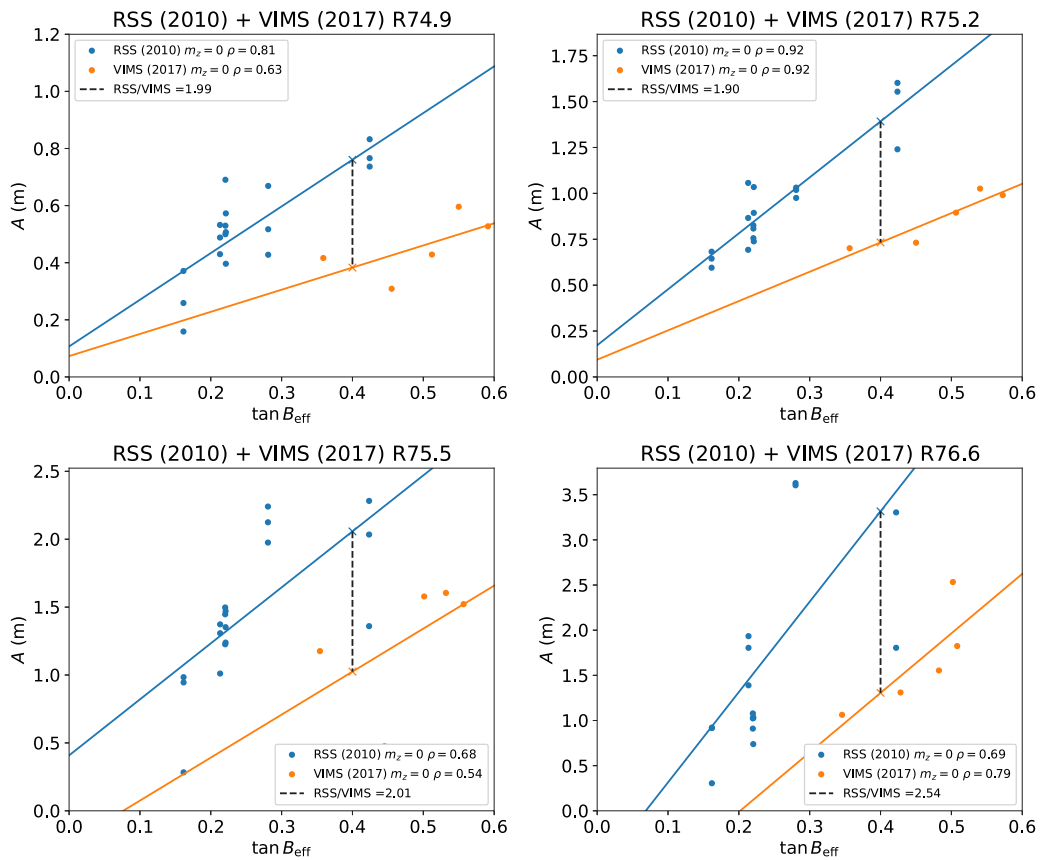


Fig. 28. Trends in the inferred RSS (2010) and VIMS (2017) mode amplitudes A_z^0 with $\tan B_{\text{eff}}$, for radial regions R74.9, R75.2, R75.5, and R76.6 (from upper left to lower right). The best-fitting linear model to each set of observations is shown as a solid line, with correlation coefficient ρ as given in the legend. The ratio of the RSS (2010) and VIMS (2017) mode amplitudes is estimated in each case from the values of the fitted lines at $\tan B_{\text{eff}} = 0.4$, shown by the vertical dashed lines, with $A_z^0(\text{RSS 2010})/A_z^0(\text{VIMS 2017}) = 1.94 - 2.54$ for these four regions. (For interpretation of the references to color in this figure legend, the reader is referred to the web version of this article.)

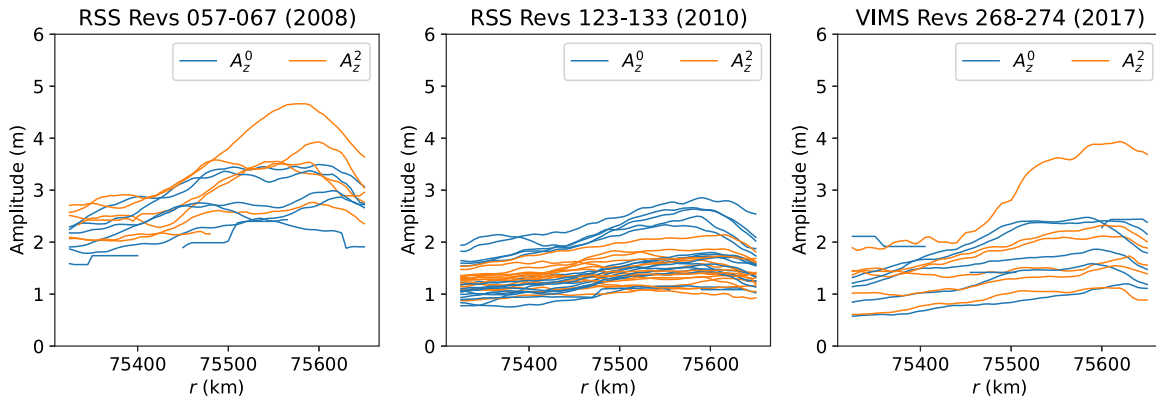


Fig. 29. Mode amplitudes A_z^0 and A_z^2 derived from regional power spectra of region R75.5 (75,300–75,670 km) for three time periods: the 2008 early RSS observations (revs 057–067) at left, the later 2010 low-inclination RSS events (revs 123–133) in the middle panel, and the 2017 series of VIMS observations (revs 268–274) at right. A window halfwidth $w = 200$ km was used in all cases. Both modes show a gradually rising amplitude with radius, reaching a peak near 75,575 km. There is a significant decline in the amplitudes of both modes over the nine year interval from left to right, suggesting that there has been detectable damping on a decadal timescale. (Note that the observations span a range of $\tan B_{\text{eff}}$, which as shown in Fig. 28 has a systematic effect on the inferred amplitudes.) (For interpretation of the references to color in this figure legend, the reader is referred to the web version of this article.)

as a reminder the two sets of observations sample different ranges of $\tan B_{\text{eff}}$, which systematically affects the inferred amplitudes, as shown in Fig. 28.

6. Damping behavior

In this section we address the damping of vertical and radial kinematic waves via direct collisional simulations. We employ a local

method based on a co-moving simulation region with periodic boundary conditions (Salo et al., 2018). In local simulations, only the $m = 0$ mode can be directly analyzed. However, due to the small pitch angle of the $m \neq 0$ waves we may assume that their damping behavior is similar to the axisymmetric mode. Due to the periodic boundaries, the radial wavelength of the simulated wave must be an integer fraction of the radial size of the calculation region. In the actual rings, kinematic perturbations wind up with time, with a rate determined by the local

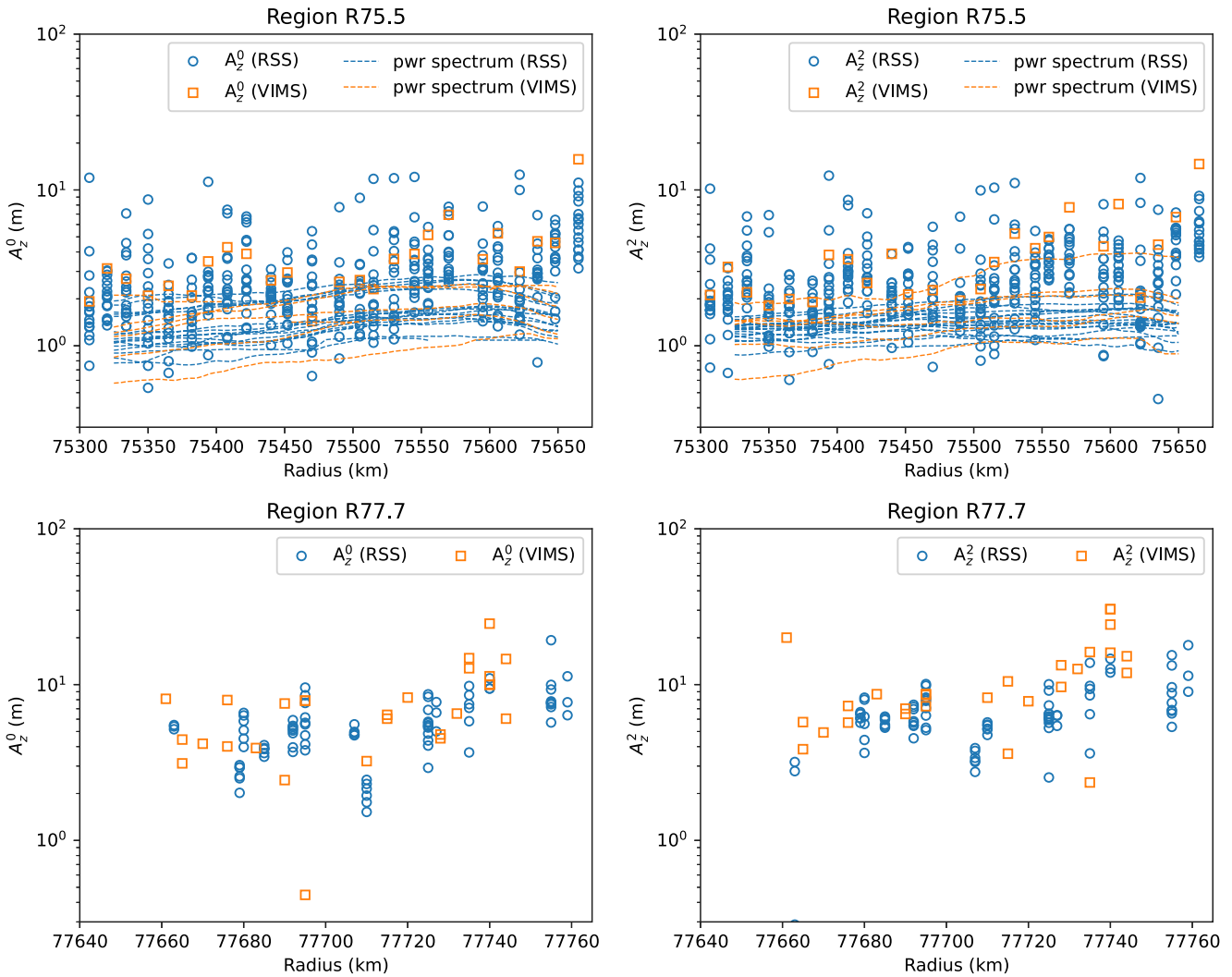


Fig. 30. Mode amplitudes A_z^0 and A_z^2 derived from model fits to individual wavepackets. The top row shows the results for region R75.5, with the radial location of each wavepacket on the horizontal axis and the corresponding fitted mode amplitudes A_z^0 and A_z^2 shown in the left and right panels. Blue symbols mark RSS observations from 2010 and orange symbols mark VIMS observations from 2017. For comparison, the radial trends in amplitude computed from regional power spectra (Fig. 29) are included as dashed lines. The bottom panels show the results of wavepacket fits for region R77.7, with somewhat larger average amplitudes than in R75.5. Similar results are visible in Fig. 14, which shows ~ 1 km wavelength ripples with vertical amplitudes of $\sim 5\text{--}10$ m, and somewhat larger amplitudes for R77.7 than for R75.5.

gradient of κ and μ for radial and vertical modes, respectively (see Eqs. (8) and (9)). Our strategy is to measure the damping rate using simulations with various fixed radial extents, and to determine how the amplitude decay rates scale with the viscosity of the system and the instantaneous wavelength of the wave. This enables us to deduce the expected time evolution of the wave amplitude, which can then be compared with the radial amplitude variations derived from occultation observations.

Since self-gravity has only a small effect (quantified below) on the viscosity of low optical depth regions of the C ring, most of our simulations assume non-gravitating particles. For simplicity, the collisions assume a constant coefficient of restitution ϵ_n , in which case the simulated viscosities scale with $R^2\Omega$, where R is the particle radius and Ω the angular velocity. The proportionality factor depends on the dynamical optical depth τ and the assumed value of ϵ_n , with viscosity increasing for less dissipative impacts. For small $\tau \lesssim 0.5$, viscosity increases linearly with τ . We may thus easily scale simulations performed with a given set of R , τ , and Ω to other cases. For our nominal parameters we use $R = 1$ m, $\tau = 0.05$ (corresponding to $\tau_{RSS} = 0.1$), and a reference orbital radius $a = 75,000$ km. In the standard

$\tau = 0.05$ simulation, the number of test particles is $N = 4000$, the radial size of the simulation region is $L_x = 1000$ particle radii and tangential size is $L_y = 251.32$ particle radii. For some simulations, we used larger N . We present most of the simulation results in a non-dimensional form, except when compared directly to observations.

A typical simulation example of wave amplitude damping is shown in Fig. 31. A radially-dependent sinusoidal perturbation was imposed in either the z-coordinate (left) or the radial velocity (right) of the particles, with wavelength equal to the radial size of simulation region (500 m). The initial epicyclic amplitude was 20 m in both cases. Labels indicate the time since the perturbation, measured in orbital periods; before the perturbation was applied, the system was evolved for 100 orbital periods to ensure that a steady state had been reached. Notice the substantial vertical and radial damping over just 2000 orbital periods (a bit more than a year) for this high-viscosity case.

In the hydrodynamic approximation, ignoring the ring's self-gravity, the amplitude Z of a vertical corrugation satisfies the equations

$$\frac{\partial^2 Z}{\partial t^2} = -\mu^2 Z + v_z \frac{\partial^2 W}{\partial r^2} \quad (78)$$

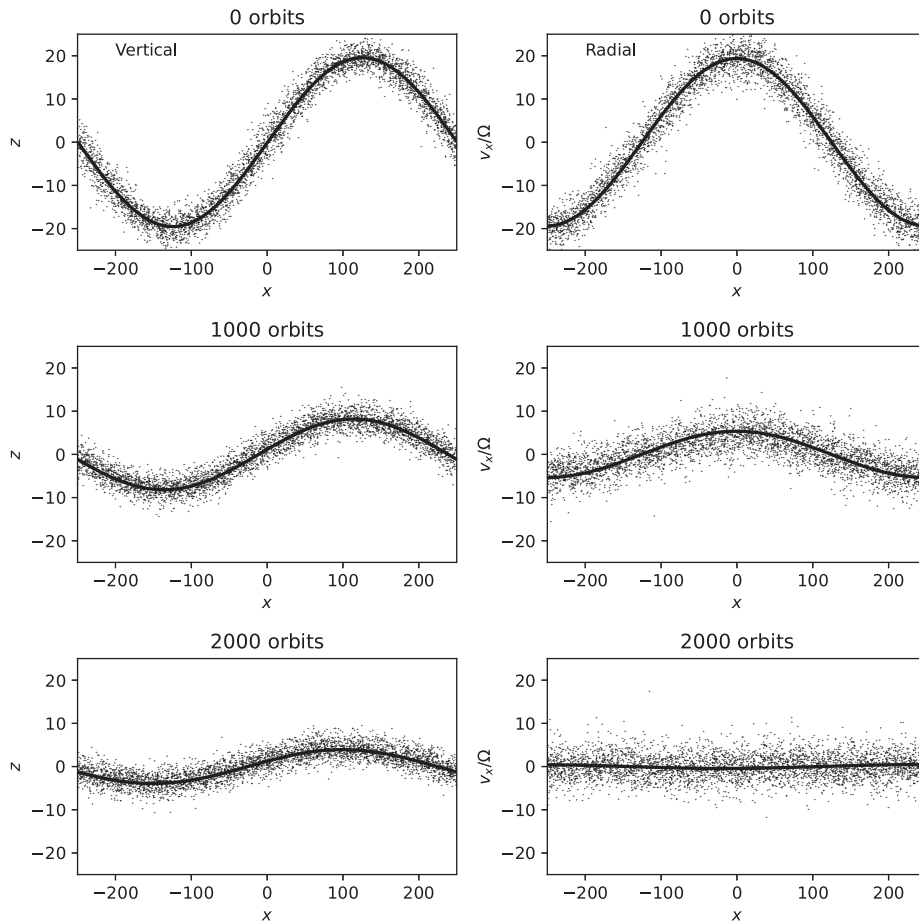


Fig. 31. Example of wave damping in N-body collisional simulations, for dynamical optical depth $\tau = 0.05$, coefficient of restitution $e_n = 0.5$, and particle radius $R = 1$ m. A radially-dependent sinusoidal perturbation was imposed in either the z-coordinate (left) or the radial velocity (right) of the particles, with wavelength equal to the radial size of simulation region. Labels indicate the time since the perturbation, measured in orbital periods. In this simulation, the self-gravity of ring particles was not included. However, similar damping behavior is seen in simulations with self-gravity. See text for details.

$$W = \frac{\partial Z}{\partial t}. \quad (79)$$

This system has a solution of an exponentially damped sinusoidal oscillation:

$$Z(t) = Z(0) \cos(\omega t + k_z r) e^{-\gamma t}, \quad (80)$$

where

$$\omega^2 = \mu^2 - \gamma^2 \quad (81)$$

and

$$\gamma = \frac{1}{2} v_z k_z^2 \quad (82)$$

In practice, $\gamma \ll \mu$ and the wave oscillation frequency $\omega \approx \mu$, whereas the exponential damping rate depends on viscosity v and the wavenumber squared k_z^2 .

6.1. Simulation results

To confirm the anticipated k_z^2 dependence of the damping rates and to measure the viscosities v_z , we performed simulations where a vertical perturbation was added to the positions and velocities of the particles, depending on their radial x position as

$$\Delta z = A_z \sin(k_z x) \quad (83)$$

$$\Delta v_z = A_z \Omega \cos(k_z x), \quad (84)$$

which produces a traveling sinusoidal wave with $Z(0) = A_z$. In most of our simulations, $k_z = 2\pi/L_x$, where L_x is the radial extent of

the calculation region, corresponding to one wavelength. The above perturbation is applied after the simulation system has settled to a steady state, characterized by a velocity dispersion determined by the assumed e_n . For small $\tau \rightarrow 0$, the velocity dispersion does not depend on optical depth. During the simulation, a radial Fourier fit to the mean vertical position of the particles is performed (see Fig. 31) and tabulated as a function of time; in the case of a traveling wave, the fitted instantaneous Fourier amplitude equals the wave amplitude. We then perform an exponential fit to the wave amplitude versus time:

$$A_z(t) = A_z(0) e^{-\gamma t} \quad (85)$$

$$= A_z(0) e^{-t/t_{ez}}, \quad (86)$$

where t_{ez} is the e-folding time of vertical amplitude. In non-dimensional form,

$$T_{ez} = t_{ez}/t_{per} = \frac{2}{(2\pi)^3} \left(\frac{v_z}{\Omega R^2} \right)^{-1} \left(\frac{\lambda_z}{R} \right)^2, \quad (87)$$

where $\lambda_z = 2\pi/k_z$ and $t_{per} = 2\pi/\Omega$ is the orbital period.

In the hydrodynamic treatment of vertical waves, the damping factor v_z is often identified with the kinematic viscosity v , related to the radial transport rate of angular momentum. However, since hydrodynamics provides only an approximation for the ring behavior (see, e.g., Latter and Ogilvie, 2008 and Schmidt et al., 2009), we will simply refer to v_z as the vertical viscosity. In our simulations, the derived value of v_z provides a direct measure of the rate of wave damping, which is the quantity we want to compare with observations.

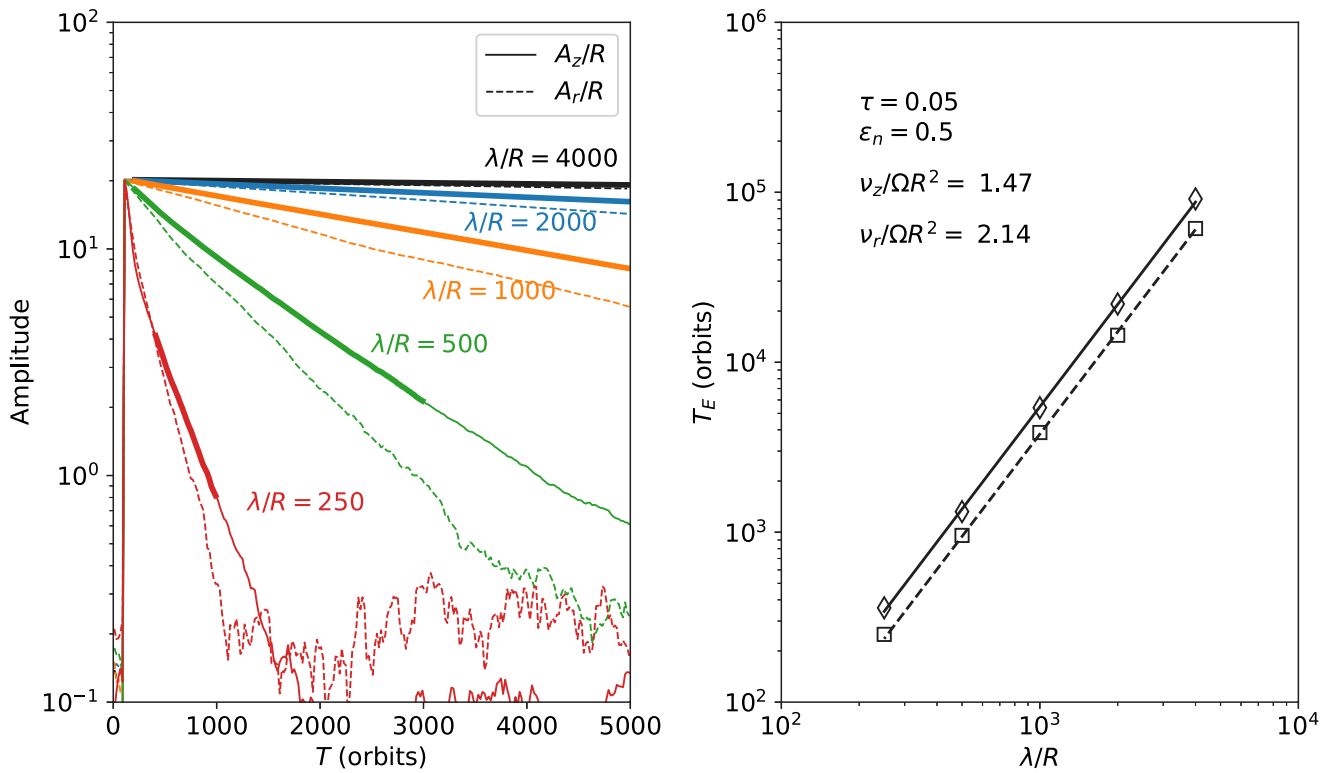


Fig. 32. Damping of vertical (solid curves) and radial (dashed curves) oscillation amplitudes. Left panel: Each curve corresponds to time evolution in a separate run, with a different radial size of the local simulation region. A radius-dependent sinusoidal perturbation was imposed in either the z-coordinate or the radial velocity of the particles, after $T = 100$ orbital periods, with wavelength equal to radial size of simulation region, and initial amplitude corresponding to 20 particle radii. The e-folding times of exponential decay were obtained from linear fits of the logarithm of amplitude versus time, over the range indicated by thicker lines (the same time range was used for runs with radial and vertical perturbations; for clarity, these are marked only in A_r). Right panel: The e-folding time of the perturbation, measured in orbital periods. A constant coefficient of restitution $\epsilon_n = 0.5$ and the dynamical optical depth $\tau = 0.05$ were assumed. In case of constant ϵ_n the viscosities scale proportionally to ΩR^2 . The lines indicate the quadratic dependence between T_e and λ using the fitted values of v_z and v_r indicated by the labels.

For the damping of radial waves, a similar equation applies:

$$T_{er} = t_{er}/t_{per} = \frac{2}{(2\pi)^3} \left(\frac{v_r}{\Omega R^2} \right)^{-1} \left(\frac{\lambda_r}{R} \right)^2, \quad (88)$$

where $\lambda_r = 2\pi/k_r$. In the hydrodynamic approximation, the v_r term in Eq. (88) is replaced by $7v/3 + \xi$, where ξ is the bulk viscosity (Shu, 1984). The identification of v_r with the hydrodynamic counterpart is as problematic as that of v_z , even more so due to ambiguity in the meaning of bulk viscosity for planetary rings. In principle, ξ can be directly measured in N-body simulations, as a proportionality factor between radial compression and the deviation of pressure from its steady-state value (Salo et al., 2001; Schmidt et al., 2001). However, in practice, ξ acts merely as a proxy for the energy exchange between various components of velocity ellipsoid induced by compression (Latter and Ogilvie, 2008), and is not properly captured by the hydrodynamic treatment, which assumes an isotropic velocity distribution. Regardless of its hydrodynamic interpretation, the radial viscosity v_r derived directly from simulations is the quantity we want to compare to observations.

For practical reasons, when measuring the radial damping, the initial perturbation is added only to radial velocities

$$\Delta v_x = A_r \Omega \cos(k_r x), \quad (89)$$

rather than to particle positions, since adding radial displacements would result in particle overlaps. The radial wave produced in this manner is a standing wave, and its instantaneous amplitude derived from the Fourier fit equals the wave amplitude only after an integer number of perturbation half-periods. Since our applied sampling interval of Fourier amplitudes (roughly 40 times/orbit) is not an exact fraction of orbital period, we first tabulate the maximum of radial velocity Fourier amplitudes over five orbital periods and fit these maximum values over

the corresponding tabulation times, prior to performing an exponential fit to the decay of A_r with time.

Fig. 32 compares the amplitude damping over time for different perturbation wavelengths. In the left panel the time evolution of vertical (solid) and radial amplitudes (dashed) is shown, while in the right panel the fitted damping parameters, converted to T_e , are plotted as a function of λ/R . (The examples shown in Fig. 31 are from the $\lambda/R = 500$ simulations.) The simulated decay rates clearly confirm the expected quadratic trend predicted by a hydrodynamic treatment. The labels indicate the fitted values of v_z and v_r , corresponding to the lines shown overplotted on the individual damping coefficients derived for various wavelengths. As a general result, the ratio $v_r/v_z \approx 1.4$, consistent with the faster decay of the radial perturbation seen in Fig. 31.

Fig. 33 summarizes the fitted values of v_z and v_r from simulations performed with different values of ϵ_n and τ . For less dissipative particles (larger ϵ_n) the steady-state velocity is larger, which leads to strongly increased v_z and v_r . Roughly, viscosities are proportional to the square of the velocity dispersion. Measured in terms of effective vertical thickness $H = \sqrt{12z^2}$ (which is proportional to the velocity dispersion), $H/R = 2.5$ for $\epsilon_n = 0.1$, increasing to $H/R \approx 6$ and 12 for $\epsilon_n = 0.5$ and 0.6, respectively. Over this range of elasticity, the ratio v_z/H^2 varies by less than 10%. This behavior of v_z and v_r is consistent with the similar trends of kinematic viscosity (Salo et al., 2018), although the magnitudes are different: the fitted v_z is roughly a factor ten larger than the kinematic viscosity measured from the same simulations. The expected small- τ linear dependence of viscosities on optical depth is also confirmed (see the inset figure).

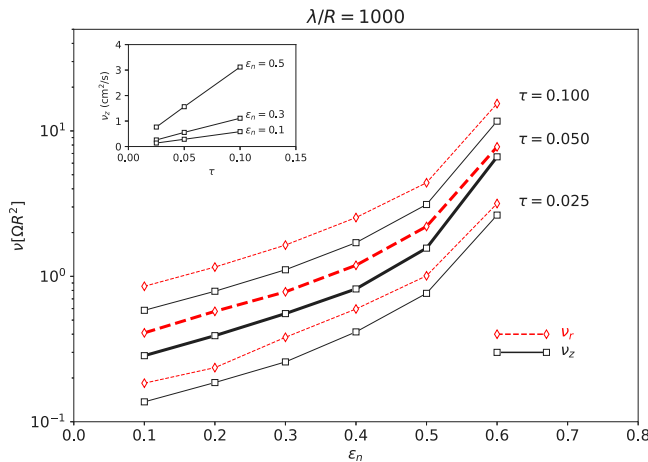


Fig. 33. The dependence of measured v_z and v_r on ϵ_n , for three different optical depths. The inset figure shows v_z as a function of τ for $\epsilon_n = 0.1, 0.3, 0.5$, highlighting the linear dependence on optical depth. In all cases $v_r/v_z \sim 1.4$.

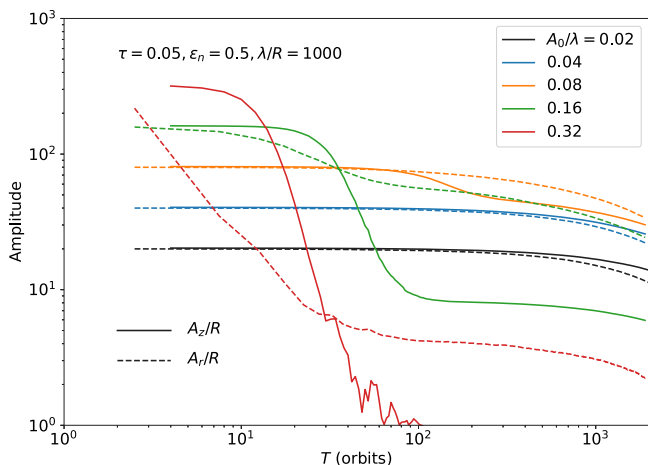


Fig. 34. Effect of damping on the initial $m \neq 1$ perturbation amplitude. The time evolution of vertical (solid curves) and radial (dashed) amplitudes is shown for $\epsilon_n = 0.50$ and $\tau = 0.05$. Five simulations are compared, using larger and larger initial amplitudes; the black curves correspond to Fig. 32 with $A(0)/\lambda = 0.02$. Doubling the fractional amplitude to 0.04 leads to nearly identical exponential decay (note that here log-log axes are used). However, for still larger $A(0)/\lambda$ the amplitudes show an increasingly drastic initial drop. This collapse is particularly strong for the vertical amplitudes and takes place when $A(0)/\lambda \gtrsim 0.08$.

In all of the above examples, the initial perturbation had a small epicyclic amplitude compared to the radial wavelength of the disturbance. In this case the decay of amplitudes followed the expected exponential trend. Fig. 34 explores what happens if the initial amplitude is large. Compared to the nominal case of Fig. 32, where $A(0)/\lambda_z = 0.02$, this ratio is increased by successive factors of two. Doubling the $A(0)/\lambda_z$ ratio yields identical behavior, but when $A(0)/\lambda_z$ is further increased, there is a rapid initial collapse of the amplitude. Signs of this are evident when the vertical amplitude reaches $A(0)/\lambda_z = 0.08$ (note that this corresponds to a large maximal slope, $\frac{\partial A_z}{\partial x} = 2\pi A(0)/\lambda \approx 0.5$), and become catastrophic for larger values of $A(0)/\lambda_z$. For radial perturbations, the amplitude drop is weaker but still pronounced when $A(0)/\lambda_r \gtrsim 0.16$.

As tests of our numerical results, we confirmed that the decay rates of vertical and radial amplitudes are unaffected if both waves are simultaneously present (using initial amplitudes $A(0)/\lambda = 0.02$). We also confirmed that the tangential size of the calculation region was large enough not to affect damping rates, and that simulating waves

with several wavelengths within the calculation region gave similar results to that of a single wavelength.

The simulations just described did not include the effects of ring self-gravity. In the case of the C ring, the contribution of gravitational viscosity due to self-gravity wakes can be expected to be insignificant compared to total viscosity, in particular when such small optical depths ($\tau < 0.5$) are considered.⁸ However, even at low optical depths, the gravitational binary encounters between particles modify the steady-state velocity dispersion and impact frequency, and thereby also change somewhat the local and non-local contributions to viscosity. To quantify this effect on the expected damping rates, we carried out additional N-body simulations that included self-gravity, with $\tau = 0.05$, $\rho = 900 \text{ kg m}^{-3}$, and $a = 75,000$, covering $\epsilon_n = 0.1 - 0.6$. As shown in Fig. 35, for $\epsilon_n < 0.4$ the inclusion of self-gravity enhances both v_z and v_r , by as much as a factor of two for $\epsilon_n = 0.1$. This follows from the gravitational scattering in close binary encounters, which correspond to completely elastic impacts, so that the combined effect of dissipative physical impacts and gravitational encounters is similar to that obtained by using a somewhat larger effective ϵ_n (see Hämeen-Anttila and Salo, 1993). However, gravitational scattering is effective only as long as the velocity dispersion is less than or of the order of the mutual escape velocity of particle pairs. Thus the increase in v_z and v_r gets smaller for larger ϵ_n , as the velocity dispersion maintained by impacts alone becomes comparable to or larger than the mutual escape velocity. Furthermore, for $\epsilon_n > 0.5$, the inclusion of self-gravity actually reduces the steady-state velocity dispersion and thereby also v_r and v_z . This follows from the gravitational speed-up of physical impact velocities, leading to slightly enhanced dissipation and thereby a reduced steady-state velocity dispersion, and consequently to smaller viscosities.

Overall, the inclusion of self gravity makes the damping rates somewhat less dependent on ϵ_n . The scaling of damping rates with particle size and optical depth (as long as τ is small) is similar to that in non-gravitating simulations, with $v_{r/z} \propto \tau R^2$. Note that the changes due to self-gravity shown in Fig. 35 represent a maximum effect one can expect, as the actual ring particles are likely to have lower internal density than that of solid ice, as assumed in the simulations.

6.2. Application to observations

From our N-body simulations of vertical and radial wave perturbations, we have established how the damping behavior depends on the instantaneous perturbation wavelength as a function of τ , R and ϵ_n . We now estimate the time dependence of the damping. Since the timescale of wavelength evolution is long (years) compared to the establishment of ring steady-state (less than 50 orbital periods, or about a week, even for τ as small as 0.05), we can combine Eq. (86) for the amplitude decay,

$$dA/dt = -\gamma A \quad (90)$$

$$= -\frac{1}{2}\nu k^2 A \quad (91)$$

with the time evolution of the wavenumber of the perturbation,

$$k(r, t) = k_0(r) + \dot{k}(r)t, \quad (92)$$

where k_0 is the initial wavenumber at $t = 0$, and \dot{k} is the windup rate depending on the type of perturbation (see Eqs. (31), (32), (36), and (37)). Combining these equations gives

$$dA/A = -\frac{1}{2}\nu(k_0 + \dot{k}t)^2 dt, \quad (93)$$

⁸ See, for example, Fig. 11 in Salo et al. (2018), or Fig. 7 in Daisaka et al. (2001); assuming an internal density $\rho < 900 \text{ kg m}^{-3}$ and Saturnocentric distance 75,000 km corresponds to $r_h < 0.62$.

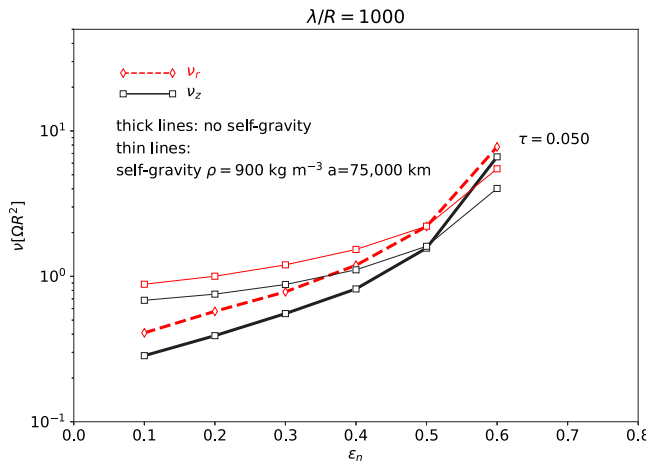


Fig. 35. The effect of self-gravity on the viscosity factors v_r and v_z , as a function of particle elasticity ϵ_n . The thick lines are the same non-gravitating curves for $\tau = 0.05$ as in Fig. 33. The thin lines are the same when including self-gravity, assuming a Saturnocentric distance 75,000 km and particle internal density $\rho = 900 \text{ kg m}^{-3}$. For smaller ρ or smaller distance, the self-gravitating curve would be closer to non-gravitating case. The effect of self-gravity is to reduce the dependence of v_r and v_z on ϵ_n . The scaling of viscosity factors with particle size and optical depth is similar to the non-gravitating case.

which integrates to

$$A(t) = A(0) \exp \left[-\frac{1}{2} \nu \left(\frac{1}{3} k^2 t^3 + k k_0 t^2 + k_0^2 t \right) \right] \quad (94)$$

$$= A(0) \exp \left[-\frac{1}{6} \nu k^2 t^3 \right], \quad (95)$$

where the second expression follows from setting the initial wavenumber k_0 to zero (infinite wavelength), and ν is set to v_z or v_r , depending on the assumed perturbation.⁹

Fig. 36 applies Eq. (95) to estimate the damping of the initial perturbation amplitude in 2017.5 (i.e., 33.8 years since the perturbation in 1983.7). The fractional amplitude is calculated using viscosities based on the τ_{RSS} profile of the observed C ring region, utilizing the v_z and v_r values derived above for $\tau = 0.05$, the assumed coefficient of restitution ϵ_n , and particle radius R . At the upper left, we assume $\epsilon_n = 0.5$ and $R = 1 \text{ m}$. In this case, in regions with $\tau_{RSS} = 2\tau \sim 0.05$, the current vertical amplitudes are estimated to be $\sim 20\%$ of the initial values, whereas the surviving radial amplitudes are only half of that. Because of the τ dependence of viscosities, in regions of $\tau_{RSS} \gtrsim 0.1$ the initial perturbation has been damped nearly completely. At the upper right, ϵ_n is reduced to 0.3, resulting in substantially less damping than for $\epsilon_n = 0.5$. On the other hand, increasing the particle size to $R = 2 \text{ m}$ (lower left) results in very strong damping across the entire inner C ring. For comparison, the lower right shows the estimated damping of an $m = 1$ pattern over a time span of 25.9 yr (appropriate for the *Cassini* low-inclination images used in the Hedman et al., 2011 analysis). We have assumed that the measured behavior of $m \neq 1$ waves can be

⁹ It is of interest to compare the $e^{-(t/t_d)^3}$ dependence in Eq. (95), where $t_d^3 = 6/(v_r k^2) = 8/3 a^2 / (\nu_r \Omega^2)$, to Eq. (65) in Hedman et al. (2022), having a similar form with $t_d^3 = 8/7 a^2 / (\nu \Omega^2)$ for $m = 0$ or 2, when letting $\kappa_L = \Omega$ and $r_L = a$. These are equal if we identify $v_r = 7/3 \nu + \xi$, and omit the bulk viscosity ξ , as done by Hedman et al. (2022). In our case, the $e^{-(t/t_d)^3}$ dependence follows from the wrapping of the kinematic wave with time, while in the case of a forced density wave (or bending wave), the wavelength is reduced when the wave propagates away from the exact resonance. This leads to a wave amplitude proportional to $e^{-(x/x_{\text{res}})^3}$ (Shu, 1984 Eq. (98)), where x is the radial displacement from exact resonance. Converting the radial displacement to time by dividing by the wave group velocity leads to the time dependence in Hedman et al. (2022) Eq. (65), or Eqs. (63) and (98) in Shu (1984).

directly applied to an $m = 1$ perturbation, and used the appropriately corrected windup rate, with the radial gradient of $\dot{\Omega}$ replacing gradient of μ for vertical and gradient of $\dot{\omega}$ instead of gradient of κ for radial wavelength evolution. Clearly, even for this quite viscous case ($\epsilon_n = 0.50$, $R = 2 \text{ m}$), the expected damping is negligible because of the much longer wavelength of the wave pattern.¹⁰

6.3. Ring particle properties and initial perturbation amplitudes

The systematic decrease in mode amplitudes seen between the 2008 RSS and the 2017 VIMS observations suggests that substantial mode damping has occurred on a decadal timescale. We now compare the observed damping behavior to theoretical models of the wavelength-dependent damping rates to estimate the mode amplitudes A_z^0 and A_z^2 at the time of their formation, and their sensitivity to the assumed elasticity and viscosity of the rings. Fig. 37 shows the vertical $m = 0$ amplitude damping factor as a function of radius for four N-body simulations, in the same format as Fig. 36. In each panel, the observed average $m = 0$ vertical mode amplitude A_z^0 from the late RSS observations, normalized to match the amplitude damping factor for R75.5, is shown as a horizontal bar spanning the radial range of each of the eight defined regions in Fig. 1. In the upper left panel, $\epsilon_n = 0.5$ and $R = 1 \text{ m}$. The next two panels show the corresponding results for less elastic particles, with $\epsilon_n = 0.3$ (upper right) and $\epsilon_n = 0.1$ (lower left). In these successive runs, v_z decreases, damping is reduced, and the amplitude damping factor in R75.5 systematically increases (i.e., the mode amplitude after 33.8 years is closer to the initial amplitude as v_z and ϵ_n are decreased). For comparison, we include a final example with $\epsilon_n = 0.30$ and particle radius $R = 2 \text{ m}$, showing substantial damping. The simulations in Fig. 36 did not include self-gravity. However, based on Fig. 35, the upper-left plot for $R = 1 \text{ m}$ and $\epsilon_n = 0.50$ would be essentially unchanged if self-gravity were included, and that of the upper-right plot with $\epsilon_n = 0.3$ with no self-gravity would be very similar to the case of $\epsilon_n = 0.1$ with self-gravity.

Qualitatively, the most elastic simulation in Fig. 37, with $\epsilon_n = 0.5$, comes closest to matching the radial variations in the scaled regionally averaged amplitudes A_z^0 obtained from 2010 RSS observations. The damping factor in R75.5 is ~ 0.2 , and the observed scaled amplitudes (the horizontal bars) for most regions are in reasonable agreement with the blue curve showing the amplitude damping factor computed using the observed optical depth profile plotted below. The agreement is less satisfactory for $\epsilon_n = 0.3$, while the inelastic $\epsilon_n = 0.1$ simulation gives the poorest match: the predicted amplitude damping factors in high optical depth regions such as R74.9, R76.9, and R77.3 fall above the observations, while they fall below the observations for the low optical depth R76.6.

To refine this assessment, we now compare the observed time variability of A_z^0 and A_z^2 with the predicted trends from Eq. (95). Fig. 38 shows the observed amplitudes in region R75.5 for the three separate time periods corresponding to the 2008 and 2010 RSS events and the 2017 VIMS events for $\tan B_{\text{eff}} = 0.4$, taking account of the observed dependence of the inferred mode amplitude on $\tan B_{\text{eff}}$ for $\tan B_{\text{eff}} \leq 0.5$ shown in Fig. 28, along with the theoretical damping curves computed from the model parameters assumed for an expanded suite of models such as those shown in Fig. 37. All observed and model amplitudes have been normalized to unity at the average date of the VIMS observations in 2017. These are best matched by the $\epsilon_n = 0.5$ N-body results,

¹⁰ The results would be quite different, however, for the scenario in which the C ring ripples resulted from a closely-spaced pair of initial $m = 1$ vertical disturbances several centuries ago (Marouf et al., 2011), owing to the cubic dependence on time in the exponent of the expression for the damping factor in Eq. (95). In this case, for R75.5, the computed vertical damping factor is a vanishingly small $\sim 10^{-45}$, indicating that no evidence would remain of the initial disturbance during the *Cassini* era, independent of the initial amplitudes or the details of the assumed particle properties.

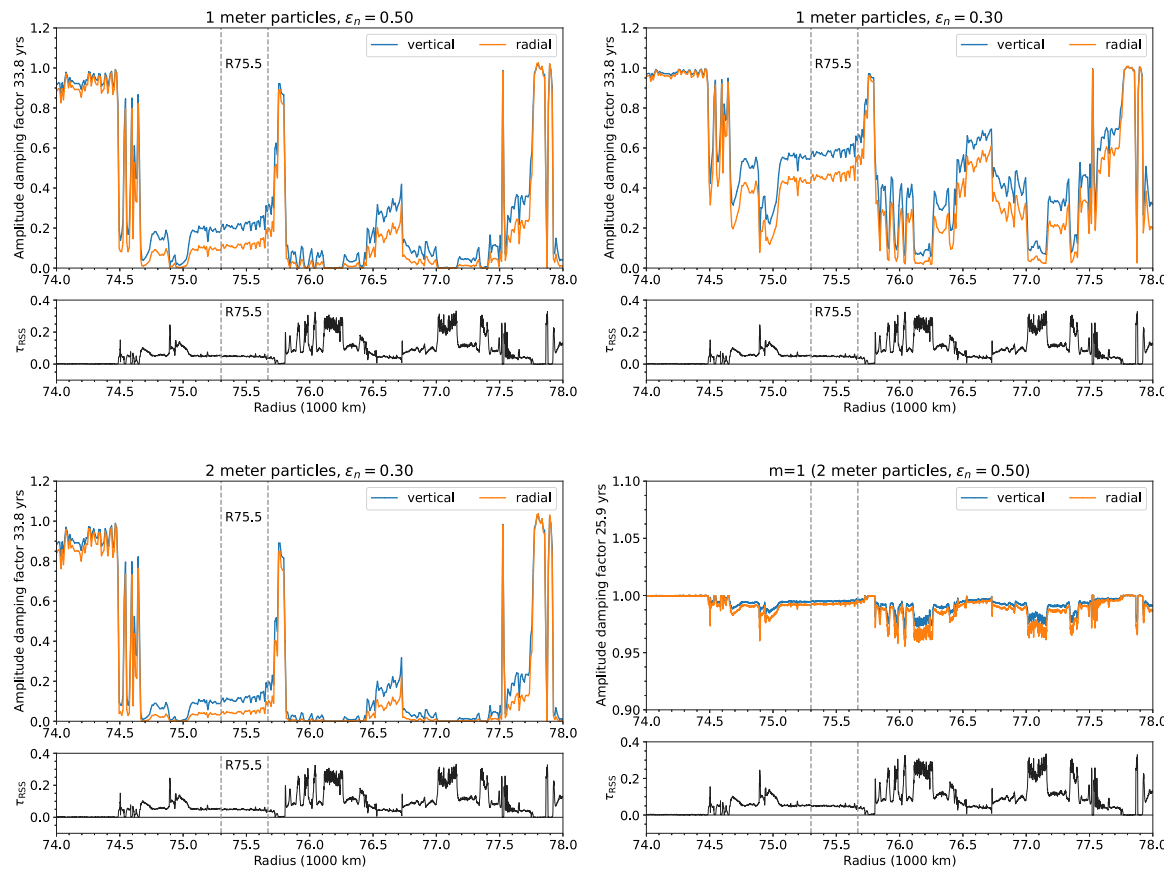


Fig. 36. Amplitude damping factors after 33.8 years for a variety of assumed ring particle properties, using the approximation that v_z and v_r are directly proportional to optical depth τ_n . Upper left: The non-dimensional values of v_z and v_r are scaled to physical units assuming a particle size $R = 1$ m and Ω scaled appropriately with the orbital radius. The estimated viscosities are derived from the numerical simulations for $\epsilon_n = 0.50$. For comparison, the RSS_133E_K25 optical depth profile is shown on the same radial scale ($\tau_{RSS} = 2\pi$ is assumed). Upper right: same except using viscosities for $\epsilon_n = 0.3$. Lower left: $\epsilon_n = 0.3$ but with 2 m particles. Lower right: damping of $m = 1$ waves after 25.9 years, using the viscosities for $\epsilon_n = 0.5$ with $R = 2$ m particles. (Note the change in vertical scale.)

consistent with our qualitative inference from examination of the trends in Fig. 37. For $\epsilon_n \leq 0.4$, the predicted damping between 2008 and 2017 is much smaller than observed, while for the larger particle case ($\epsilon_n = 0.3$, $R = 2$ m) the predicted damping is far too large. These results suggest that the initial amplitudes of the A_z^0 and A_z^2 modes at the time of formation were ~ 4 to 7 times larger than the observed 2017 VIMS values. Assuming $R = 1$ m and $\epsilon_n = 0.5$, the corresponding viscosities from the N-body simulations are $v_z = 1.6 \text{ cm}^2 \text{ s}^{-1}$ and $v_r = 2.2 \text{ cm}^2 \text{ s}^{-1}$, for R75.5. For comparison, Afigbo et al. (2025) found $v_r \simeq 3 - 20 \text{ cm}^2 \text{ s}^{-1}$ from an analysis of density waves in the inner C ring between 74,500–77,300 km.

7. Considerations for the impact formation mechanism

We have shown that the $m = 0$ and $m = 2$ vertical modes responsible for the $\lambda \sim 1$ km ripple structure evident in Cassini occultation profiles of the inner C ring originated at nearly the same time (within a few days of each other at most), and are likely to have had a common origin with the longer-wavelength ($\lambda \sim 30$ km) vertical corrugations visible in Cassini images and attributed to an impact swarm in 1983.7 (Hedman et al., 2011). Similarly, the ripples are vertical corrugations resulting from the windup of $m = 0$ and $m = 2$ vertical modes with slightly different pattern speeds, producing prominent beat patterns in wavepackets observed in the low-optical depth inner C ring. One may think of the $m = 0, 1$, and 2 vertical modes conceptually as Fourier components of the original vertical distortion of the ring plane by an impact swarm, with the relative initial amplitudes of the modes implied by our analysis providing constraints on the details of the formation mechanism. We

find no signatures for $m = 3$ vertical modes in the occultation data, but the predicted wavelength ($\lambda \sim 0.5$ km) is below the resolution limit of many of the data sets. Significantly, no counterpart $\lambda \sim 1$ km radial modes with $m = 0$ or $m = 2$ have been found in the occultation observations, with an estimated upper limit in amplitude of a few m. This may reflect a relative inefficiency in the production of radial modes for the actual geometry of the impact. Supporting this possibility, Hedman et al. (2015) found from an analysis of D ring observations that vertical motions induced by the 1983.7 event were 2.3 ± 0.5 times larger than the corresponding in-plane motions. On the other hand, we have shown from N-body simulations that the radial viscosity is larger than the vertical viscosity ($v_r \simeq 1.4v_z$). For elastic collisions (see Fig. 36, $\epsilon_n = 0.5$), the observed 2017 amplitudes for $m \neq 1$ vertical modes are $\sim 20\%$ of the initial values, whereas the surviving radial amplitudes are only half of that. Thus, it is possible that any initial radial disturbances have been damped below the level of detectability in the occultation data.

When comparing observed mode amplitudes with predictions from impact swarm models, recall that most of our amplitude estimates result from power spectrum analysis of regions more than 100 km in radial extent, and that even taking into account the radial dependence of the mode windup rate, the phase coherence of $\lambda \sim 1$ km waves across the region is imperfect. Consequently, these average amplitudes are likely to be underestimates of the actual local vertical excursions. As we noted above, such local estimates from wavepacket fits are up to a factor of two or more larger than the regional averages. Under the assumption that the initial $m = 0$ and $m = 2$ vertical amplitudes were higher by a factor of $\sim 4 - 7$ than in 2017, the wavepacket fits shown in

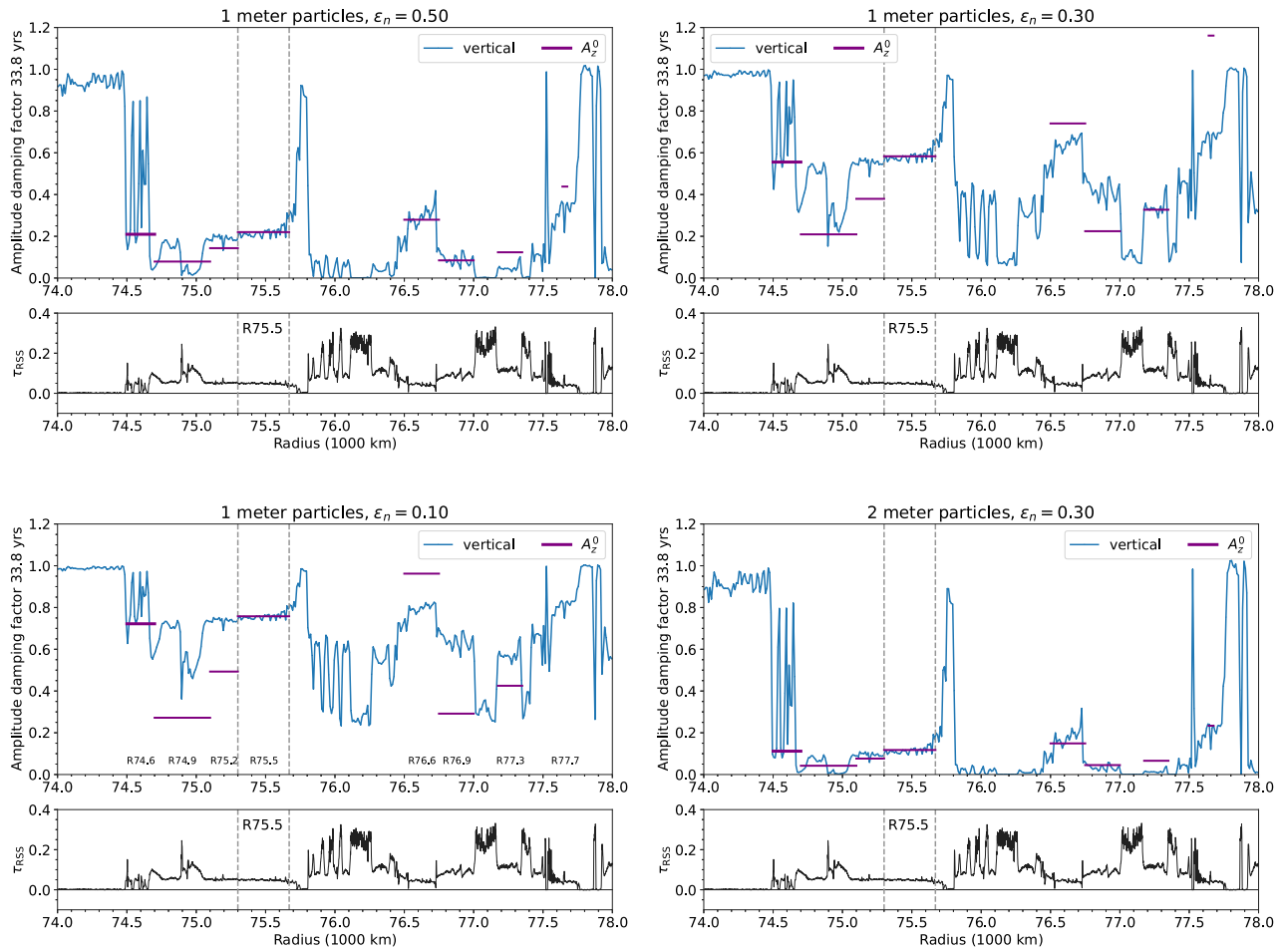


Fig. 37. Amplitude damping factors for an $m = 0$ vertical mode from N-body simulations, with $\epsilon_n = 0.5$ (upper left), $\epsilon_n = 0.3$ (upper right), and $\epsilon_n = 0.1$ (lower left, with radial ranges labeled), all assuming a particle size $R = 1$ m. For comparison, $\epsilon_n = 0.3$ and $R = 2$ m in the simulation at lower right. In each panel, the observed average $m = 0$ vertical mode amplitude A_z^0 from the 2010 RSS observations, normalized to match the amplitude damping factor for R75.5, is shown as a horizontal bar spanning the radial range of each of the eight regions defined in Fig. 1. (For interpretation of the references to color in this figure legend, the reader is referred to the web version of this article.)

Fig. 30 imply typical initial amplitudes of the eventual ripple structure of 10–30 m, and possibly as large as 100 m in the outer regions of R77.7.

From direct inversion of a sample wavepacket (Fig. 14), we showed that the vertical structure of the ring in region R77.7 includes both the short-wavelength corrugations and a $\lambda \sim 25 - 30$ km periodic signature of amplitude $A_z \sim 75$ m, a factor of several larger than the average $m = 1$ amplitude for this region found by Hedman et al. (2011). However, all of these estimates are predicated on a simple model for the variation in predicted wave optical depth with viewing geometry that appears to be contradicted by the observations shown in Fig. 28, suggesting that we may be missing something fundamental in our understanding of ring vertical structure. Our estimates of the relative mode amplitudes for a given $\tan B_{\text{eff}}$ are probably more reliable than the amplitudes themselves.

Finally, we note that $m = 0$ and $m = 2$ perturbations on the ring will freely oscillate on timescales comparable to an orbit period (~ 8 h), and producing such a global pattern with an impact swarm may be impeded if the impacting particles take too long to pass through the rings.

8. Conclusions

Our principal conclusions are as follows:

- Short-wavelength ($\lambda \sim 1$ km) ripple structure seen in low-inclination Cassini RSS, VIMS, and UVIS observations of the inner

C ring (74,500–77,765 km) is associated with vertical corrugations produced by simultaneous $m = 0$ and $m = 2$ vertical modes with slightly different pattern speeds, resulting in a characteristic beating pattern in the optical depth profiles. The pattern speeds are consistent with these modes and not others when looking at observations at different times (see Figs. 8 and 9), and the amplitudes of the ripples in the optical depth profile weaken with higher ring opening angle, as expected for vertical modes, but not radial modes. As shown in Fig. 20, only $m = 0$ and $m = 2$ modes are consistent with the observed ripple wavelengths and a date near 1983, consistent with Hedman et al. (2011). Finally, when correcting for the effects of ring self-gravity, only this combination of modes results in similar impact dates for both modes, as illustrated in Fig. 22.

- The hypothesis that the observed disturbance resulted from two separate impacts with the rings several centuries ago is ruled out by the observed radial dependence of the component waves, the absence of similar C ring structure in the Voyager RSS occultation observations in 1980, and numerical simulations showing that the putative waves would have been completely damped by the time of the Cassini observations. (See Figs. 25 and 26.)
- From fits to the wavenumbers $k_z^2(t)$ and $k_z^0(t)$ of the two modes, and from power spectral analysis of the regional variation of wavenumber over time and orbital radius, we infer an impact date $t_i = \text{UTC } 1983 \text{ Sep } 19.25 \pm 5.5 \text{ d}$, taking into account a plausibly small contribution of ring self-gravity to the windup rates of the

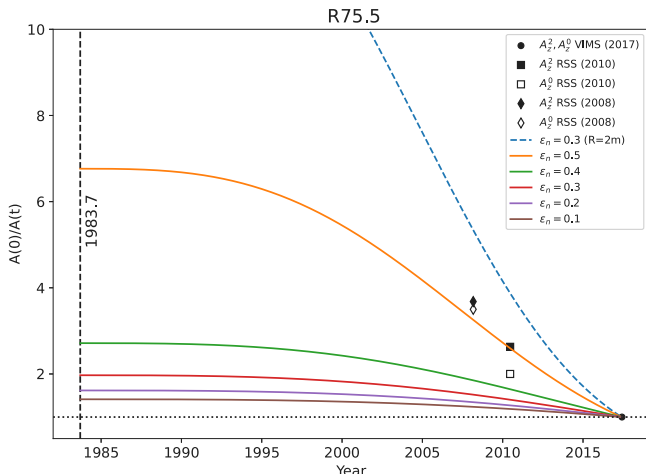


Fig. 38. Predicted time dependence of mode amplitudes since the assumed impact date 1983.7, for a suite of assumed ϵ_n , particle radius R , and the corresponding viscosities v_z from N-body simulations (see Fig. 32), compared to the observed amplitudes A_z^0 and A_z^2 obtained from power spectral analysis of early RSS (2008), late RSS (2010), and VIMS (2017) observations for region R75.5. The particle radius is $R = 1$ m for all cases except for the $\epsilon_n = 0.3$, $R = 2$ m model plotted as a dashed line. All observed and model amplitudes have been normalized to unity at the average date of the VIMS observations in 2017. The observed RSS observed amplitudes A_z^0 and A_z^2 are ~4 times larger than the 2017 VIMS amplitudes for 2008, and ~2–3 times larger for 2010. These are best matched by the $\epsilon_n = 0.5$ N-body results (orange curve) and imply that the initial amplitudes of the A_z^0 and A_z^2 modes at the time of formation were ~4 to 7 times larger than the observed values in 2017. For $R = 1$ m and $\epsilon_n = 0.5$, the corresponding viscosities from the N-body simulations are $v_z = 1.6 \text{ cm}^2 \text{ s}^{-1}$ and $v_r = 2.2 \text{ cm}^2 \text{ s}^{-1}$. (For interpretation of the references to color in this figure legend, the reader is referred to the web version of this article.)

corrugations. For comparison, Hedman et al. (2011) found $t_i = \text{UTC } 1983 \text{ Sep } 20 \pm 40 \text{ d}$ from analysis of the $m = 0$ vertical mode seen in Cassini images. (See Figs. 21–23.)

- No convincing signatures for radial modes with $m = 0$ or $m = 2$, or for vertical modes with $m \geq 3$, are detectable in the occultation data. Quasiperiodic $m = 1$ structure with $\lambda \sim 25\text{--}35 \text{ km}$ is visible in the occultation profiles and power spectra that may also originate from the 1983 impact, although the phase coherence in the optical depth profiles is less convincing than was found by Hedman et al. (2011) in their analysis of Cassini ISS images. Direct inversion of wavepackets to derive the vertical profile of the ring shows evidence of $\lambda \sim 30 \text{ km}$ structure with vertical amplitude A_z of order 75 m. (See Fig. 14.)
- The measured amplitudes A_z^2 and A_z^0 (1–10 m) have comparable values at any given radius, and are anti-correlated with the ring optical depth. (See Figs. 27 and 30.)
- We detect a significant decrease in the amplitudes of both modes over the time interval 2008–2017 of their detectability in the Cassini occultation data. (See Figs. 28 and 38.)
- N-body ring particle collisional simulations provide constraints on the viscosity and coefficient of restitution ϵ_n that are compatible with the observed radial trend of the A_z^2 and A_z^0 mode amplitudes and their damping over time. Damping of radial waves is faster than that of vertical, with the ratio of radial to vertical ring particle viscosities being $v_r/v_z \sim 1.4$ for a wide range of simulation conditions. (See Figs. 32–35.)
- The $m = 1$ corrugation amplitude variations with ring radius and optical depth observed by Hedman et al. (2011) are unlikely to have suffered much damping since their formation, owing to their long wavelength. The initial amplitudes of the $m = 0$ and $m = 2$ vertical modes are estimated to be ~4 to 7 times their present

values at a radius of 75,500 km. (See Figs. 37 and 38.)

- The observed linear dependence of the inferred vertical mode amplitudes A_z^2 and A_z^0 on $\tan B_{\text{eff}}$ suggests that our adopted model for the vertical structure of the rings and the effect of viewing geometry (based on Gresh et al., 1986 and Hedman et al., 2011, 2015) is oversimplified. Our estimates of the relative mode amplitudes for a given $\tan B_{\text{eff}}$ are probably more reliable than the amplitudes themselves. (See Fig. 28.)
- No short-wavelength ripple structure is found beyond a radius of 77,765 km, where the higher average optical depth limits the detectability of the low vertical amplitudes predicted for this region, based on the $m = 1$ observations (Hedman et al., 2011).
- These results provide important initial conditions for future detailed dynamical models of the 1983 impact with Saturn's rings that attempt to account for the origin and evolution of the newly-identified $m = 0$ and $m = 2$ vertical modes, the longer-wavelength $m = 1$ corrugations, and the absence of $m = 0$ and $m = 2$ radial modes and of vertical modes with $m \geq 3$. The creation of a coherent $m = 0$ and $m = 2$ vertical perturbations with free periods of ~8 h by a swarm of impacting particles might imply that the initial disturbance was quite short.

CRediT authorship contribution statement

Richard G. French: Writing – original draft, Visualization, Validation, Supervision, Software, Project administration, Methodology, Investigation, Formal analysis, Data curation, Conceptualization. **Philip D. Nicholson:** Writing – original draft, Methodology, Investigation, Funding acquisition, Conceptualization. **Matthew M. Hedman:** Writing – review & editing, Methodology, Investigation, Data curation, Conceptualization. **Heikki Salo:** Writing – original draft, Methodology, Investigation, Formal analysis. **Essam A. Marouf:** Data curation, Conceptualization. **Colleen A. McGhee-French:** Data curation. **Nicole Rappaport:** Data curation. **Joshua Colwell:** Data curation. **Richard Jerousek:** Writing – review & editing, Data curation. **Victor M. Afibgo:** Investigation. **Sophia Flury:** Software, Methodology, Data curation. **Jolene Fong:** Software, Data curation. **Ryan Maguire:** Software, Formal analysis, Data curation. **Glen Steranka:** Software, Data curation. **Matthew S. Tiscareno:** Writing – review & editing.

Declaration of competing interest

The authors declare that they have no known competing financial interests or personal relationships that could have appeared to influence the work reported in this paper.

Acknowledgments

This work was supported in part by NASA CDAP, USA grant 80NSSC23K0217. We especially thank an anonymous reviewer for detailed comments and many helpful suggestions, which led us to clarify and justify several key results and assumptions. We are also grateful to the Cassini RSS, VIMS, and UVIS science and engineering teams for planning, observing, and reducing the occultation observations that are the basis of this work.

Appendix A. Corrections for ring self-gravity

Here we derive the corrections to the expressions for $k_r^m(a, t)$ and $k_z^m(a, t)$ for the effect of ring self-gravity, Eqs. (48)–(51), following the prescription of Hedman et al. (2011, 2015) for $m = 1$ perturbations in images of the C and D rings. We use the density wave and bending wave dispersion relations to estimate corrections to Ω_{pr} and Ω_{pz} , and thence to k_r^m and k_z^m for ring self-gravity. The dispersion relation for

free radial waves is given by Shu (1984), Eq. (37):

$$(\omega_r - mn)^2 = \kappa^2 - 2\pi G\sigma_0 |k_r^m|. \quad (\text{A.1})$$

Solving for ω_r , we have

$$\omega_r = m\Omega_{Pr} = mn \pm \kappa [1 - 2\pi G\sigma_0 |k_r^m|/\kappa^2]^{1/2} \quad (\text{A.2})$$

If $2\pi G\sigma_0 |k_r^m| \ll \kappa^2$, and we take the minus sign to match Eq. (2) for the limit where $\sigma_0 \rightarrow 0$, we obtain

$$\begin{aligned} m\Omega_{Pr} &\simeq mn - \kappa [1 - \pi G\sigma_0 |k_r^m|/\kappa^2] \\ &\simeq mn - \kappa + \pi G\sigma_0 |k_r^m|/\kappa \\ &\simeq m\Omega_{Pr}^0 + \pi G\sigma_0 |k_r^m|/\kappa, \end{aligned} \quad (\text{A.3})$$

where Ω_{Pr}^0 is the free (*i.e.*, unforced) pattern speed. Using Eq. (26) as the 0th-order approximation for k_r^m ,

$$m\Omega_{Pr} \simeq m\Omega_{Pr}^0 + \frac{\pi G\sigma_0 m}{\kappa} \left| \frac{\partial \Omega_{Pr}^0}{\partial a} \right| \Delta t. \quad (\text{A.4})$$

Ω_{Pr} is now time-dependent due to the windup of the corrugation, and from Eq. (S14) of Hedman et al. (2011), Eq. (26) is replaced by

$$\begin{aligned} k_r^m &= -m \frac{\partial}{\partial a} \left(\int_{t_i}^t \Omega_{Pr} dt \right) \\ &= -m (\partial \Omega_{Pr}^0 / \partial a) \Delta t - \frac{m\pi G}{2} \frac{\partial}{\partial a} \left[\frac{\sigma_0}{\kappa} \left| \partial \Omega_{Pr}^0 / \partial a \right| \right] \Delta t^2 \\ &= k_{z0}^m \left\{ 1 - \frac{\pi G}{2} \frac{\partial(\sigma_0/\kappa)}{\partial a} \Delta t - \frac{\pi G\sigma_0}{2\kappa} \frac{\partial |\partial \Omega_{Pr}^0 / \partial a|}{\partial a} \frac{\Delta t}{|\partial \Omega_{Pr}^0 / \partial a|} \right\}. \end{aligned} \quad (\text{A.5})$$

Expanding the differentials,

$$k_r^m = k_{z0}^m \left[1 + \frac{\pi G\sigma_0}{2\kappa^2} \frac{\partial \kappa}{\partial a} \Delta t - \frac{\pi G}{2\kappa} \frac{\partial \sigma_0}{\partial a} \Delta t + \frac{\pi G\sigma_0}{2\kappa} \frac{|\partial^2 \Omega_{Pr}^0 / \partial a^2|}{|\partial \Omega_{Pr}^0 / \partial a|} \Delta t \right]. \quad (\text{A.6})$$

For $m \neq 1$ or 0,

$$\Omega_{Pr} \sim \frac{m-1}{m} n(a) \propto a^{-3/2}, \quad (\text{A.7})$$

$$\partial \Omega_{Pr}^0 / \partial a \simeq -\frac{3}{2} \Omega_{Pr} / a \propto a^{-5/2}, \quad (\text{A.8})$$

and

$$\partial^2 \Omega_{Pr}^0 / \partial a^2 \simeq -\frac{5}{2} (\partial \Omega_{Pr} / \partial a) / a \quad (\text{A.9})$$

$$\simeq \frac{15}{4} \Omega_{Pr} / a^2 \propto a^{-7/2}. \quad (\text{A.10})$$

Therefore,

$$k_r^m = k_{z0}^m \left[1 - \frac{3\pi G\sigma_0}{4\kappa a} \Delta t - \frac{\pi G}{2\kappa} \frac{\partial \sigma_0}{\partial a} \Delta t + \frac{5\pi G\sigma_0}{4\kappa a} \Delta t \right] \quad (\text{A.11})$$

or

$$k_r^m(a) = k_{z0}^m(a) \left[1 + \frac{\pi G}{2\kappa} \left(\frac{\sigma_0}{a} - \frac{\partial \sigma_0}{\partial a} \right) \Delta t \right]. \quad (\text{A.12})$$

The dispersion relation for free vertical waves is given by Shu (1984), Eq. (84):

$$(\omega_z - mn)^2 = \mu^2 + 2\pi G\sigma_0 |k_z^m|, \quad (\text{A.13})$$

where μ is the vertical epicyclic frequency. The development is the same as for radial waves except for the sign of the second term on the right hand side, with the result

$$k_z^m(a) = k_{z0}^m(a) \left[1 - \frac{\pi G}{2\mu} \left(\frac{\sigma_0}{a} - \frac{\partial \sigma_0}{\partial a} \right) \Delta t \right]. \quad (\text{A.14})$$

For radial perturbations with $m = 0$, we have the dispersion relation

$$(\omega_r^0)^2 = \kappa^2 - 2\pi G\sigma_0 |k_r^0|, \quad (\text{A.15})$$

or

$$\omega_r^0 = \pm \kappa [1 - 2\pi G\sigma_0 |k_r^0|/\kappa^2]^{1/2}, \quad (\text{A.16})$$

but here we take the ‘+’ sign to match Eq. (8) when $\sigma_0 \rightarrow 0$:

$$\begin{aligned} \omega_r^0 &\simeq \kappa - \pi G\sigma_0 |k_r^0|/\kappa \\ &= \omega_{r0}^0 - \pi G\sigma_0 |k_r^0|/\kappa. \end{aligned} \quad (\text{A.17})$$

This is identical to the expression for $m\Omega_{Pr}$ in Eq. (A.3) except for the sign of the correction. For $|k_r^0|$ we use the 0th-order approximation in Eq. (36)

$$|k_r^0| = |\partial \omega_r^0 / \partial a| \Delta t, \quad (\text{A.18})$$

so

$$\omega_r^0 \simeq \omega_{r0}^0 - \frac{\pi G\sigma_0}{\kappa} |\partial \omega_r^0 / \partial a| \Delta t. \quad (\text{A.19})$$

The modified version of k_r^0 that accounts for the ring’s self-gravity is

$$\begin{aligned} k_r^0 &= -\frac{\partial}{\partial a} \left(\int_{t_i}^t \omega_r^0 dt \right) \\ &= -(\partial \omega_r^0 / \partial a) \Delta t + \frac{\pi G}{2} \frac{\partial}{\partial a} \left[\frac{\sigma_0}{\kappa} \left| \partial \omega_r^0 / \partial a \right| \right] \Delta t^2 \\ &= k_{r0}^0 \left\{ 1 + \frac{\pi G}{2} \frac{\partial(\sigma_0/\kappa)}{\partial a} \Delta t + \frac{\pi G\sigma_0}{2\kappa} \frac{\partial |\partial \omega_r^0 / \partial a|}{\partial a} \Delta t / |\partial \omega_r^0 / \partial a| \right\}. \end{aligned} \quad (\text{A.20})$$

As above,

$$\omega_r^0 \sim \kappa \propto a^{-3/2}, \quad (\text{A.21})$$

$$\partial \omega_r^0 / \partial a \simeq -\frac{3}{2} \kappa / a \propto a^{-5/2}, \quad (\text{A.22})$$

and

$$\begin{aligned} \partial^2 \omega_r^0 / \partial a^2 &\simeq -\frac{5}{2} (\partial \omega_r^0 / \partial a) / a \\ &\simeq \frac{15}{4} \kappa / a^2 \propto a^{-7/2}. \end{aligned} \quad (\text{A.23})$$

Thus, we for $m = 0$ the radial self-gravity correction is the same as for $m > 1$ but of the opposite sign:

$$k_r^0(a) = k_{r0}^0(a) \left[1 - \frac{\pi G}{2\kappa} \left(\frac{\sigma_0}{a} - \frac{\partial \sigma_0}{\partial a} \right) \Delta t \right]. \quad (\text{A.24})$$

For $m = 0$ bending waves, the dispersion relation is

$$(\omega_z^0)^2 = \mu^2 + 2\pi G\sigma_0 |k_z^0|, \quad (\text{A.25})$$

and so

$$\omega_z^0 = \pm(\mu^2 + 2\pi G\sigma_0 |k_z^0|)^{1/2}. \quad (\text{A.26})$$

Taking the ‘+’ sign so that $\omega_z \rightarrow v$ as $\sigma_0 \rightarrow 0$ (Eq. (9)), we have

$$\omega_z^0 = \mu [1 + 2\pi G\sigma_0 |k_z^0| / \mu^2]^{1/2}. \quad (\text{A.27})$$

This is of the same form as Eq. (50) except for the sign of the second term, and by symmetry the vertical self-gravity correction is therefore

$$k_z^0(a) = k_{z0}^0(a) \left[1 + \frac{\pi G}{2\mu} \left(\frac{\sigma_0}{a} - \frac{\partial \sigma_0}{\partial a} \right) \Delta t \right]. \quad (\text{A.28})$$

Appendix B. Explicit wavenumber formulae

It is sometimes convenient to have explicit, if only approximate, expressions for the radial wavenumbers k_r^m and k_z^m that appear in many of the equations in this paper, as well as approximate numerical values for their wavelengths and dimensionless ratios k_z^m/k_r^m . We begin

with Eqs. (26), (27), (31), (32), (36), and (37), based on derivations by Hedman et al. (2011, 2015), for the time-dependent radial wavenumbers of the radial (k_r^m) and vertical (k_z^m) perturbations for different values of m , the azimuthal wavenumber of the perturbations (i.e., the number of spiral arms in the pattern). These in turn depend on radial derivatives of the frequencies for the various modes, as specified in Eqs. (2), (5), (8), and (9), as well as the time interval between the initial impact and the observation, $\Delta t = t - t_0$. We first treat the special cases of $m = 0$ and $m = 1$, and then deal with the more general expressions for other values of m .

B.1. $m = 0$

For $m = 0$, corresponding to an axisymmetric ripple pattern, there is no pattern speed, per se, but the temporal frequencies of free radial (κ) and vertical (μ) oscillations in the rings ω_r^0 and ω_z^0 are given by Eqs. (8) and (9):

$$\begin{aligned}\omega_r^0(a) &= \kappa = n - \dot{\varpi}_{\text{sec}} \\ \omega_z^0(a) &= \mu = n - \dot{\Omega}_{\text{sec}},\end{aligned}\quad (\text{B.1})$$

where n is the mean motion and $\dot{\varpi}_{\text{sec}}$ and $\dot{\Omega}_{\text{sec}}$ are the apsidal and nodal precession rates of a ring particle orbit at semimajor axis a . The radial wavenumber k_r^0 is given by Eq. (36):

$$\begin{aligned}k_r^0(a) &= \left| \frac{\partial \omega_r^0}{\partial a} \right| \Delta t \\ &= \left| \frac{\partial n}{\partial a} - \frac{\partial \dot{\varpi}}{\partial a} \right| \Delta t \\ &\simeq \left| -\frac{3n}{2a} + \frac{7\dot{\varpi}}{2a} \right| \Delta t \\ &= \frac{3n\Delta t}{2a} \left[1 - \frac{7\dot{\varpi}}{3n} \right] \\ &\simeq \frac{3n\Delta t}{2a} \left[1 - \frac{7}{2} J_2(R_p/a)^2 \right],\end{aligned}\quad (\text{B.2})$$

where we have used the first-order approximation for $\dot{\varpi}_{\text{sec}}$ in Eq. (3). The corresponding radial wavenumber for vertical perturbations k_z^0 is given by Eq. (37):

$$\begin{aligned}k_z^0(a) &= \left| \frac{\partial \omega_z^0}{\partial a} \right| \Delta t \\ &= \left| \frac{\partial n}{\partial a} - \frac{\partial \dot{\Omega}}{\partial a} \right| \Delta t \\ &\simeq \left| -\frac{3n}{2a} + \frac{7\dot{\Omega}}{2a} \right| \Delta t \\ &= \frac{3n\Delta t}{2a} \left[1 - \frac{7\dot{\Omega}}{3n} \right] \\ &\simeq \frac{3n\Delta t}{2a} \left[1 + \frac{7}{2} J_2(R_p/a)^2 \right],\end{aligned}\quad (\text{B.3})$$

where we have used the first-order approximation for $\dot{\Omega}_{\text{sec}}$ in Eq. (7).¹¹

From the above expressions we have the useful but simple result, independent of Δt , that

$$k_z^0/k_r^0 \simeq 1 + 7J_2(R_p/a)^2 + O(J_2^2(R_p/a)^4) \simeq 1.071,\quad (\text{B.4})$$

where we evaluate the J_2 scale factor R_p/a at $a = 76,600$ km, mid-way between the regions R75.5 and R77.5.

B.2. $m = 1$

For $m = 1$ the general expressions for the pattern speed, Eqs. (2) and (5) apply, but the leading terms in Ω_{Pr} and Ω_{Pz} involving the factor

¹¹ We note that the above expressions are not quite correct to $O(J_2)$, as they neglect the J_2 correction to the mean motion n , but this cancels out in the ratios we discuss below, and leads to only small corrections ($\sim 1\%$) in the absolute values of k_r^0 and k_z^0 .

($m - 1$) are zero, leaving the simpler expressions

$$\Omega_{Pr}^1(a) = \dot{\varpi}_{\text{sec}}(a)\quad (\text{B.5})$$

$$\Omega_{Pz}^1(a) = \dot{\Omega}_{\text{sec}}(a).\quad (\text{B.6})$$

Substituting these into Eqs. (26) and (27), we find that

$$\begin{aligned}k_r^1(a) &= \left| \frac{\partial \Omega_{Pr}^1}{\partial a} \right| \Delta t \\ &= \left| \frac{\partial \dot{\varpi}}{\partial a} \right| \Delta t \\ &\simeq \left| -\frac{7\dot{\varpi}}{2a} \right| \Delta t \\ &= \frac{7n\Delta t}{2a} \left(\frac{\dot{\varpi}}{n} \right) \\ &\simeq \frac{21n\Delta t}{4a} J_2(R_p/a)^2,\end{aligned}\quad (\text{B.7})$$

and

$$\begin{aligned}k_z^1(a) &= \left| \frac{\partial \Omega_{Pz}^1}{\partial a} \right| \Delta t \\ &= \left| \frac{\partial \dot{\Omega}}{\partial a} \right| \Delta t \\ &\simeq \left| -\frac{7\dot{\Omega}}{2a} \right| \Delta t \\ &\simeq \frac{21n\Delta t}{4a} J_2(R_p/a)^2,\end{aligned}\quad (\text{B.8})$$

since, to first order in J_2 , $\dot{\Omega}_{\text{sec}} = -\dot{\varpi}_{\text{sec}}$. So, to this order we find that $k_z^1 = k_r^1$. If instead we use the full Eqs. (3) and (6) to evaluate $\dot{\varpi}_{\text{sec}}$ and $\dot{\Omega}_{\text{sec}}$, then the two rates differ by a term of $O(J_2^2(R_p/a)^4)$ and it is straightforward to show that

$$k_z^1/k_r^1 \simeq 1 - \frac{33}{14} J_2(R_p/a)^2 \simeq 0.976\quad (\text{B.9})$$

at $a = 76,600$ km.¹²

Note that the radial wavenumbers for $m = 1$ are both smaller than those for $m = 0$ by a factor of $\sim \frac{7}{2} J_2(R_p/a)^2 \simeq 0.035$ at $a = 76,600$ km.

B.3. $m \neq 0$ and $m \neq 1$

For other values of m we again proceed based on Eqs. (26) and (27), using the full expressions for Ω_{Pr}^m and Ω_{Pz}^m in Eqs. (2) and (5). Otherwise, the derivation is very similar to that for Eqs. (B.2) and (B.3) above. For radial perturbations, we have

$$\begin{aligned}k_r^m(a) &= \left| \frac{\partial \Omega_{Pr}^m}{\partial a} \right| \Delta t \\ &= \left| (m-1) \frac{\partial n}{\partial a} + \frac{\partial \dot{\varpi}}{\partial a} \right| \Delta t \\ &\simeq \left| -(m-1) \frac{3n}{2a} - \frac{7\dot{\varpi}}{2a} \right| \Delta t \\ &= \frac{3n\Delta t}{2a} \left| m-1 + \frac{7\dot{\varpi}}{3n} \right| \\ &\simeq \frac{3n\Delta t}{2a} \left| m-1 + \frac{7}{2} J_2(R_p/a)^2 \right|.\end{aligned}\quad (\text{B.10})$$

¹² The J_4 and J_6 terms cancel out of the ratio, as they enter in the same manner into $\dot{\Omega}_{\text{sec}}$ and $\dot{\varpi}_{\text{sec}}$, to leading order.

where we have again used the first-order approximation for $\dot{\varpi}_{\text{sec}}$ in the final line. For vertical perturbations we have

$$\begin{aligned} k_z^m(a) &= \left| \frac{\partial \Omega_{Pz}^m}{\partial a} \right| \Delta t \\ &= \left| (m-1) \frac{\partial n}{\partial a} + \frac{\partial \dot{\Omega}}{\partial a} \right| \Delta t \\ &\simeq \left| -(m-1) \frac{3n}{2a} - \frac{7\dot{\Omega}}{2a} \right| \Delta t \\ &= \frac{3n\Delta t}{2a} \left| m-1 + \frac{7\dot{\Omega}}{3n} \right| \\ &\simeq \frac{3n\Delta t}{2a} \left| m-1 - \frac{7}{2} J_2(R_p/a)^2 \right|. \end{aligned} \quad (\text{B.11})$$

Note that m can be either positive (corresponding to the situation where $\Omega_P < n$, or an inner Lindblad resonance), or negative (corresponding to the situation where $\Omega_P > n$, or an outer Lindblad resonance), leading to different values of k_r^m and k_z^m . In both cases the pattern speed is positive, and approaches the Keplerian mean motion n as $m \rightarrow \infty$.

From the above expressions, we find that the ratio of wavenumbers for vertical and radial perturbations with the same value of m is given approximately by

$$k_z^m/k_r^m \simeq 1 - \frac{7}{m-1} J_2(R_p/a)^2 \simeq 1 - 0.071/(m-1) \quad (\text{B.12})$$

where we again evaluate the factor R_p/a at $a = 76,600$ km.

B.4. Degeneracies between modes with differing azimuthal wavenumbers

There is, however, a near-degeneracy between the values of k_r^m and k_z^m for positive and negative values of m that may be seen from the above expressions. If we set $m = -m'$, then we find that

$$\begin{aligned} k_r^m &= \frac{3n\Delta t}{2a} \left| -m' - 1 + \frac{7\dot{\omega}}{3n} \right| \\ &= \frac{3n\Delta t}{2a} \left| m' + 1 - \frac{7\dot{\omega}}{3n} \right| \\ &\simeq \frac{3n\Delta t}{2a} \left| m' + 1 + \frac{7\dot{\Omega}}{3n} \right| \\ &\simeq \frac{3n\Delta t}{2a} \left| 1 - m + \frac{7\dot{\Omega}}{3n} \right| \\ &= k_z^{2-m} \end{aligned} \quad (\text{B.13})$$

In a similar fashion, it is readily shown that $k_z^m \simeq k_r^{2-m}$. For example, the wavenumbers for vertical perturbations with $m = 2$ are almost the same as those for radial perturbations with $m = 0$, while those for radial perturbations with $m = 2$ are almost the same as those for vertical perturbations with $m = 0$.¹³ Similar degeneracies apply to the pairs of modes with $m = 3$ and -1 , $m = 4$ and -2 , etc.

This inverse relationship between radial and vertical modes can also be seen in the vertical/radial wavenumber ratios, with Eq. (B.12) implying that

$$\begin{aligned} k_r^{2-m}(a)/k_z^{2-m}(a) &\simeq 1 + \frac{7}{1-m} J_2(R_p/a)^2 \\ &= 1 - \frac{7}{m-1} J_2(R_p/a)^2 \\ &\simeq k_z^m(a)/k_r^m(a). \end{aligned} \quad (\text{B.14})$$

Returning to Eqs. (B.10) and (B.11), the dominant term $m-1$ in the expressions for k_r^m and k_z^m means that oscillations with larger values of $|m-1|$ will have higher radial wavenumbers, or shorter radial

¹³ A similar degeneracy between the oscillation frequencies of density waves with $m = 0$ and bending waves with $m = 2$ was identified by Hedman et al. (2019), who noted that such waves are almost indistinguishable unless their phases can be compared at two or more different longitudes. In both this case and in the present situation, the key underlying cause is that the apsidal and nodal precession rates of ring particle orbits are almost equal in magnitude but opposite in sign.

wavelengths.

B.5. Numerical values

All of the wavenumber estimates given above scale as $3n\Delta t/2a$, except for modes with $m = 1$ that scale as $(21n\Delta t/4a) J_2(R_p/a)^2$. We can get a rough idea of the wavenumbers to be expected for the inner C ring and an impact event in 1983 by substituting nominal values of $a = 76,600$ km, $n = 1450^\circ \text{ d}^{-1} = 2.93 \times 10^{-4} \text{ rad s}^{-1}$, $J_2 = 1.63 \times 10^{-2}$ and $\Delta t = 30 \text{ yr} = 9.47 \times 10^8 \text{ s}$. The corresponding mean radial wavelengths $2\pi/\bar{k}$ are 32.7 km for $m = 1$, 1.16 km for $m = 0$ or 2, 0.58 km for $m = -1$ or 3, 0.39 km for $m = -2$ or 4 and 0.29 km for $m = -3$ or 5. The ratios k_z^m/k_r^m (or their inverses) range from 1.071 for $m = 0$ (or 2) to 1.018 for $m = -3$ (or 5). For $m = 1$ $k_z^1/k_r^1 = 0.975$. In practice, perturbation patterns with $|m-1| \geq 3$ (i.e., $m \geq 4$ or $m \leq -2$) are unlikely to be detectable in most of the Cassini RSS and VIMS occultation profiles, which have effective radial resolutions of ~ 250 m, at best.

See Table 5 for a more accurate and extensive set of values, calculated using the full set of gravity coefficients in Table 2 for semimajor axes r_0 given in Table 4.

Data availability

Data will be made available on request.

References

- Afigbo, V.M., Hedman, M.M., Nicholson, P.D., French, R.G., Mankovich, C.R., Jerousek, R.G., Dewberry, J., 2025. Unveiling what makes Saturn ring: Quantifying the amplitudes of Saturn's planetary normal-mode oscillations using Kronoseismology (VII). *JGR: Planets* submitted for publication, under revision.
- Baillié, K., Colwell, J.E., Lissauer, J.J., Esposito, L.W., Sremčević, M., 2011. Waves in Cassini UVIS stellar occultations. 2. The C ring. *Icarus* 216, 292–308. <http://dx.doi.org/10.1016/j.icarus.2011.05.019>.
- Borderies-Rappaport, N., Longaretti, P.-Y., 1994. Test particle motion around an oblate planet. *Icarus* 107, 129–141. <http://dx.doi.org/10.1006/icar.1994.1011>.
- Brouwer, D., Clemence, G.M., 1961. *Methods of Celestial Mechanics*. Academic Press, New York.
- Colwell, J.E., Esposito, L.W., Cooney, J.H., 2018. Particle sizes in Saturn's rings from UVIS stellar occultations 1. Variations with ring region. *Icarus* 300, 150–166. <http://dx.doi.org/10.1016/j.icarus.2017.08.036>.
- Daisaka, H., Tanaka, H., Ida, S., 2001. Viscosity in a dense planetary ring with self-gravitating particles. *Icarus* 154, 296–312. <http://dx.doi.org/10.1006/icar.2001.6716>.
- French, R.G., Bridges, B., Hedman, M.M., Nicholson, P.D., Mankovich, C., McGhee-French, C.A., 2021. Kronoseismology V: A panoply of waves in Saturn's C ring driven by high-order internal planetary oscillations. *Icarus* 370. <http://dx.doi.org/10.1016/j.icarus.2021.114660>.
- French, R.G., McGhee-French, C.A., Nicholson, P.D., Hedman, M.M., 2019. Kronoseismology III: Waves in Saturn's inner C ring. *Icarus* 319, 599–626. <http://dx.doi.org/10.1016/j.icarus.2018.10.013>.
- French, R.G., Nicholson, P.D., 2000. Saturn's rings II. Particle sizes inferred from stellar occultation data. *Icarus* 145, 502–523. <http://dx.doi.org/10.1006/icar.2000.6357>.
- French, R.G., et al., 2017. Noncircular features in Saturn's rings IV: Absolute radius scale and Saturn's pole direction. *Icarus* 290, 14–45. <http://dx.doi.org/10.1016/j.icarus.2017.02.007>.
- Gresh, D.L., Rosen, P.A., Tyler, G.L., Lissauer, J.J., 1986. An analysis of bending waves in Saturn's rings using Voyager radio occultation data. *Icarus* 68, 481–502. [http://dx.doi.org/10.1016/0019-1035\(86\)90052-7](http://dx.doi.org/10.1016/0019-1035(86)90052-7).
- Hämeen-Anttila, K.A., Salo, H., 1993. Generalized theory of impacts in particulate systems. *Earth Moon Planets* 62, 47–84. <http://dx.doi.org/10.1007/BF00612895>.
- Hedman, M.M., Burns, J.A., Evans, M.W., Tiscareno, M.S., Porco, C.C., 2011. Saturn's curiously corrugated C ring. *Science* 332 (708), <http://dx.doi.org/10.1126/science.1202238>.
- Hedman, M.M., Burns, J.A., Showalter, M.R., 2015. Corrugations and eccentric spirals in Saturn's D ring: New insights into what happened at Saturn in 1983. *Icarus* 248, 137–161. <http://dx.doi.org/10.1016/j.icarus.2014.10.021>.
- Hedman, M.M., Nicholson, P.D., El Moutamid, M., Smotherman, S., 2022. Kronoseismology VI: Reading the recent history of Saturn's gravity field in its rings. *Planet. Sci. J.* 3. <http://dx.doi.org/10.3847/PSJ/ac4df8>.
- Hedman, M.M., Nicholson, P.D., French, R.G., 2019. Kronoseismology. IV: Six previously unidentified waves in Saturn's middle C ring. *Astron. J.* 157. <http://dx.doi.org/10.3847/1538-3881/aaf0a6>.

- Hedman, M.M., et al., 2007. Saturn's dynamic D ring. *Icarus* 188, 89–107. <http://dx.doi.org/10.1016/j.icarus.2006.11.017>.
- Less, L., et al., 2019. Measurement and implications of Saturn's gravity field and ring mass. *Science* 364. <http://dx.doi.org/10.1126/science.aat2965>.
- Jacobson, R.A., 2014. The orbits of the uranusian satellites and rings, the gravity field of the uranusian system, and the orientation of the pole of Uranus. *Astron. J.* 148. <http://dx.doi.org/10.1088/0004-6256/148/5/76>.
- Jerousek, R.G., et al., 2020. Saturn's C ring and Cassini division: Particle sizes from Cassini UVIS, VIMS, and RSS occultations. *Icarus* 344. <http://dx.doi.org/10.1016/j.icarus.2019.113565>.
- Latter, H.N., Ogilvie, G.I., 2008. Dense planetary rings and the viscous overstability. *Icarus* 195, 725–751. <http://dx.doi.org/10.1016/j.icarus.2008.02.001>.
- Marouf, E.A., French, R.G., Rappaport, N.J., Wong, K., McGhee, C., Anabtawi, A., 2011. Six centuries old spiral of vertical corrugations in Saturn's C-ring. In: AGU Fall Meeting Abstracts.
- Marouf, E.A., Tyler, G.L., Rosen, P.A., 1986. Profiling Saturn's rings by radio occultation. *Icarus* 68, 120–166. [http://dx.doi.org/10.1016/0019-1035\(86\)90078-3](http://dx.doi.org/10.1016/0019-1035(86)90078-3).
- Nicholson, P.D., Porco, C.C., 1988. A new constraint on Saturn's zonal gravity harmonics from Voyager observations of an eccentric ringlet. *J. Geophys. Res.* 93, 10209–10224. <http://dx.doi.org/10.1029/JB093iB09p10209>.
- Nicholson, P.D., et al., 2014. Noncircular features in Saturn's rings II: The C ring. *Icarus* 241, 373–396.
- Nicholson, P.D., et al., 2020. Occultation observations of Saturn's rings with Cassini VIMS. *Icarus* 344. <http://dx.doi.org/10.1016/j.icarus.2019.06.017>.
- Salo, H., Ohtsuki, K., Lewis, M.C., 2018. Computer simulations of planetary rings. Planetary ring systems. *Prop. Struct. Evol.* 434–493. <http://dx.doi.org/10.1017/9781316286791.016>.
- Salo, H., Schmidt, J., Spahn, F., 2001. Viscous overstability in Saturn's B ring. I. Direct simulations and measurement of transport coefficients. *Icarus* 153, 295–315. <http://dx.doi.org/10.1006/icar.2001.6680>.
- Schmidt, J., Ohtsuki, K., Rappaport, N., Salo, H., Spahn, F., 2009. Dynamics of Saturn's dense rings. In: *Saturn from Cassini-Huygens*. p. 413. http://dx.doi.org/10.1007/978-1-4020-9217-6_14.
- Schmidt, J., Salo, H., Spahn, F., Petzschmann, O., 2001. Viscous overstability in Saturn's B-ring. II. Hydrodynamic theory and comparison to simulations. *Icarus* 153, 316–331. <http://dx.doi.org/10.1006/icar.2001.6679>.
- Shu, F.H., 1984. Waves in planetary rings. pp. 513–561, *IAU Colloq. 75: Planetary Rings*.